РОССИЙСКИЙ ГОСУДАРСТВЕННЫЙ ПЕДАГОГИЧЕСКИЙ УНИВЕРСИТЕТ им. А. И. ГЕРЦЕНА
HERZEN STATE PEDAGOGICAL UNIVERSITY of RUSSIA

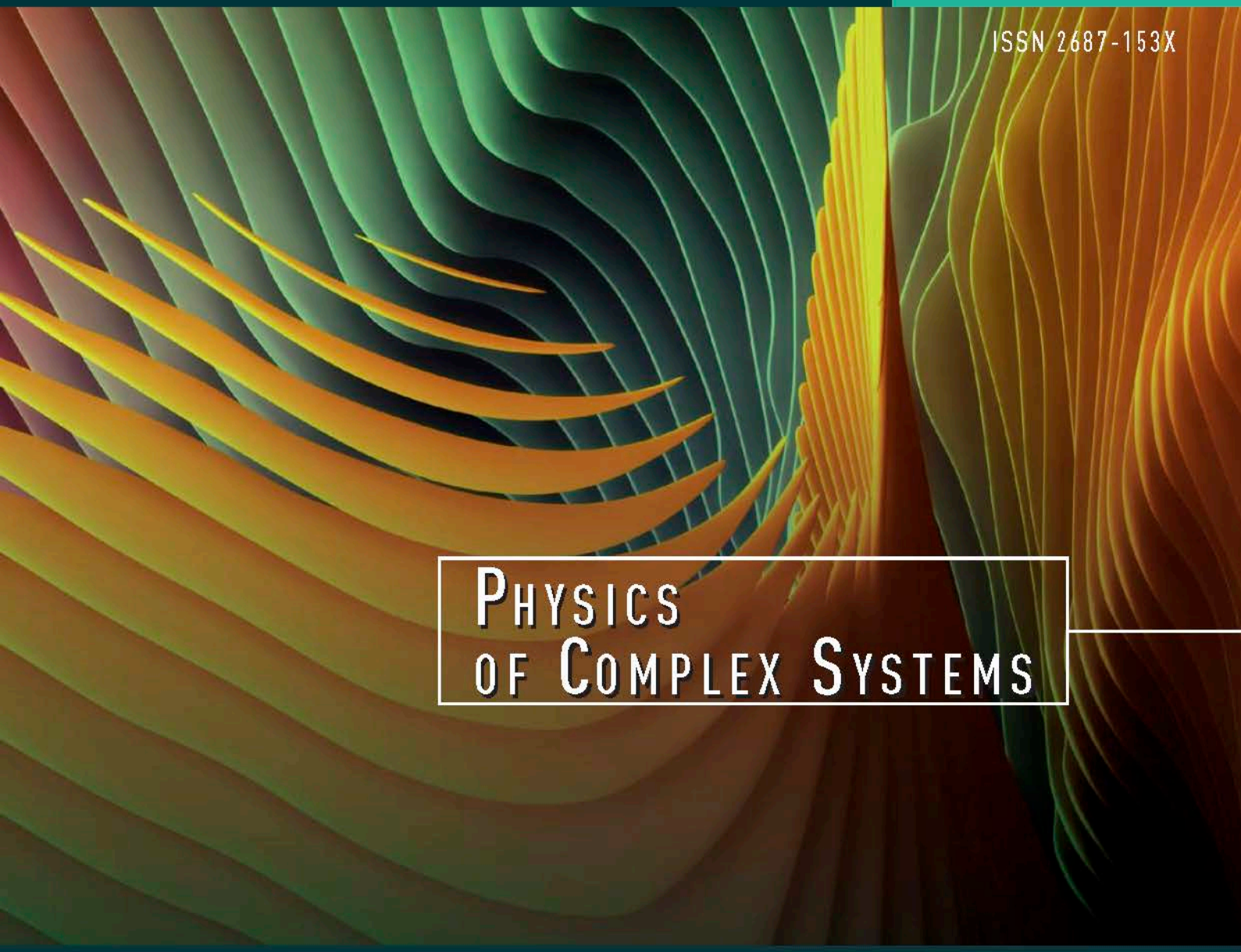

ISSN 2687-153X

PHYSICS OF COMPLEX SYSTEMS

Т. 6 № 1 2025

VOL. 6 NO. 1 2025

Herzen State Pedagogical University of Russia

ISSN 2687-153X (online)
physcomsys.ru
https://www.doi.org/10.33910/2687-153X-2025-6-1
2025. Vol. 6, no. 1

PHYSICS OF COMPLEX SYSTEMS

Mass Media Registration Certificate El No. FS77-77889, issued by Roskomnadzor on 10 February 2020
Peer-reviewed journal
Open Access
Published since 2020
4 issues per year

Publishing house of Herzen State Pedagogical University of Russia
48 Moika Emb., Saint Petersburg 191186, Russia
E-mail: izdat@herzen.spb.ru
Phone: +7 (812) 312-17-41

Data size 3,78 Mbyte
Published at 28.02.2025

Editor of the English text *I. A. Nagovitsyna*
Corrector *M. L. Kurakina*
Cover design by *O. V. Rudneva*
Layout by *D. V. Romanova*

Saint Petersburg, 2025

CONTENTS

Condensed Matter Physics. Dielectrics

UDC 628.313

EDN XCXNQF
https://www.doi.org/10.33910/2687-153X-2025-6-1-3-8

Polysulfonamide electret membranes for hydrocarbon emulsion separation

M. F. Galikhanov [1, 2], I. G. Shaikhiev [1], V. O. Dryakhlov [1], Z. T. Sanatullova ✉[1]

[1] Kazan National Research Technological University, 68 Karla Marksa Str., Kazan 420015, Russia
[2] Center for New Materials and Advanced Technologies of the Institute of Applied Research of the Academy of Sciences of the Republic of Tatarstan, 20 Baumana Str., Kazan 420111, Russia

Authors

Mansur F. Galikhanov, ORCID: 0000-0001-5647-1854, e-mail: mgalikhanov@yandex.ru

Ildar G. Shaikhiev, ORCID: 0000-0003-0542-0963, e-mail: ildars@inbox.ru

Vladislav O. Dryakhlov, ORCID: 0000-0003-2136-9221, e-mail: vladisloved@mail.ru

Zemfira T. Sanatullova, ORCID: 0009-0005-1620-3616, e-mail: my@3sanatullova.ru

For citation: Galikhanov, M. F., Shaikhiev, I. G., Dryakhlov, V. O., Sanatullova, Z. T. (2025) Polysulfonamide electret membranes for hydrocarbon emulsion separation. *Physics of Complex Systems*, 6 (1), 3–8. https://www.doi.org/10.33910/2687-153X-2025-6-1-3-8 EDN XCXNQF

Received 29 September 2024; reviewed 27 December 2024; accepted 27 December 2024.

Funding: The study did not receive any external funding.

Abstract. Wastewater containing emulsified petroleum products poses a serious threat to the environment. Hydrocarbons change the physicochemical properties of the environment, poison the body of living organisms, and envelop their bodies, leading to the suppression of biocenosis and degradation of ecosystems. In this regard, polysulfonamide membranes for water purification from emulsified oil have been studied. To increase resistance to oiling and improve performance, the filters were treated with corona discharge at a voltage of U = 5–35 kV for 1–5 minutes. As a result of corona treatment, the efficiency increased from 74.9 to 84.5%, while productivity increased by up to 11 times. This circumstance is explained by a change in the contact properties of the surface of the modified membranes, as shown by the results of this study.

Keywords: wastewater, petroleum products, polysulfonamide membranes, industrial oil, corona treatment, emulsion

Oil and petroleum products are fundamental components of the economic security of any state. At the same time, excessive intake of hydrocarbons into the environment leads to a decrease in the stability of ecosystems and pollution of the biosphere, as a result of which living organisms die, soil fertility decreases, water becomes unsuitable for drinking and fish farming, and air contributes to environmental diseases of the cardiovascular and respiratory systems. In the end, the person himself is exposed to the negative effects of adverse environmental factors, as a result of which the quality of life and work capacity decrease. The solution to this issue is the use of energy- and resource-saving technologies (Altapova et al. 2017; Dryakhlov et al. 2015; Fedotova et al. 2016; Zainullin, Abzalova 2019; Zainullin, Shaigallyamova 2019; Zainullin et al. 2005).

In this context, the use of membrane technologies for water purification from hydrocarbons is relevant. The advantages of polymer membranes include high efficiency, a wide range of sizes for cleaning contaminants (from ions to suspended solids), and a relatively small area occupied by equipment, which is important in industrial settings. The disadvantage is the concentration polarization of hydrocarbons

on the filter surface during separation, which leads to oiling of the membrane and a decrease in the performance of emulsion cleaning. To address this issue, the treatment of membranes with corona discharge is proposed.

In recent decades, the corona discharge has attracted increasing attention in both scientific and practical circles due to its unique properties and potential applications. A corona discharge is an electric discharge that occurs in a gas when the voltage exceeds a certain threshold, but does not reach the level necessary to create a full arc discharge. This phenomenon is widely studied in the context of electrophysics, materials science, and energy technologies.

Processing of polymer materials using corona discharge is a promising method that allows modifying their surfaces to improve adhesion, hydrophilicity, and other performance characteristics. Modern technologies require highly efficient approaches to polymer processing due to the growing needs of materials science and engineering. Corona discharge, as a physical process, ensures the creation of active centers on the surface of polymers, which opens up new possibilities for their functionalization.

When exposed to corona discharge, charged particles are formed, initiating a physical and chemical modification on the surface of the treated material to impart the necessary characteristics, as in the case of membranes, to increase wettability. The AC corona is characterized by the groups O–, HOO–, H_2O_2, and O_3. At higher humidity levels, the concentration of OH groups increases, while O– and O_3 – concentrations decrease. CO_3 ions are also formed during negative corona discharge.

Modification of polymer membranes by corona discharge is an effective method of modifying and improving their surface properties, which significantly improves their functionality and applicability in various industries.

The key advantages of this method include:

1. Increased adhesion. Corona discharge increases the wettability of the membrane surface, which contributes to the repulsion of the hydrocarbon phase and increases selectivity to water.

2. Improved separation efficiency. Corona discharge can increase the permeability of membranes to gases and liquids, which is particularly beneficial in wastewater treatment.

3. Antibacterial properties. Corona discharge facilitates the formation of functional groups with antimicrobial activity, which can enhance operational characteristics of the membrane.

Experimental studies (Shaikhiev et al. 2015; 2016a; 2016b; 2020a; 2020b; 2021) show that processing parameters such as discharge power, exposure time, and distance to the surface significantly affect the final properties of membranes. Properly optimizing these parameters is crucial to achieving the desired balance between improving the properties and maintaining the initial characteristics of polymers.

Based on the above, further research was conducted on the separation of water-oil emulsions (WOE) using industrial oil grade 'I20-A' (3%) and the surfactant 'Kositol 242' (0.2%) with polysulfonamide (PSA) membranes with a pore size of 0.1 μm. To intensify the process and increase resistance to fouling, the polymer filters were subjected to corona discharge plasma for 1–5 minutes at voltages ranging from 5 to 35 kV. As shown by the data in the table, the modification resulted in an increase in the separation efficiency to approximately 90%, with productivity increasing by up to 10 times. The results suggest that the tested ultrafiltration membranes can be effectively used for the purification of wastewater containing emulsified oils, such as those found in spent lubricating and cooling fluids or cleaning solutions.

Atomic force microscopy (AFM) using a MultiMode V probe microscope was used to obtain images of the surface of both the original (untreated) and modified PSA membranes.

Infrared (IR) spectra of the examined membrane samples were obtained using an IR Fourier spectrometer (Infralum FT-08) over the frequency range of 600–4000 cm^{-1}.

The initial stage of the research involved studying the separation of WOE using PSA membranes with a pore size of 0.01 μm pre-treated treated with corona discharge. The corresponding productivity graphs over the duration of the process are presented in Figure 1, and the COD values of the permeates are provided in Table 1.

Based on the data in Figure 1, an increase in the performance of the modified membranes up to 11 times is observed, with the highest values of productivity occurring at the maximum exposure time to corona discharge. At the same time, Table 1 indicates that the lowest COD value, corresponding to the highest efficiency of 84.5%, was achieved at τ = 5 min and U = 25 kV. This was accompanied by the lowest productivity, likely due to partial pore blockage. The efficiency of the initial membrane was 74.9%.

 https://www.doi.org/10.33910/2687-153X-2025-6-1-3-8

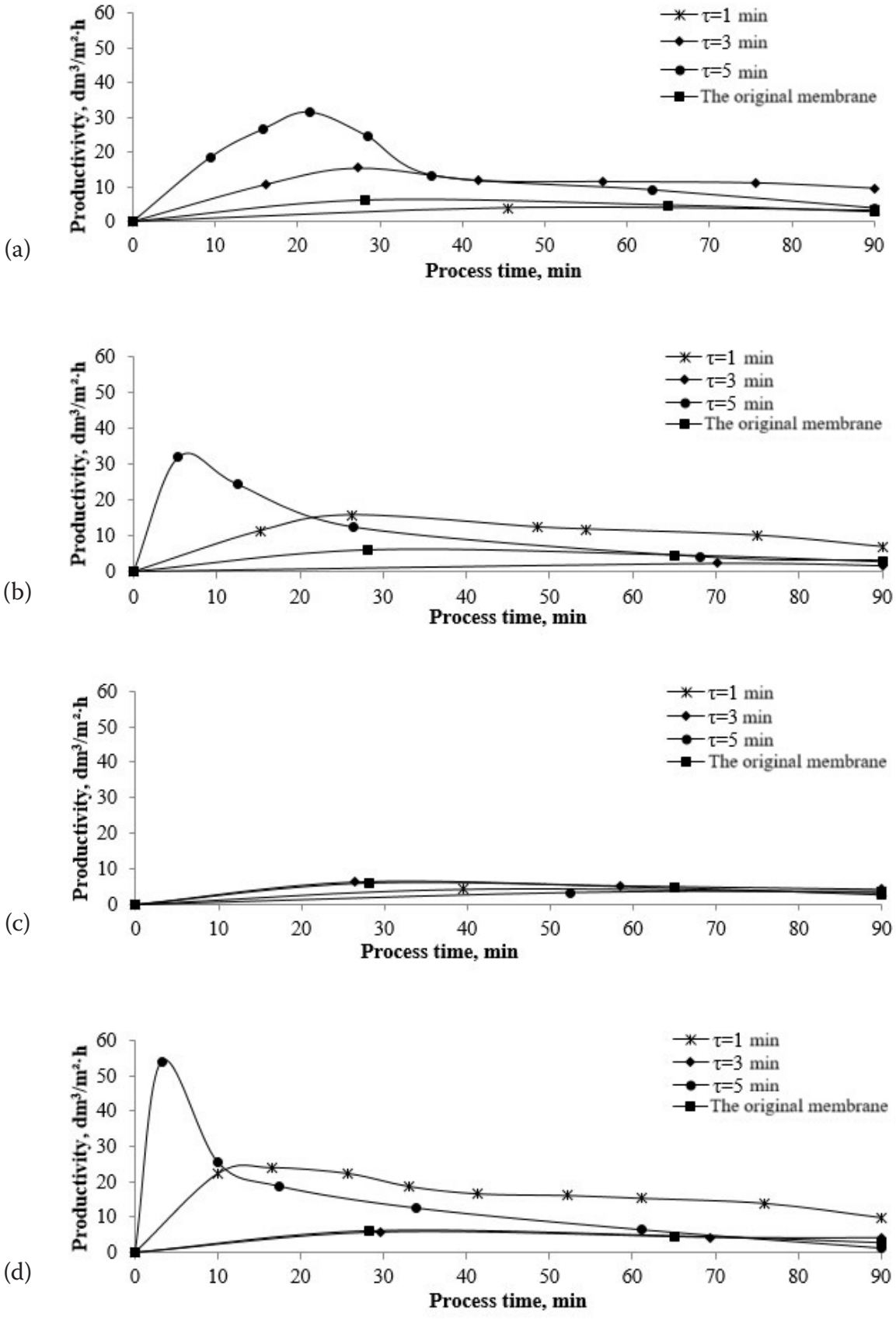

Fig. 1. Graphs showing the change in productivity of WOE separation using PSA membranes with a pore size of 0.01 μm, treated with corona discharge at a) U = 5 kV; b) U = 15 kV; c) U = 25 kV; d) U = 35 kV as a function of process time

Table 1. COD values of the permeates obtained from the separation of WOE using corona-treated PSA membranes with a pore size of 0.01 μm

Corona treatment time, τ, min	COD values, mg O/dm³			
	Corona treatment voltage, U, kV			
	5	15	25	35
1	6480	7020	5040	7020
3	6660	6480	7020	6840
5	5760	6660	**4860**	7200
Permeate after emulsion separation with the original membrane	**7880**			
Original/Initial emulsion	**31360**			

Subsequently, the effect of different types of plasma on the surface structure and internal structure of PSA membranes was evaluated using instrumental methods. In particular, Figure 2 shows images of the membrane surfaces after exposure to glow and corona discharge plasma.

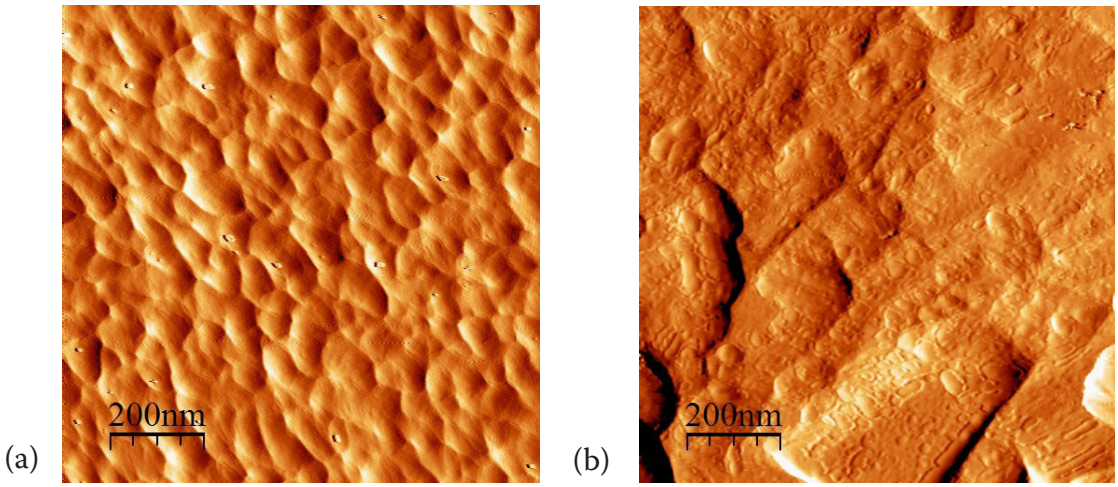

Fig. 2. Images of the surface of the PSA membrane: a) original; b) plasma-treated in corona discharge

Based on AFM analysis (Fig. 2), surface deformations were observed on the modified membrane, resulting in an increase in roughness. The height of the protrusions increased from 100 nm to 750 nm.

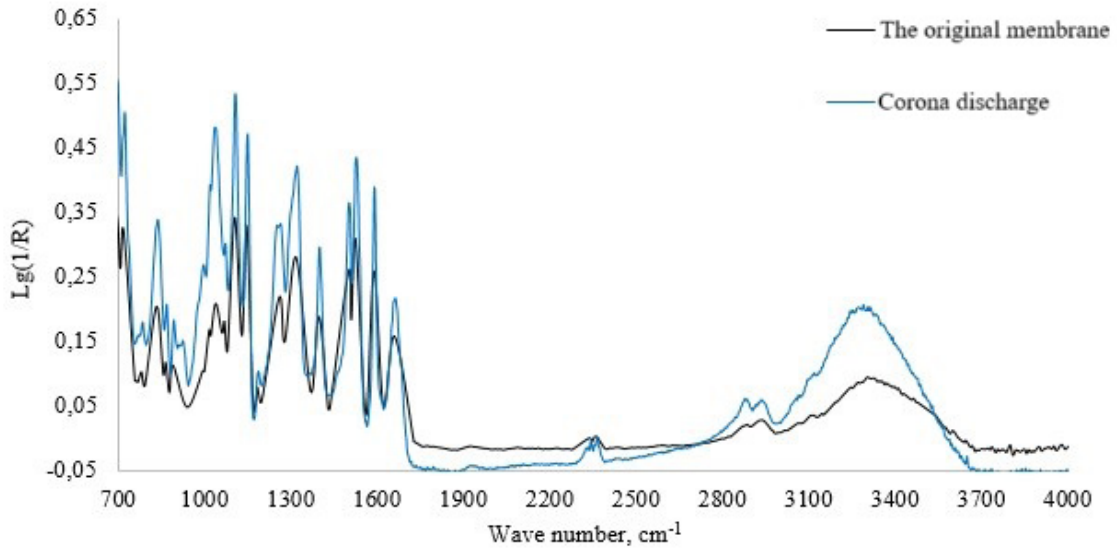

Fig. 3. IR spectra of PSA membranes before and after plasma treatment

https://www.doi.org/10.33910/2687-153X-2025-6-1-3-8

IR spectroscopy (Fig. 3) identified the following fragments of PSA: C–H, SO_2, C–S, C–O, N–H, C–C, and CH_2. Corona discharge treatment introduced oxygen-containing functional groups, which enhanced the hydrophilicity of the membrane surface, leading to improved operational characteristics.

Conclusions

The data obtained from this study indicate that corona discharge plasma treatment significantly improves the operational characteristics of polymer membranes, specifically in terms of productivity and efficiency in the separation of water-oil emulsions. These improvements are attributed to changes in both the topography and chemical structure of the membranes, as confirmed by AFM and IR spectroscopy, respectively.

Conflict of Interest

The authors declare that there is no conflict of interest, either existing or potential.

Author Contributions

All the authors contributed to the discussion of the final work and participated in writing the article.

References

Altapova, R. F., Sanatullova, Z. T., Shaikhiev, I. G. (2017) Udalenie maslyanykh plenok s poverkhnosti vody valyanymi i vojlochnymi otkhodami proizvodstva (monooksid ugleroda), obrabotannymi kremnijorganicheskimi zhidkostyami [Removal of oil films from the water surface by felting and felt production waste (carbon monoxide) treated with organosilicon liquids]. *Vestnik Tekhnologicheskogo universiteta — Bulletin of the Technological University*, 20 (19), 111–116. (In Russian)

Dryakhlov, V. O., Shaikhiev, I. G., Abdullin, I. Sh. et al. (2015) Vliyanie parametrov plazmy ponizhennogo davleniya na effektivnost' membrannogo razdeleniya vodomaslyanykh emul'sij [Impact of low-pressure plasma parameters on membrane separation efficiency of oil-water emulsions]. *Voda: khimiya i ekologiya — Water: Chemistry and Ecology*, 2 (80), 25–30. (In Russian)

Fedotova, A. V., Shaikhiev, I. G., Dryakhlov, V. O. et al. (2016) Vliyanie plazmy nizkogo davleniya na strukturu polisul'fonamidnykh membran i ikh razdelitel'nye kharakteristiki otnositel'no vodoneftyanoj emul'sii [Influence of low-pressure plasma on the structure of polysulfonamide membranes and their separation characteristics relative to a water-oil emulsion]. *Vestnik Belgorodskogo gosudarstvennogo tekhnologicheskogo universiteta imeni V. G. Shuhova — Bulletin of Belgorod State Technological University named after V. G. Shukhov*, 5, 167–173. (In Russian)

Shaikhiev, I. G., Altapova, A. F., Sanatullova, Z. T. (2016a) Issledovanie vliyaniya parametrov plazmennoj obrabotki na effektivnost' udaleniya devonskogo masla s poverkhnosti vody valyal'nymi i vojlochnymi otkhodami proizvodstva (monooksid ugleroda) [Investigation of the effect of plasma treatment parameters on the efficiency of removal of devonian oil from the water surface by felting and felt production waste (carbon monoxide)]. *Vestnik Tekhnologicheskogo universiteta — Bulletin of the Technological University,* 19 (23), 161–166. (In Russian)

Shaikhiev, I. G., Dryakhlov, V. O., Fazullin, D. D. (2020a) Membrannaya ochistka vody, soderzhashchej otrabotannye smazochnye materialy [Membrane purification of water containing spent lubricants]. *Chernye metally — Ferrous metals*, 7, 46–50. (In Russian)

Shaikhiev, I. G., Dryakhlov, V. O., Galikhanov, M. F. et al. (2020b) Razdelenie maslyanoj emul'sii s ispol'zovaniem poliakrilonitril'nykh membran, modifitsirovannykh koronnym razryadom [Separation of oil emulsion using polyacrylonitrile membranes, modified by corona discharge]. *Neorganicheskie materialy: Prikladnye issledovaniya*, 11 (5), 1160–1164. (In Russian)

Shaikhiev, I. G., Sanatullova, Z. T., Farnosova, T. F. (2021) Per'ya indejki — perspektivnyj sorbtsionnyj material dlya udaleniya nefti i masel iz vodnykh sred [Turkey feathers are a promising sorption material for removing oil and oils from aqueous media]. In: *Innovatsionnye tekhnologii zashchity okruzhayushchej sredy v sovremennom mire. materialy Vserossijskoj nauchnoj konferentsii s mezhdunarodnym uchastiem molodykh uchenykh i spetsialistov [Innovative technologies for environmental protection in the modern world. materials of the All-Russian scientific conference with international participation of young scientists and specialists]*. Kazan: Kazan National Research Technological University Publ., pp. 519–524. (In Russian)

Shaikhiev, I. G., Safina, G. Sh., Alekseeva, M. Yu. et al. (2016b) Vliyanie parametrov odnopolyarnogo koronnogo razryada na selektivnost' i proizvoditel'nost' razdeleniya vodomaslyanoj emul'sii polisul'fonamidnoj membranoj [Influence of parameters of a unipolar corona discharge on the selectivity and productivity of separation of a water-oil emulsion by polysulfonamide membrane]. *Vestnik Tekhnologicheskogo universiteta — Bulletin of the Technological University*, 19 (5), 89–92. (In Russian)

Shaikhiev, I. G., Safina, G. Sh., Dryakhlov, V. O. et al. (2015) Intensifikatsiya razdeleniya vodoneftyanykh emul'sij polisul'fopamidnymi membranami, obrabatyvaemymi v oblasti odnopolyarnogo koronnogo razryada [Intensification of separation of water-oil emulsions by polysulfopamide membranes treated in the field of unipolar corona discharge]. *Vestnik Tekhnologicheskogo universiteta — Bulletin of the Technological University*, 18 (17), 217–220. (In Russian)

Zainullin, A. M., Abzalova, A. G. (2019) Kompleksnaya fiziko-khimicheskaya ochistka stochnykh vod proizvodstva TNRS [Complex physico-chemical wastewater treatment of TNRS production]. In: *Innovatsionnye podkhody k resheniyu sovremennykh problem ratsional'nogo ispol'zovaniya prirodnykh resursov i okhrany okruzhayushchej sredy. Sbornik dokladov Mezhdunarodnoj nauchno-tekhnicheskoj konferentsii [Innovative approaches to solving modern problems of rational use of natural resources and environmental protection. Collection of reports of the International Scientific and Technical Conference]*. Belgorod: BSTU Publ., pp. 188–191. (In Russian)

Zainullin, A. M., Shaigallyamova, L. S. (2019) Ochistka stochnykh vod proizvodstva nitrosoedinenij aromaticheskogo ryada [Wastewater treatment of the production of aromatic nitro compounds]. In: *Innovatsionnye podkhody k resheniyu sovremennykh problem ratsional'nogo ispol'zovaniya prirodnykh resursov i okhrany okruzhayushchej sredy. Sbornik dokladov Mezhdunarodnoj nauchno-tekhnicheskoj konferentsii [Innovative approaches to solving modern problems of rational use of natural resources and environmental protection. Collection of reports of the International Scientific and Technical Conference]*. Belgorod: BSTU Publ., pp. 192–195. (In Russian)

Zainullin, A. M., Shaikhiev, I. G., Friedland, S. V. (2005) Issledovanie kataliticheskoj ochistki stochnykh vod proizvodstva diazodinitrokhinona [Investigation of catalytic wastewater treatment of diazodinitroquinone production]. *Bezopasnost' zhiznedeyatel'nosti*, 7, 46–47. (In Russian)

 https://www.doi.org/10.33910/2687-153X-2025-6-1-3-8

Condensed Matter Physics. Dielectrics

UDC 538.9

EDN ZZHQFC
https://www.doi.org/10.33910/2687-153X-2025-6-1-9-16

Charge transport mechanism and memristive effect in a thin film based on fluorinated polyaryl ether containing 1,4-dioxo-thioxanthene-9-one in-chain blocks

A. A. Gismatulin ✉[1], V. A. Pustovarov [2], D. S. Odintsov [3], I. A. Os'kina [3], I. K. Shundrina [3], I. A. Azarov [1], L. A. Shundrin [3], V. A. Gritsenko [1]

[1] Rzhanov Institute of Semiconductor Physics, Siberian Branch of the Russian Academy of Sciences, 13 Lavrentiev Ave., Novosibirsk 630090, Russia
[2] Ural Federal University, 19 Mira Str., Ekaterinburg 620002, Russia
[3] N. N. Vorozhtsov Institute of Organic Chemistry, Siberian Branch of the Russian Academy of Sciences, 9 Lavrentiev Ave., Novosibirsk 630090, Russia

Authors

Andrei A. Gismatulin, ORCID: 0000-0003-3177-6226, e-mail: aagismatulin@isp.nsc.ru

Vladimir A. Pustovarov, ORCID: 0000-0001-7373-1152, e-mail: v.a.pustovarov@urfu.ru

Danila S. Odintsov, ORCID: 0000-0002-6644-6211, e-mail: odintsov@nioch.nsc.ru

Irina A. Os'kina, ORCID: 0000-0001-5788-0182

Inna K. Shundrina, ORCID: 0000-0003-1172-7523, e-mail: ishund@nioch.nsc.ru

Ivan A. Azarov, ORCID: 0000-0001-9571-2227, e-mail: azarov@isp.nsc.ru

Leonid A. Shundrin, ORCID: 0000-0002-5091-2812, e-mail: shundrin@nioch.nsc.ru

Vladimir A. Gritsenko, ORCID: 0000-0003-1646-0848, e-mail: grits@isp.nsc.ru

For citation: Gismatulin, A. A., Pustovarov, V. A., Odintsov, D. S., Os'kina, I. A., Shundrina, I. K., Azarov, I. A., Shundrin, L. A., Gritsenko, V. A. (2025) Charge transport mechanism and memristive effect in a thin film based on fluorinated polyaryl ether containing 1,4-dioxo-thioxanthene-9-one in-chain blocks. *Physics of Complex Systems*, 6 (1), 9–16. https://www.doi.org/10.33910/2687-153X-2025-6-1-9-16 EDN ZZHQFC

Received 9 October 2024; reviewed 9 December 2024; accepted 9 December 2024.

Funding: The research related to the charge transport study was supported by the state contract under the ISP SB RAS program No. FWGW-2025-0010 The work on organic polymer synthesis as well as the fabrication of metal-polymer-silicon and memristor structures was funded by the state contract under the N. N. Vorozhtsov Institute of Organic Chemistry SB RAS program No. FWUE-2022-0007.

Abstract. A new fluorinated thermally stable polyaryl ether with electron-withdrawing thioxanthenone in-chain block (FPAE-ThS) was synthesized through the interaction of perfluorobiphenyl with 1,4-dihydroxy-*9H*-thioxanthene-9-one. The charge transport mechanism within the FPAE-ThS film is governed by the phonon-assisted tunneling between neighbouring traps. The thermal (1.0 eV) and optical trap (2.0 eV) ionization energies, as well as the trap concentration ($N = 1.0 \times 10^{20}$ cm^{-3}), are determined. The value of half Stokes shift (1.1 eV), obtained from the photoluminescence and photoluminescence excitation spectra, is consistent with the results of charge transport simulation. Furthermore, a prototype memory device based on the FPAE-ThS film demonstrates the resistive switching behavior with a four-order difference in the resistance between its low- and high-resistance states.

Keywords: fluorinated polymers, charge transport, memristor, trap, photoluminescence, photoluminescence excitation spectra

Introduction

The main advantages of organic devices over silicon-based counterparts include low cost of organic materials, inexpensive and environmentally friendly fabrication of organic electronic components using printing technologies and their versatile properties, such as lightweight, flexibility, transparency, durability, and reliability (Kronemeijer et al. 2014). Recently, a non-volatile memristor memory based on organic films has been developed (Shaposhnik et al. 2020; Yuan et al. 2021). This type of memory holds significant potential for next-generation flash memory and neuromorphic artificial intelligence devices.

The key requirements for organic polymers used in memristor technologies are their thermostability and ambipolarity. Specifically, the polymer structure must feature the alternating electron-donor and electron-acceptor chain blocks that facilitate the trap mechanism of electron transport. Thioxanthone (9*H*-thioxanthen-9-one) and its derivatives are electron acceptor compounds (Vasilieva et al. 2012) and found numerous practical applications (Jiang, Yin 2014a; 2014b; Kumar, Pereira 2020; Nazir et al. 2015; Neumann et al. 1997; Wang et al. 2014; Wang et al. 2018; Wu et al. 2014; Yilmaz et al. 2010). Recent studies have shown that the C-H fragments at the 1,4-positions of the 9*H*-thioxanthen-9-one ring can be replaced by OH groups during the cyclization of arylsulfanylbenzoic acid and benzoquinone (Loskutov, Beregovaya 2009), yielding the corresponding 1,4-dihydroxy-1*H*-thioxanthen-9-one (**1**, Fig. 1). Compound **1** was found to be a strong electron acceptor (Odintsov et al. 2023). The presence of two functional OH groups in the structure of compound **1** provides an opportunity to synthesize an electroactive polymer containing thioxanthone-like structures as an effective electron-acceptor in-chain block. This motivated us to synthesize fluorinated polyaryl ether with electron acceptor 1,4-dioxy-9*H*-thioxanthene-9-one in-chain blocks (FPAE-ThS, Fig. 1) for its potential application in polymer-based resistive memory devices. Notably, polyfluoroaromatic fragments were not previously used in the design of electroactive polymers for this purpose. Perfluorobyphenyl was chosen as the second monomer for polycondensation because of its regioselective reactivity with nucleophiles, which is facilitated by the reactive F atoms at the 1,8-positions of the cycle. Meanwhile, the presence of two F atoms in the ortho-positions of the benzene rings may also reduce the π-conjugation between the thioxanthenone and tetrafluorophenyl fragments of the polymer chain, thus, increasing the polymer energy gap (E_g), and preventing the emergence of semiconducting properties.

The study of charge transport mechanisms, in particular leakage currents, can provide insights into the trap nature of polymer films through the characterization of trap energies (Gismatulin et al. 2024). Time-of-flight transient experiments on polymers showed that the logarithm mobility is proportional to the square root of the electric field ($\sqrt{F}$) (Dunlap et al. 1996; Hirao et al. 1995; Novikov et al. 1998). This dependence is formally described by the Frenkel law in inorganic dielectric films (Frenkel 1938; Ganichev et al. 2000; Gritsenko et al. 2018; Schroeder 2015).

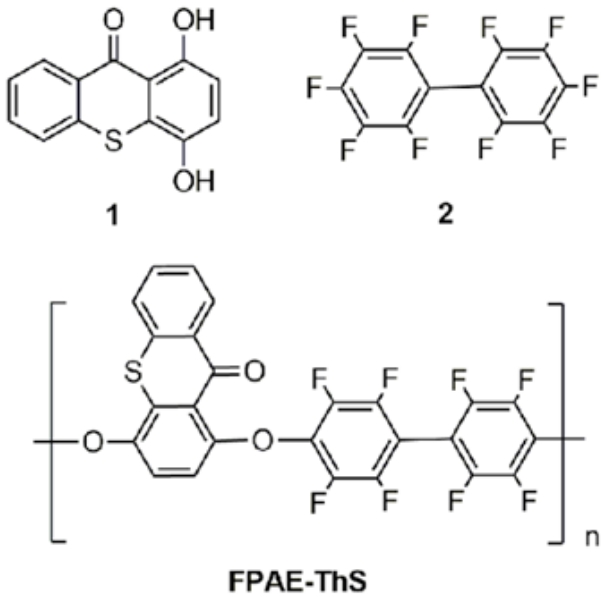

Fig. 1. Structures of 1,4-dihydroxy-1H-thioxanthen-9-one (1), perfluorobiphenyl (2) and FPAE-ThS

 https://www.doi.org/10.33910/2687-153X-2025-6-1-9-16

The primary objective of the reported study is to explore the charge transport mechanisms within thin FPAE-ThS films and to determine the trap parameters that govern the charge transport. In addition, the potential of using FPAE-ThS films as an active medium in memristor devices was investigated.

Methods

FPAE-ThS was synthesized through the nucleophilic polycondensation of monomers **1** and **2** in dimethylacetamide using K_2CO_3 to increase the basicity of the solution (ESI). FPAE-ThS showed good molecular weight properties for forming thin films on Si wafers and demonstrated its thermal stability up to 247 °C. Its electrochemical reduction/oxidation activity confirmed the ability of FPAE-ThS to facilitate the charge transport (ESI). The polymer has an energy gap (E_g) of 3.02 eV, which classifies FPAE-ThS as a dielectric material (ESI).

To investigate the trap ionization mechanism in the FPAE-ThS film, experimental current density (*j*) and electric field (*F*) characteristics, measured at different temperatures, were compared with different theoretical models (Gismatulin et al. 2024).

To fabricate metal-insulator-silicon (MIS) structures, FPAE-ThS polymer films were deposited from a 1% FPAE-ThS solution in chloroform on Si (100) p-type silicon substrates, with the resistances of 10 Ohm×cm and 0.001 Ohm×cm, by spin coating using the SpinNXG-P1AC spin coater. Prior to deposition, the Si substrate was treated with a 10% HF solution to remove the native oxide layer. An array of upper aluminum (Al) electrodes was sputtered onto the FPAE-ThS layer through a shadow mask by thermal sputtering, with a contact area of 0.5 mm^2. To enhance the electrical contact for *j-F* measurements, the bottom electrode was also thermally sputtered over the entire area of the non-planar Si substrate. The *j-F* characteristics of the Si/FPAE-ThS/Al structure were measured using a Keithley 2400 electrometer. Measurements were conducted over a temperature range of 300 to 375K using a Linkam LTS420E cell, with the temperature controlled by a Linkam T95 temperature controller. The voltage ramp rate was set to 0.9 V/sec.

The thickness and refractive index of the FPAE-ThS films were measured using an Ellips-1881 SAG spectral ellipsometer. A film thickness of 110 nm was used to study the charge transport mechanism, while a film thickness of 25 nm was employed for the memristor structure.

The photoluminescence (PL) spectra in the range of 1.7–3.3 eV and the photoluminescence excitation (PLE) spectra in the range of 3.3–5.2 eV were measured at the temperature of 4.4 K. Measurements were carried out using a HORIBA iXR320 FLUOROLOG spectrometer, equipped with a cooled Synapse plus CCD camera (Horiba) as a detector and a 150 W ozone-free Xe lamp. A closed-cycle cryogenic system and a high-vacuum helium cryostat (Trade Engineering, Russia) with an RDK-205D2 cryohead (Japan), controlled by a Lake Shore 331 temperature controller, were used to cool the sample. The PL spectra were recorded with a spectral resolution of 2 nm, while the PLE spectra were normalized to the number of exciting photons using a calibrated photodiode. The PL spectra are presented without normalization to the spectral sensitivity of the detection system.

The transverse charge transport mechanism in a copolymer is similar to that in a dielectric due to its high energy gap. It is described by the following expression (Gismatulin et al. 2024; Gritsenko et al. 2018):

$$j = \frac{e}{a^2} P = eN^{\frac{2}{3}} P, \tag{1}$$

where *j* is the current density, *e* is the electron charge, *a* is the average distance between traps, $N = a^{-3}$ is the trap concentration, and *P* is the trap ionization probability.

The exponential dependence of the current density on the electric field in the Frenkel effect arises from the reduction in the Coulomb barrier under the influence of the electric field. The trap ionization probability in the Frenkel model is described by the following expression (Frenkel 1938):

$$P = \nu \exp\left(- \frac{W - \left(\frac{e^3}{\pi \varepsilon_\infty \varepsilon_0} \right)^{\frac{1}{2}} \sqrt{F}}{kT} \right), \tag{2}$$

where $\nu = W/h$ is the attempt to escape factor, *W* is the trap ionization energy, *h* is the Planck constant, $\varepsilon_\infty = n^2$ is the high-frequency permittivity, *n* is the refractive index, ε_0 is the dielectric constant, *F* is the electric field, *k* is the Boltzmann constant, and *T* is the temperature.

For high concentrations of neutral traps, the phonon-assisted tunneling mechanism between neighboring traps, as proposed by Nasyrov and Gritsenko, is applicable. In this model, electron tunneling occurs from one trap to a neighboring trap, rather than ionization into the FPAE-ThS conduction band, due to the short distance between traps (Odintsov et al. 2022).

The trap ionization probability in the Nasyrov and Gritsenko phonon-assisted tunneling model between neighboring traps is given by the expression (Nasyrov, Gritsenko 2011):

$$P = \frac{2\sqrt{\pi}\hbar W_t}{m^* a^2 \sqrt{2kT\left(W_{opt} - W_t\right)}} \exp\left(-\frac{W_{opt} - W_t}{kT}\right) \exp\left(-\frac{2a\sqrt{2m^* W_t}}{\hbar}\right) \sinh\left(\frac{eFa}{2kT}\right), \quad (3)$$

where, $\hbar$ is the reduced Planck constant, W_t is the thermal trap ionization energy, m^* is the effective mass, and W_{opt} is the optical trap ionization energy.

Results and discussion

The refractive index (n) and absorption coefficient (α) are shown in Fig. 2. These optical constants were determined by reconstructing the data from multiple angles using an inverse ellipsometry approach, applying optimization techniques for each photon energy individually. In the ultraviolet region, three distinct peaks are observed in both the refractive index and the absorption coefficient, corresponding to photon energies of 3.1 eV, 3.9 eV and 4.5 eV. The refractive index in the infrared region is consistent with values typically found in similar organic films (Odintsov et al. 2022). At a photon energy of 1.1 eV, the refractive index of the FPAE-ThS film is measured to be 1.49, as shown in Fig. 2.

The experimental *j-F* characteristics of the p-Si/FPAE-ThS/Al structure were simulated by the Frenkel model (see Fig. 3(a)). The corresponding trap ionization energy (W) obtained from the simulation is 0.55 eV. The attempt-to-escape factor (ν) was then calculated using the Einstein relation: $\nu = W/h$, giving a value of 1.3×10^{14} sec^{-1} at the trap ionization value of 0.55 eV. The high-frequency dielectric constant parameter value obtained from the simulation is 19. Alternatively, the high-frequency dielectric constant can be derived from the expression $\varepsilon_\infty = n^2 = (1.49)^2 = 2.22$. Thus, the Frenkel effect is not a suitable model to describe the charge transport and trap ionization in the FPAE-ThS film. In addition, the Frenkel model predicts an extraordinarily low trap concentration value, $N = 1.5 \times 10^{11}$ cm^{-3}, which is inconsistent with typical trap concentrations in inorganic dielectrics, normally ranging from 10^{18} to 10^{21} cm^{-3} (Nasyrov, Gritsenko 2013).

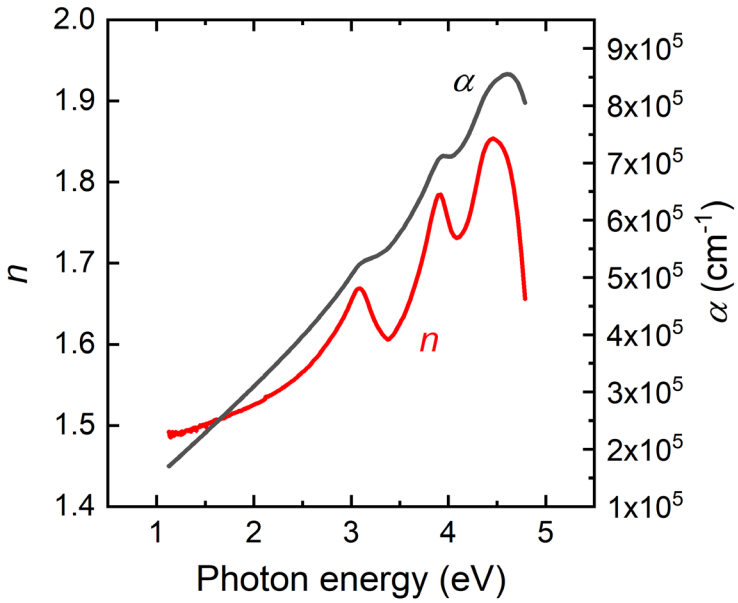

Fig. 2. Refractive index (n) and absorption coefficient (α) of the FPAE-ThS film at different quantum energies

 https://www.doi.org/10.33910/2687-153X-2025-6-1-9-16

In the Nasyrov and Gritsenko model, the trap ionization probability exhibits an exponential dependence on the intertrap distance, $a = N^{-1/3}$, or, equivalently, on the trap concentration N. Thus, the trap concentration can be determined from the curve slope of the j-F characteristic (see Fig. 3(b)). The simulation results based on the Nasyrov and Gritsenko model give the following fitting parameters: trap concentration $N = 1.0 \times 10^{20}$ cm^{-3}, thermal trap ionization energy $W_t = 1.0$ eV, optical trap ionization energy $W_{opt} = 2.0$ eV and effective electron mass $m^* = 0.39\ m_e$.

The PL spectra of the FPAE-ThS film are shown in Fig. 4. A broad peak in the range of 2.25–2.45 eV predominates the PL spectrum. In addition, the PLE spectrum, shown in Fig. 5, reveals three maxima at 3.80, 4.55 and 5.05 eV. Notably, the PLE peaks at 3.8 eV and 4.55 eV coincide with the peaks in the refractive index and absorption coefficient spectra of the FPAE-ThS film, suggesting that the luminescence centers of the FPAE-ThS film are associated with these energy levels. The thermal trap energy $W_t = 1.0 \pm 0.1$ eV obtained from the charge transport simulation is in agreement with the half Stokes shift value of 1.1 ± 0.1 eV of the PL and PLE spectra.

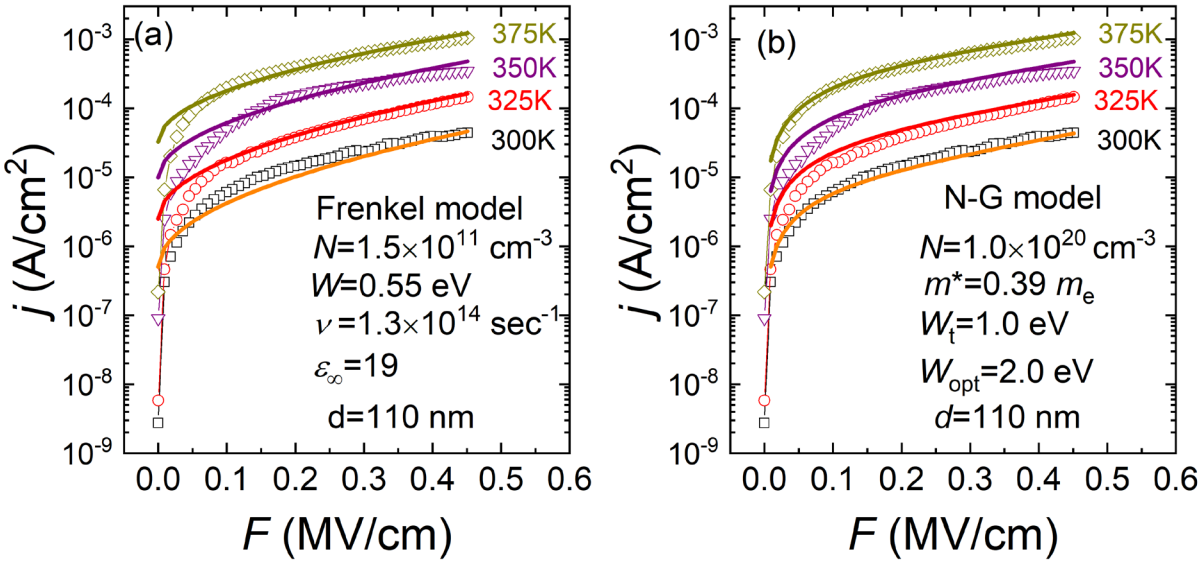

Fig. 3. j-F characteristics of the FPAE-ThS-based structure at various temperatures, along with simulations using (a) the Frenkel model and (b) the Nasyrov-Gritsenko model

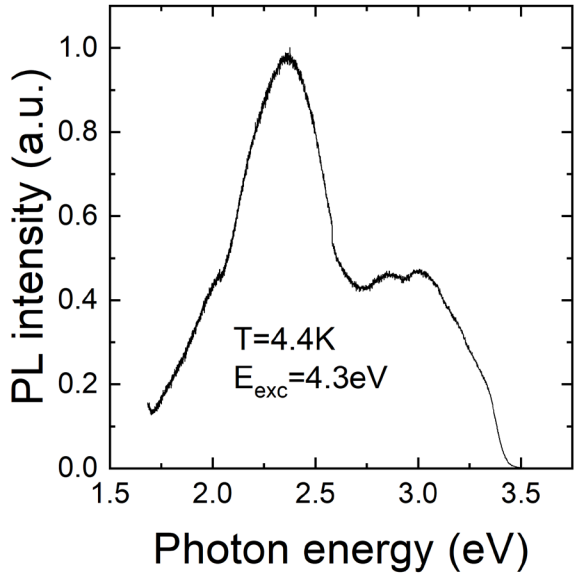

Fig. 4. Photoluminescence spectra of the FPAE-ThS film at a temperature of 4.4 K

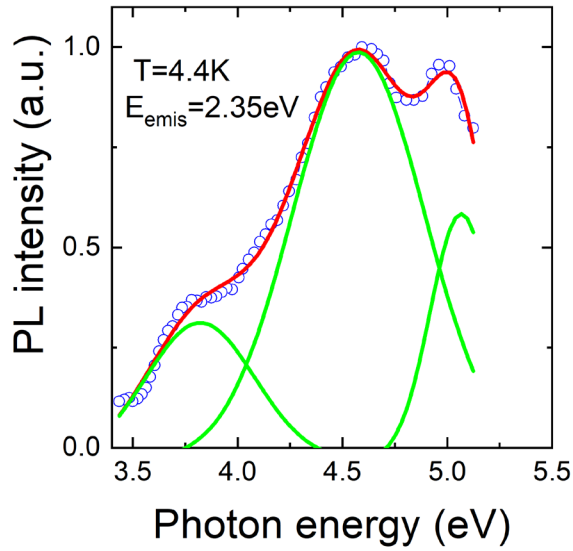

Fig. 5. Photoluminescence excitation spectrum (2.35 eV emission band) of the FPAE-ThS film at a temperature of 4.4 K (blue circles). The green curves represent the decomposition of the spectrum into three peaks, the red line denotes the sum of these individual components

The potential application of the FPAE-ThS film as an active medium in a memristor is demonstrated through the p^{++}-Si/FPAE-ThS/Al MIS structure (see Fig. 6). This structure, with a 25 nm thick FPAE-ThS film, shows its reversible resistive switching behavior from the high resistance state (HRS) to the low resistance state (LRS) when the voltage sweep is increased from 0 V to +3V and from the LRS to the HRS when the voltage sweep is reversed from 0 V to -2.5V. (Fig. 6). The FPAE-ThS-based memristor is a low-power memory device, making it a promising candidate for practical applications in the Resistive Random-Access Memory (ReRAM) technology, which requires switching voltages of less than 5 V.

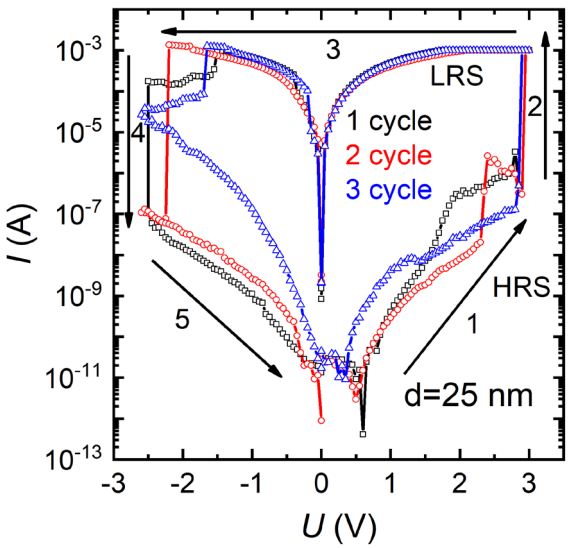

Fig. 6. current-voltage characteristics of the FPAE-ThS-based memristor, with arrow numbers 1 to 5 indicating the voltage sweep direction

Conclusions

We described the synthesis and properties of a novel electroactive polyaryl ether containing an electron-withdrawing thioxanthenone in-chain block and a polyfluoroaromatic tetrafluorobiphenyl fragment. This fragment was used for the first time in the design of organic polymers for practical applications

 https://www.doi.org/10.33910/2687-153X-2025-6-1-9-16

in memristor technologies. The charge transport mechanism in the thin FPAE-ThS film was studied by measuring the current density-electric field characteristics of the corresponding MIS structures at different temperatures and modelling the experimental data using both the Frenkel model and the Nasyrov-Gritsenko model of phonon-assisted tunneling between traps. It was shown that the Frenkel model fails to describe the experimental data, predicting an anomalously high value of the high-frequency permittivity and an anomalously low trap concentration. In contrast, the Nasyrov-Gritsenko model of phonon-assisted tunneling between traps quantitatively describes the experimental data, yielding values for the thermal (W_t = 1.0 eV) and optical (W_{opt} = 2.0 eV) trap energies, as well as a reasonable trap concentration (N=1.0×10^{20} cm^{-3}) for the FPAE-ThS film. These results indicate that the charge transport in the FPAE-ThS film is effectively described by a multiphonon mechanism, similar to processes occurring in semiconductors and inorganic dielectrics. Moreover, the thermal trap energy derived from the simulation of the charge transport mechanism in FPAE-ThS films is consistent with the half Stokes shift value observed in the PL and PLE spectra of the FPAE-ThS film, taking into account measurement and simulation errors. In addition, FPAE-ThS was shown to be a viable active layer for memristors. The FPAE-ThS-based memristor structure has low switching voltages and a 4-order resistance ratio between HRS and LRS, thus making it particularly advantageous for applications in the Resistive Random-Access Memory (ReRAM) technology.

Conflict of Interest

The authors declare that there is no conflict of interest, either existing or potential.

Author Contributions

All authors contributed equally to the final work, engaging in discussions and collaborating on the writing of the article.

Acknowledgements

The authors acknowledge the Core Facilities VTAN NSU and the Multi-Access Chemical Research Center of the Siberian Branch of the Russian Academy of Sciences for granting an access to their experimental equipment and instrumental facilities.

References

Dunlap, D. H., Parris, P. E., Kenkre, V. M. (1996) Charge-dipole model for the universal field dependence of mobilities in molecularly doped polymers. *Physical Review Letters*, 77, article 542. https://doi.org/10.1103/PhysRevLett.77.542 (In English)

Frenkel, J. (1938) On pre-breakdown phenomena in insulators and electronic semi-conductors. *Physical Review*, 54, 647–648. https://doi.org/10.1103/PhysRev.54.647 (In English)

Ganichev, S. D., Ziemann, E., Prettl, W. et al. (2000) Distinction between the Poole-Frenkel and tunneling models of electric-field-stimulated carrier emission from deep levels in semiconductors. *Physical Review B*, 61, 10361–10365. https://doi.org/10.1103/PhysRevB.61.10361 (In English)

Gismatulin, A. A., Odintsov, D. S., Shundrina, I. K. et al. (2024) Charge transport mechanism and trap origin in methyl methacrylate copolymer with thioxanthenone side groups. *Chemical Physics Letters*, 840, article 141140. https://doi.org/10.1016/j.cplett.2024.141140 (In English)

Gritsenko, V. A., Perevalov, T. V., Voronkovskii, V. A. et al. (2018) Charge transport and the nature of traps in oxygen deficient tantalum oxide. *ACS Applied Materials & Interfaces*, 10, 3769–3775. https://doi.org/10.1021/acsami.7b16753 (In English)

Hirao, A., Nishizawa, H., Sugiuchi, M. (1995) Diffusion and drift of charge carriers in molecularly doped polymers. *Physical Review Letters*, 75, 1787–1790. https://doi.org/10.1103/PhysRevLett.75.1787 (In English)

Jiang, X., Yin, J. (2014a) Copolymeric photoinitiators containing in-chain thioxanthone and coinitiator amine for photopolymerization. *Journal of Applied Polymer Science,* 94, 2395–2400. https://doi.org/10.1002/app.21178 (In English)

Jiang, X., Yin, J. (2014b) Polymeric photoinitiator containing in-chain thioxanthone and coinitiator amines. *Macromolecular Rapid Communications*, 25, 748–752. https://doi.org/10.1002/marc.200300270 (In English)

Kronemeijer, A. J., Pecunia, V., Venkateshvaran, D. et al. (2014) Two-dimensional carrier distribution in top-gate polymer field-effect transistors: correlation between width of density of localized states and Urbach energy. *Advanced Materials*, 26, 728–733. https://doi.org/10.1002/adma.201303060 (In English)

Kumar, M., Pereira, L. (2020) Towards highly efficient TADF yellow-red OLEDs fabricated by solution deposition methods: Critical influence of the active layer morphology. *Nanomaterials*, 10 (1), article 101. https://doi.org/10.3390/nano10010101 (In English)

Loskutov, V. A., Beregovaya, I. V. (2009) Reaction of thiosalicylic acid with 1,4-quinones and cyclization of the resulting arylsulfanylbenzoic acids. *Russian Journal of Organic Chemistry,* 45, 1405–1409. https://doi.org/10.1134/S1070428009090152 (In English)

Nasyrov, K. A., Gritsenko, V. A. (2011) Charge transport in dielectrics via tunneling between traps. *Journal of Applied Physics*, 109, article 093705. https://doi.org/10.1063/1.3587452 (In English)

Nasyrov, K. A., Gritsenko, V. A. (2013) Transport mechanisms of electrons and holes in dielectric films. *Physics Uspekhi*, 56, 999–1012. https://doi.org/10.3367/UFNe.0183.201310h.1099 (In English)

Nazir, R., Balciunas, E., Buczynska, D. et al. (2015) Donor–acceptor type thioxanthones: Synthesis, optical properties, and two-photon induced polymerization. *Macromolecules,* 48, 2466–2472. https://doi.org/10.1021/acs.macromol.5b00336 (In English)

Neumann, M. G., Gehlen, M. H., Encinas, M. V. et al. (1997) Photophysics and photoreactivity of substituted thioxanthones. *Journal of the Chemical Society, Faraday Transactions*, 93, 1517–1521. https://doi.org/10.1039/A607264J (In English)

Novikov, S. V., Dunlap, D. H., Kenkre, V. M. et al. (1998) Essential role of correlations in governing charge transport in disordered organic materials. *Physical Review Letters*, 81, article 4472. https://doi.org/10.1103/PhysRevLett.81.4472 (In English)

Odintsov, D. S., Shundrina, I. K., Gismatulin, A. A. et al. (2022) Heat-resistant polyimides with electron-acceptor pendant groups of the thioxanthenone series for resistive storage devices with a low switching voltage. *Journal of Structural Chemistry*, 63, 1811–1819. https://doi.org/10.1134/S0022476622110117 (In English)

Odintsov, D. S., Os'kina, I. A., Irtegova, I. G. et al. (2023) Electrochemical reduction of 1*H*-thioxanthene-1,4,9-trione and 3-methyl-1*H*-thioxanthene-1,4,9-trione—representatives of a new class of heterocycles related to thioxanthenone. *European Journal of Organic Chemistry*, 26 (33), article e202300459. https://doi.org/10.1002/ejoc.202300459 (In English)

Schroeder, H. (2015) Poole-Frenkel-effect as dominating current mechanism in thin oxide films — an illusion?! *Journal of Applied Physics,* 117, article 215103. https://doi.org/10.1063/1.4921949 (In English)

Shaposhnik, P. A., Zapunidi, S. A., Shestakov, M. V. et al. (2020) Modern bio and chemical sensors and neuromorphic devices based on organic semiconductors. *Russian Chemical Reviews*, 89, 1483–1506. https://doi.org/10.1070/rcr4973 (In English)

Vasilieva, N. V., Irtegova, I. G., Loskutov, V. A. et al. (2012) Redox properties and radical anions of 2-substituted thioxanthen-9-ones and their 2-methyl S-oxide derivatives. *Mendeleev Communications,* 23 (6), 334–336. https://doi.org/10.1016/j.mencom.2013.11.010 (In English)

Wang, H., Xie, L., Peng, Q. et al. (2014) Novel thermally activated delayed fluorescence materials–thioxanthone derivatives and their applications for highly efficient OLEDs. *Advanced Materials,* 26, 5198–5204. https://doi.org/10.1002/adma.201401393 (In English)

Wang, Y., Zhu, Y., Xie, G. et al. (2018) Red thermally activated delayed fluorescence polymers containing 9H-thioxanthen-9-one-10,10-dioxide acceptor group as pendant or incorporated in backbone. *Organic Electronics*, 59, 406–413. https://doi.org/10.1016/j.orgel.2018.05.058 (In English)

Wu, Q., Xiong, Y., Liang, Q. et al. (2014) Developing thioxanthone based visible photoinitiators for radical polymerization. *RSC Advances*, 4, article 52324. https://doi.org/10.1039/C4RA07614A (In English)

Yilmaz, G., Tuzun, A., Yaggi, Y. (2010) Thioxanthone–carbazole as a visible light photoinitiator for free radical polymerization. *Journal of Polymer Science. Part A: Polymer Chemistry*, 48, 5120–5125. https://doi.org/10.1002/pola.24310 (In English)

Yuan, L., Liu, S., Chen, W. et al. (2021) Organic memory and memristors: From mechanisms, materials to devices. *Advanced Electronic Materials*, 7 (11), article 2100432. https://doi.org/10.1002/aelm.202100432 (In English)

Condensed Matter Physics. Dielectrics

UDC 537.3

EDN OEOMHP
https://www.doi.org/10.33910/2687-153X-2025-6-1-17-25

Electret properties and electrical conductivity of polypropylene-polyphenylene sulfide composites

A. A. Pavlov ✉[1], M. A. Kovalenko [2], V. A. Goldade [2, 3], M. E. Borisova [1], S. V. Zotov [2]

[1] Peter the Great St. Petersburg Polytechnic University,
29 Polytechnicheskaya Str., Saint Petersburg 195251, Russia
[2] V. A. Belyi Metal-Polymer Research Institute of National Academy of Sciences of Belarus,
32 Kirova Str., Gomel 246050, Belarus
[3] Francisk Skorina Gomel State University, 102 Sovetskaya Str., Gomel 246003, Belarus

Authors

Andrey A. Pavlov, ORCID: 0000-0001-5459-7509, e-mail: pavlov.aa.hv@mail.ru

Mikhail A. Kovalenko, e-mail: mikhailkovalenko1991@gmail.com

Victor A. Goldade, ORCID: 0000-0001-7964-8034, e-mail: victor.goldade@gmail.com

Margarita E. Borisova, ORCID: 0000-0003-0761-6302, e-mail: vladimirl.borisov@gmail.com

Sergey V. Zotov, ORCID: 0000-0002-4480-6503, e-mail: zotov-1969@mail.ru

For citation: Pavlov, A. A., Kovalenko, M. A., Goldade, V. A., Borisova, M. E., Zotov, S. V. (2025) Electret properties and electrical conductivity of polypropylene-polyphenylene sulfide composites. *Physics of Complex Systems*, 6 (1), 17–25. https://www.doi.org/10.33910/2687-153X-2025-6-1-17-25 EDN OEOMHP

Received 4 September 2024; reviewed 28 October 2024; accepted 28 October 2024.

Funding: The study had no financial support.

Abstract. The electret properties and electrical conductivity of polypropylene-polyphenylene sulfide (PP-PPS) composites were studied. The results reveal that the effective surface charge density is higher in fibrous-porous materials (FPM) compared to film-based composites. In the electrical conductivity-temperature dependence, a characteristic up-turn is observed at a temperature of 110 °C, where the high-temperature segment of the curve corresponds to the intrinsic conductivity of the composite. The low-temperature segment can be attributed to structural defects. Additionally, two relaxation maxima are identified in the thermally stimulated depolarization (TSD) current spectra. The low-temperature peak is associated with the charge relaxation at the matrix-filler interface, a phenomenon driven by Maxwell — Wagner polarization. The high-temperature maxima are likely related to the relaxation of charges governed by the intrinsic conductivity of PP in its amorphous phase.

Keywords: polypropylene, polyphenylene sulfide, electret, electrical conductivity, composite material

Introduction

In recent years, there has been an increasing demand for polymer composites incorporating fillers of diverse types, including dielectric fillers (metal oxides, clays) (Galikhanov et al. 2024a; 2024b; Gorokhovatskij et al. 2020), nanostructured fillers (aerosil, talc, nanotubes, montmorillonite, diatomite) (Galikhanov et al. 2019; Goldade et al. 2020; 2021; Kovalenko, Goldade 2021; Kovalenko et al. 2023; Minzagirova et al. 2021), as well as polymer blends and copolymers (Aniskina et al. 2010; Castro et al. 2024; Gorokhovatskij et al. 2022; Guliakova et al. 2024). The introduction of fillers allows to adjust various material properties, including mechanical, electrical, and optical characteristics, allowing for the fabrication of composites with tailored performance attributes (Galikhanov et al. 2024b). The investigation

of the electret state in polymer composites is of significant practical importance, since the electret charge influences key performance characteristics of materials, i. e., liquid permeability, friction wear resistance, and filtration efficiency (Goldade et al. 2019; Kestelman 2000; Li et al. 2021).

The objective of this study is to investigate the electret effect in composite materials composed of polypropylene and polyphenylene sulfide. A comparison is made between film-based samples and fibrous-porous samples, as the electret state in the latter significantly influences filtration efficiency (Chen et al. 2023; Kara, Molnár 2021; Zhang 2020).

Materials and methods

The reported experiments are based on polypropylene (PP) 4445S produced by Rospolymer LLC (T_m = 160 °C) and polyphenylene sulfide (PFS) NHU-PPS produced by ZHEJIANG NHU SPECIAL MATERIALS CO.LTD (Tm = 230 °C). To obtain the PP-PPS composite, both powdered and granular forms of polymers were used. Mechanical mixing did not yield a homogeneous distribution of the components within the mixture. Consequently, a twin-screw extrusion method was employed using a SuPlast 25/2 extruder (China).

Following extrusion, the polymer was cooled and granulated, with the resulting granules used for subsequent sample fabrication. Two distinct sample types were analyzed: 1) fibrous-porous material (FPM) produced via melt-blowing technology (Pinchuk 2012) and 2) film samples obtained by hot pressing. FPM samples, each with a diameter of 1 cm, were cut from the PP-PPS composite, with a thickness ranging between 1–1.5 mm.

The thickness of the polymer films was 150–170 μm. The following sample compositions were investigated: 1) PP (without filler); 2) PP 90 wt. % + PPS 10 wt. %; 3) PP 80 wt. % + PPS 20 wt. %; 4) PP 65 wt. % + PPS 35 wt. %. The selected component ratios were based on the superior filtration efficiency of the PP-PPS composites.

Electrets formation was achieved using corona discharge at a potential of –6 kV (Fig. 1). The initial electret potential difference was adjusted by positioning a grid in the air gap between the needle and the sample. The charge process was conducted at room temperature for 1 minute. The ion transfer from the discharge region ceased when the potentials of the sample surface and the grid became equal, allowing the electret potential difference to be set.

The electret properties of the polymer composites were evaluated using two techniques: 1) measurement of the effective surface charge density (ESCD) and 2) thermally stimulated depolarization (TSD) current spectroscopy (Gorokhovatskij 1991). The polarity and magnitude of the ESCD were determined using an IPEP-1 electrostatic field parameter meter (MNIPI, Minsk, Belarus).

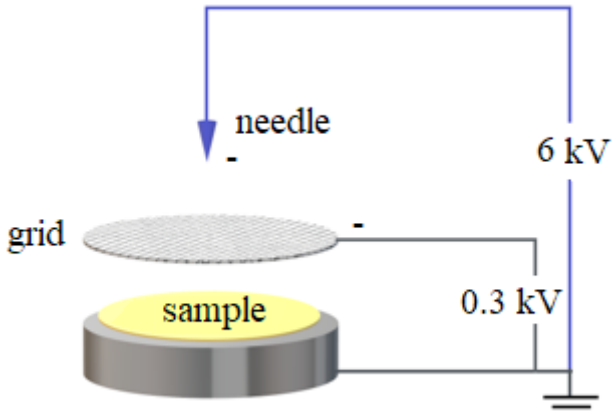

Fig. 1. Schematic of the sample charging process

To study the temperature stability of electrets, measurements of thermally stimulated voltage (TSV) and thermally stimulated depolarization (TSD) currents were conducted.

The temperature dependence of TSV, denoted as $U(T)$, allows for a visual assessment of the electret state stability in the material: the lower the temperature at which a sharp decline in U is observed, the less stable the charge. The $U(T)$ curves were obtained at a constant heating rate of 1 K/min.

 https://www.doi.org/10.33910/2687-153X-2025-6-1-17-25

Assuming that the relaxation of the near-surface homocharge occurs due to the intrinsic conductivity of the dielectric, the temperature dependence of the conductivity can be calculated using the following formula:

$$\gamma(T) = \frac{-\varepsilon\varepsilon_0\beta}{U(T)} \cdot \frac{\mathrm{d}U}{\mathrm{d}T}, \tag{1}$$

where β is the heating rate, K/s, and ε is the relative permittivity of the composite material.

The relative permittivity of composite materials was calculated using the Lichtenecker's formula (Bogorodickij 1965):

$$\lg \varepsilon = \theta_1 \cdot \lg \varepsilon_1 + \theta_2 \cdot \lg \varepsilon_2, \tag{2}$$

where ε_1 and ε_2 represent the relative permittivity of individual components, while θ_1 and θ_2 denote the volume fractions of these components. The results of these calculations are presented in Table 1.

Table 1. Relative permittivity of PP and PP-PPS

Material	PP	PP + 10% PPS	PP + 20% PPS	PP + 35% PPS
ε	2.20	2.25	2.30	2.39

The primary method for studying charge relaxation processes is the thermally stimulated depolarization (TSD) current technique. The position of the TSD current maxima is determined by the chemical composition of the material, the charging method, and the nature of the sample's contact with the electrodes. The TSD current method is also capable of detecting moisture, impurities, and material aging.

TSD currents were measured at a constant heating rate of 2 °C/min, with an insulating layer (PTFE film, 30 μm thick) placed between the sample surface and the electrode (Fig. 2). The resistivity of the insulating layer (~10^{18} ohms/m) is several orders of magnitude higher than that of the PP + PPS samples. In this configuration, the direction of the TSD current corresponds to the movement of charge carriers through the volume of the composite.

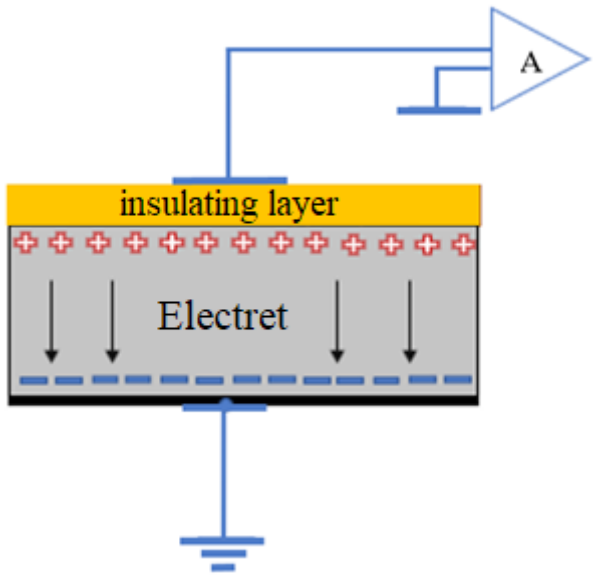

Fig. 2. TSD current measuring scheme

Results and discussion

Effective surface charge density

The effective surface charge density ESCD (σ_e) is a critical property of electrets, reflecting both the magnitude of the surface charge and the extent of the charge distribution within the material. ESCD is equivalent to the potential difference of the electret U:

$$U = \int_0^L E(x)\mathrm{d}x = E_i L = \frac{\sigma_e}{\varepsilon\varepsilon_0} = \mathrm{A}\sigma_e, \quad (3)$$

where L is the thickness of the electret, E_i is the average internal field of the electret, A is a constant.

The ESCD of FPM samples prior to corona discharge treatment ranges from –0.2 to +0.7 μC/m^2 (Fig. 3). This value represents the technological charge present in all samples and is determined by the manufacturing process. After treatment with corona discharge, a significant increase in ESCD was recorded. As the content of PPS in the composite increased from 10% to 35%, the ESCD rose to values of –3.0 and –6.2 μC/m^2, respectively.

The technological charge value in the film samples lies in the range from –0.12 to –0.3 μC/m^2 (Fig. 4). The maximum ESCD observed after corona discharge treatment in the film samples was –2.3 μC/m^2, which is notably lower than the corresponding values for the FPM samples.

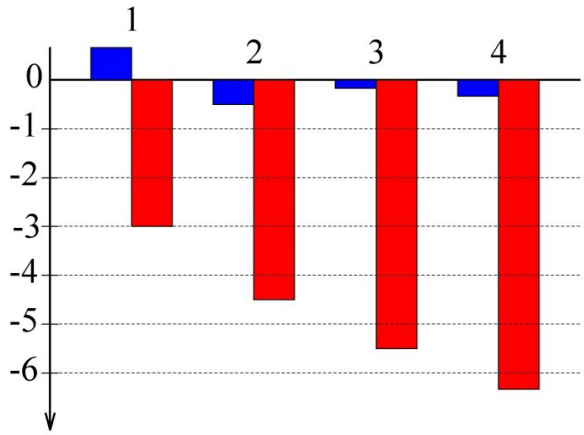

Fig. 3. ESCD values (μC/m^2) before (blue bars) and after (red bars) charging of FPM samples. Labels 1, 2, 3, and 4 correspond to PFS contents of 0%, 10%, 20%, and 35 wt.% in the PP + PFS composition, respectively

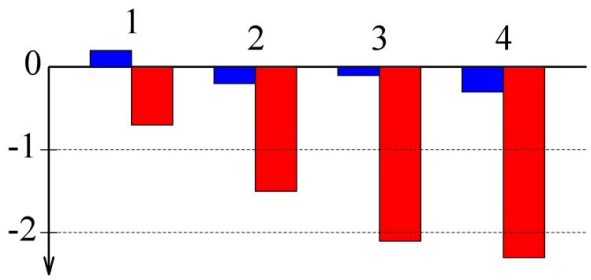

Fig. 4. ESCD values (μC/m^2) before (blue bars) and after (red bars) charging of film samples. Labels 1, 2, 3, and 4 correspond to PFS contents of 0%, 10%, 20%, and 35 wt.% in the PP + PFS composition, respectively

https://www.doi.org/10.33910/2687-153X-2025-6-1-17-25

The FPM structure contains numerous air inclusions (pores or inter-fiber spaces). The local electric fields within these pores can significantly exceed the intensity of the external electric field, potentially reaching levels that approach electric breakdown of air. This phenomenon leads to a sharp increase in the number of charge carriers adsorbed on the fibers, which, in turn, results in an increase in ESCD.

The subsequent results were obtained by studying the electret properties of the film samples.

Thermally stimulated voltage. Electrical conductivity

Figure 5 shows temperature dependences of the electret potential difference $U(T)/U_0$.

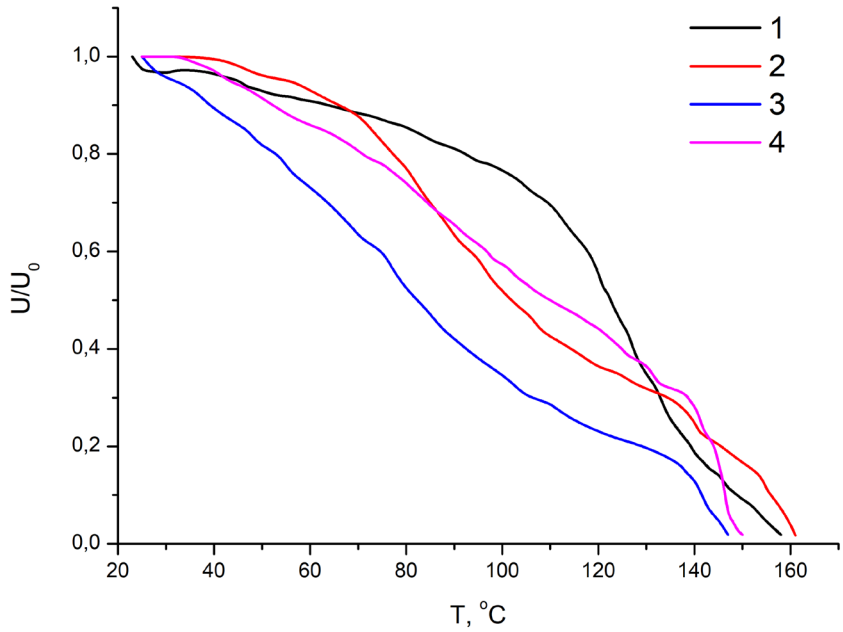

Fig. 5. Temperature dependences of the electret potential difference $U(T)/U_0$: PP (*1*), PP 90 % + PPS 10 % (*2*), PP 80 % + PPS 20 % (*3*), PP 65 % + PPS 35 % (*4*)

Figure 5 shows that the most stable electret state is observed in pure polypropylene (curve 1), where the electret potential difference changes only slightly as the sample is heated to 110 °C. In contrast, the U/U_0 of the composite materials decreases almost linearly as the temperature increases.

The temperature dependence of the electrical conductivity of dielectric materials is derived from formula 1 (Fig. 6).

A notable difference in the temperature dependence of the electrical conductivity is observed between pure PP (curve 1) and the PP + PPS composites. In pure PP, the electrical conductivity decreases steadily with increasing temperature. In contrast, the composites exhibit a distinct break at approximately 110 °C, which can be attributed to the ionic conductivity mechanism in dielectrics.

The ionic conductivity of dielectrics is typically governed by two distinct mechanisms, as described by (Borisova, Kojkov 1979). At low temperatures, conductivity is primarily influenced by impurities, whereas at higher temperatures the movement of the primary ions of the material becomes the dominant factor. The temperature dependence of conductivity, γ(T), can be expressed as:

$$\gamma(T) = A_1 e^{\left(-\frac{E_1}{kT}\right)} + A_2 e^{\left(-\frac{E_2}{kT}\right)}, \quad (4)$$

where A_1 and A_2 are independent coefficients, and E_1 and E_2 are activation energies associated with the two conduction mechanisms.

In Figure 6, curve 3 is approximated by two distinct segments with different slopes. The high-temperature segment of the curve represents the intrinsic conductivity of the dielectric material, while the low-temperature region exhibits a weaker slope ($E_1 < E_2$), indicating that the conductivity in this region is primarily determined by the nature and concentration of impurities (in this case, PFS).

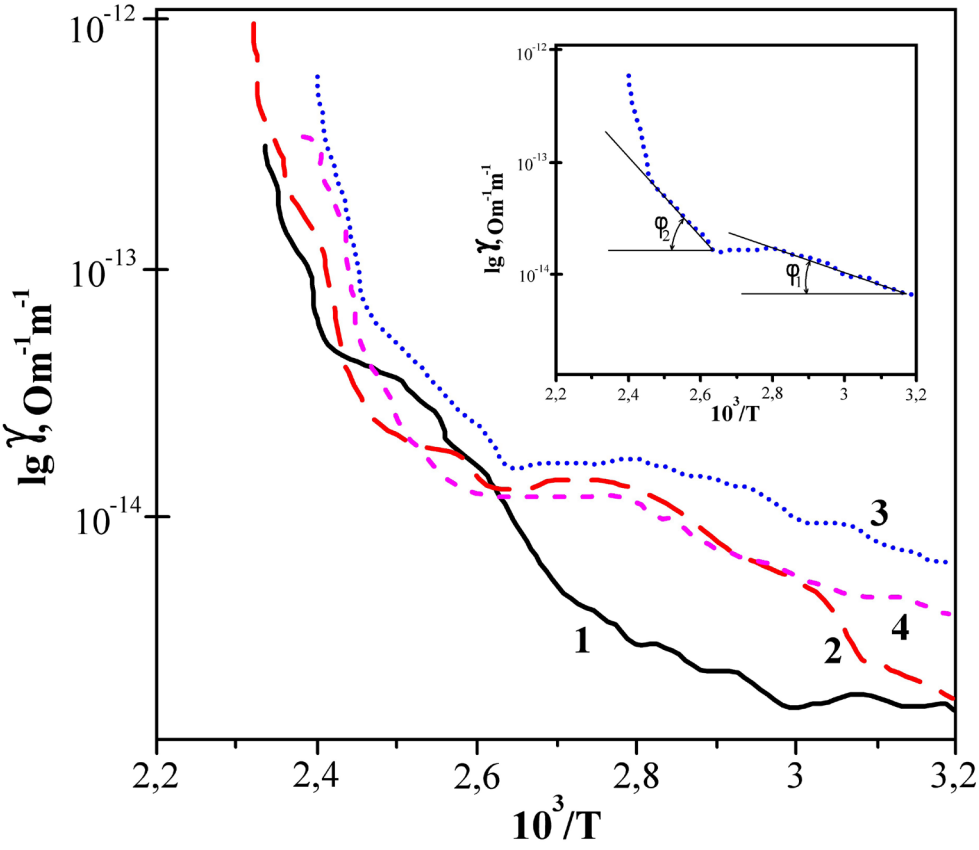

Fig. 6. Temperature dependence of the electrical conductivity:
PP (*1*), PP 90 % + PPS 10 % (*2*), PP 80 % + PPS 20 % (*3*), PP 65 % + PPS 35 % (*4*)

TSD current spectra

Figure 7 shows the temperature dependences of the TSD currents.

Two relaxation maxima are evident in the TSD spectra. The low-temperature maximum (T = 75÷90°C) is due to the relaxation process of the charge accumulated at the interface between the matrix (PP) and the filler (PPS), which exhibit different dielectric permittivity, ε, leading to Maxwell — Wagner polarization. The activation energy for the high-temperature current maxima ranges from 1.7 to 3.8 eV and increases with higher filler concentrations.

The high-temperature maximum (T = 135÷145 °C) may be associated with a relaxation process caused by the intrinsic conductivity of PP in the amorphous phase. The accumulated charge remains stable until the crystalline phase of PP melts at approximately 160 °C.

The TSD current spectra are analyzed using discrete elementary Debye maxima, each characterized by a single relaxation time (Borisova et al. 2004). In this case, the TSD current can be expressed by the formula:

$$I_{TSD} = I_m \cdot \exp\left(\frac{W_a}{kT_m} - \frac{W_a}{kT}\right) \cdot \exp\left(-\frac{W_a}{kT_m^2} \cdot \int_{T_m}^{T} \exp\left[\frac{W_a}{kT_m} - \frac{W_a}{kT}\right] dT\right), \quad (5)$$

where k is the Boltzmann constant, T_m is the temperature at which the current reaches its maximum I_m, W_a is the activation energy, τ_m is the relaxation time at the temperature of the current maxima.

An example of the experimental and calculated data for PP + 20% PPS sample is shown in Figure 8.

From the obtained graphs, the activation energies for the relaxation peaks were calculated and are presented in Table 2.

 https://www.doi.org/10.33910/2687-153X-2025-6-1-17-25

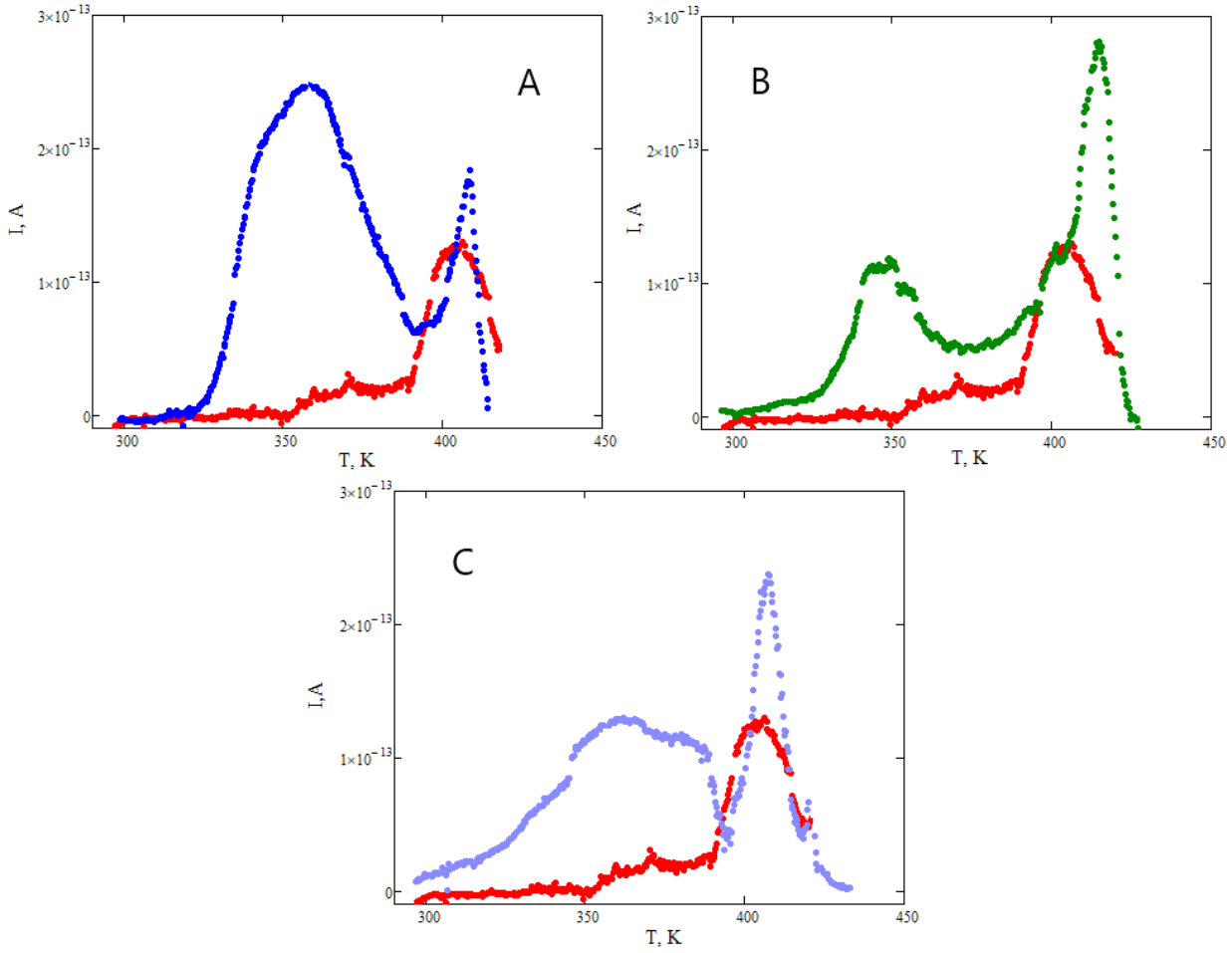

Fig. 7. TSD spectra for the PP sample (red) and composites with varying PPS content: PP + 10% PPS (A), PP + 20% PPS (B), PP + 35% PPS (C)

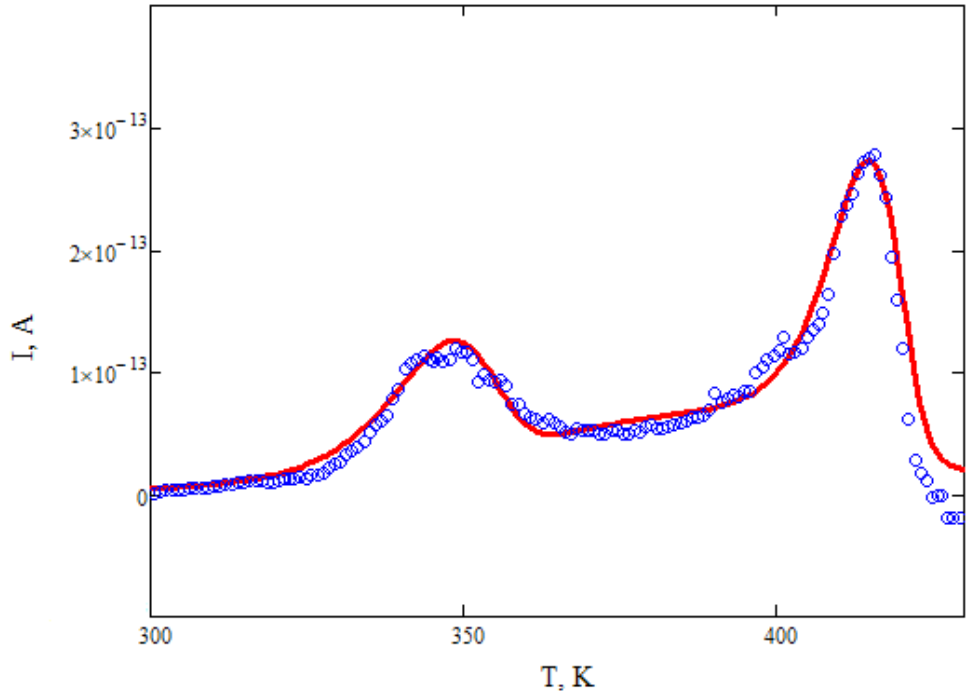

Fig. 8. Experimental (points) and calculated (solid line) TSD current for the PP + 20% PPS sample

Table 2. Current maxima and calculated activation energy values

Sample	T_m, K	I_m, 10^{-13} A	W_a, eV
PP	406	1.3	1.7
PP + 10% PPS	357	2.4	0.6
	410	1.6	1.9
PP + 20% PPS	348	1.0	1.3
	415	2.8	2.6
PP + 35% PPS	365	1.3	0.5
	408	2.3	3.8

The activation energy for the high-temperature current maxima varies from 1.7 to 3.8 eV, with an increasing trend as the filler concentration rises.

Conclusion

The study shows that the polarization of polypropylene samples filled with polyphenylene sulfide results in the formation of an electret state. Notably, the effective surface charge density is significantly higher in fibrous-porous materials compared to film-based materials. This increase in the ESCD is likely due to the formation of strong local electric fields within the pores, which substantially enhance the number of charge carriers, thereby boosting the ESCD.

In pure PP, the electrical conductivity decreases steadily with increasing temperature, while composites exhibit a distinct change in the conductivity curve at approximately 110 °C. The high-temperature segment of the curve reflects the intrinsic conductivity of the dielectric, while low-temperature conductivity is primarily influenced by material impurities.

Two relaxation maxima are observed in the TSD current spectra. The low-temperature maximum is associated with the relaxation of the charge accumulated at the interface between the matrix (PP) and the filler (PFS), which exhibit different dielectric permittivity, ε, leading to Maxwell — Wagner polarization. The high-temperature maximum can be attributed to a relaxation process caused by the intrinsic conductivity of polypropylene in the amorphous phase.

To enhance the electret properties, further investigations are recommended on composite materials based on polypropylene with lower concentrations of polyphenylene sulfide, as the greatest influence of the filler on the electret characteristics of the composite material is observed at filler concentrations below 10% (Galikhanov et al. 2019; Gorokhovatskij et al. 2020; Kovalenko et al. 2023). However, it is important to note that the electret state of filter materials does not always correlate with improved filtration efficiency (Xiao 2015). Therefore, a careful balance must be struck between the desired material properties and the technical and economic constraints of the production process.

Conflict of Interest

The authors declare that there is no conflict of interest, either existing or potential.

Author Contributions

All the authors contributed to the final work and participated in the writing of the article.

References

Aniskina, L. B., Viktorovich, A. S., Galikhanov, M. F. et al. (2010) Polielektrolitnaya model' voloknitov na osnove polietilena i polipropilena [Polyelectrolyte model of fibrites based on polyethylene and polypropylene]. *Izvestiya Rossijskogo gosudarstvennogo pedagogicheskogo universiteta im. A. I. Gertsena — Izvestia: Herzen University Journal of Humanities & Sciences*, 135, 24–36. (In Russian)

Bogorodickij, N. P. (1965) *Teoriya dielektrikov. [The theory of dielectrics]*. Leningrad: Energiya Publ., 344 p. (In Russian)

Borisova, M., Kojkov, S. (1979) *Fizika dielektrikov [Physics of dielectrics]*. Leningrad: Leningrad State University Publ., 240 p. (In Russian)

 https://www.doi.org/10.33910/2687-153X-2025-6-1-17-25

Borisova, M. E., Galukov, O. V., Tsatsynkin, P. V. (2004) *Fizika dielektricheskikh materialov. Elektroperenos i nakoplenie zaryada v dielektrikakh [Physics of dielectric materials. Charge transfer and preservation in dielectrics]*. Saint Petersburg: Saint Petersburg State University Publ., 106 p. https://doi.org/10.18720/SPBPU/2/si20-477 (In Russian)

Castro, R. A., Karulina, E. A., Galikhanov, M. F. et al. (2024) Relaxation of electric charge in polymer blends based on low-density polyethylene and copolymer of ethylene with vinyl acetate. *St. Petersburg State Polytechnical University Journal: Physics and Mathematics*, 17 (3), 36–45. https://doi.org/10.18721/JPM.17304 (In English)

Chen, C., Chen, G., Zhang, J. et al. (2023) Study on corona charging characteristic of melt-blown polypropylene electret fabrics. *Journal of Electrostatics*, 121, article 103782. https://doi.org/10.1016/j.elstat.2022.103782 (In English)

Galikhanov, M. F., Minzagirova, A. M., Spiridonova, R. R. (2019) Modifying the properties of polyethylene electrets through the incorporation of montmorillonite. *Surface Engineering and Applied Electrochemistry*, 55, 679–683. https://doi.org/10.3103/S106837551906005X (In English)

Galikhanov, M. F., Minzagirova, A. M., Guliakova, A. A. et al. (2024a) Electret composite materials based on polyethylene and petroleum asphaltenes. *IEEE Transactions on Dielectrics and Electrical Insulation*, 31 (5), 2335–2342. https://doi.org/10.1109/TDEI.2024.3434774 (In English)

Galikhanov, M. F., Zhang, X., Ma, X. et al. (2024b) The effect of modifier on electret properties and hardness of epoxy composite material. *IEEE Transactions on Dielectrics and Electrical Insulation*, 31 (5), 2343–2349. https://doi.org/10.1109/TDEI.2024.3452655 (In English)

Goldade, V. A., Kovalenko, M. A., Garbaruk, V. Yu. et al. (2020) Formirovanie i relaksatsiya zaryada v nanokompozitakh na osnove polietilena [Formation and relaxation of charge in nanocomposites based on polyethylene]. *Vestnik Grodnenskogo gosudarstvennogo universiteta im. Yanki Kupaly. Seriya 6. Tekhnika — Vesnik of Yanka Kupala State University of Grodno. Series 6. Engineering Science*, 10 (2), 52–63. (In Russian)

Goldade, V. A., Kovalenko, M. A, Zotov, S. V. (2021) Electret charge in nanocomposites based on polyethylene. *International Scientific Journal Theoretical & Applied Science*, 193 (11), 759–765. https://dx.doi.org/10.15863/TAS (In English)

Goldade, V. A., Zotov, S. V., Shapovalov, V. M. et al. (2019) Electret effect in polymer nanocomposites (review). *Polymer Materials and Technologies*, 5 (2), 6–18. https://doi.org/10.32864/polymmattech-2019-5-2-6-18 (In English)

Gorokhovatskij, Yu. A. (1991) *Termoaktivacionnaya tokovaya spektroskopiya vysokoomnyh poluprovodnikov i dielektrikov [Thermally activated current spectroscopy of high-resistance semiconductors and dielectrics].* M.: Nauka publ., 248 p. (In Russian)

Gorokhovatskij Yu. A., Demidova N. S., Temnov D. E. (2020) Electric charge relaxation in the polyethylene with mineral inclusions of diatomite. *St. Petersburg Polytechnical State University Journal. Physics and Mathematics*, 13 (2), 9–16. https://doi.org/10.18721/JPM.13201 (In English)

Gorokhovatskij Yu. A., Sotova Yu. I., Temnov D. E. (2022) A study of charge relaxation in corona electrets based on P(VDF-TFE) copolymer. *Physics of Complex Systems*, 3 (3), 104–108. https://doi.org/10.33910/2687-153X-2022-3-3-104-108 (In English)

Guliakova, A., Henderyckx, A., Shishkin, N. et al. (2024) Influence of crystallinity and isotacticity on charge decay of polypropylene homopolymer blends. *IEEE Transactions on Dielectrics and Electrical Insulation*, 31 (5), 2358–2364. https://doi.org/10.1109/TDEI.2024.3417953 (In English)

Kara, Y., Molnár, K. (2021) A review of processing strategies to generate melt-blown nano/microfiber mats for high-efficiency filtration applications. *Journal of Industrial Textiles*, 51, 137–180. https://doi.org/10.1177/15280837211019488 (In English)

Kestelman, V. N. (2000) *Electrets in Engineering: Fundamentals and Applications*. New York: Springer Publ., 281 p. https://doi.org/10.1007/978-1-4615-4455-5 (In English)

Kovalenko, M. A., Goldade, V. A. (2021) Electret properties of nanocomposites based on polyethylene and polylactide. In: *Proceedings of the 8th International Scientific and Practical Conference "International Forum: Problems and Scientific Solutions"*. Melbourne: CSIRO Publ., pp. 295–303. (In English)

Kovalenko, M. A., Goldade, V. A., Zotov, S. V. et al. (2023) Elektretnoe sostoyanie v nanokompozitakh na osnove polilaktida [Electret state in nanocomposites based on polylactide]. *Problemy fiziki, matematiki i tekhniki — Problems of Physics, Mathematics and Technics*, 2 (55), 20–24. (In Russian)

Li, X., Wang, Y., Xu, M. et al. (2021) Polymer electrets and their applications. *Journal of Applied Polymer Science*, 138 (19), article 50406. https://doi.org/10.1002/app.50406 (In English)

Minzagirova, A. M., Galikhanov, M. F., Khayrullin, R. Z. (2021) Influence of montmorillonite on the change of electret properties of polypropylene. *The VIII International Young Researchers' Conference — Physics, Technology, InnovationS (PTI-2021)*, 2466 (1), article 060023. https://doi.org/10.1063/5.0089012 (In English)

Pinchuk, L. S. (2012) *Melt blowing: Equipment, technology, and polymer fibrous materials*. Berlin: Springer Publ., 224 p. https://doi.org/10.1007/978-3-642-55984-6 (In English)

Xiao, H. (2015) Study on correlation of filtration performance and charge behavior and crystalline structure for melt-blown polypropylene electret fabrics. *Journal of Applied Polymer Science*, 132 (47), article 42807. https://doi.org/10.1002/app.42807 (In English)

Zhang, J. (2020) Electret characteristics of melt-blown polylactic acid fabrics for air filtration application. *Journal of Applied Polymer Science*, 137 (4), article 48309. https://doi.org/10.1002/app.48309 (In English)

Physics of Semiconductors. Semiconductors

UDC 621.382.323

EDN TUEBOO
https://www.doi.org/10.33910/2687-153X-2025-6-1-26-34

Modelling the behavior of metal-oxide-semiconductor structures under thermal field treatment

O. V. Aleksandrov [1], N. N. Morozov ✉[1]

[1] St. Petersburg State Electrotechnical University 'LETI' named after V. I. Ulyanov (Lenin),
5 Professora Popova Str., Saint Petersburg 197022, Russia

Authors

Oleg V. Aleksandrov, ORCID: 0009-0008-1016-1031, e-mail: Aleksandr_ov@mail.ru

Nikita N. Morozov, ORCID: 0009-0001-3655-4860, e-mail: laughter-maiden@mail.ru

For citation: Aleksandrov, O. V., Morozov, N. N. (2025) Modelling the behavior of metal-oxide-semiconductor structures under thermal field treatment. *Physics of Complex Systems*, 6 (1), 26–34. https://www.doi.org/10.33910/2687-153X-2025-6-1-26-34
EDN TUEBOO

Received 26 August 2024; reviewed 9 October 2024; accepted 9 October 2024.

Funding: The study did not receive any external funding.

Abstract. A quantitative model of the behavior of metal-oxide-semiconductor (MOS) structures subjected to thermal field treatment, particularly in the accumulation and recovery modes of mobile charge in the gate dielectric, is presented. The mobile charge transport is modelled based on ion trapping on polyenergetic defects with a spectrum of binding energies. The time-dependent shifts in the threshold voltage of the MOS structures under positive and subsequent negative gate biases are simulated. The proposed model accounts for both symmetric and asymmetric behaviours observed in MOS structures containing Na^+ ions. Additionally, the model determines the range of binding energies, trap concentrations, and the spatial localization of traps.

Keywords: MOS structure, gate dielectric, mobile charge, thermal field treatment, dispersion transport, polyenergetic traps, amorphous silicon dioxide, modeling

Introduction

Positive Bias Temperature Instability (PBTI) may be observed during thermal field treatment (TFT) of MOS structures with a positive gate voltage (Grasser 2014; Zhang et al. 2022). This phenomenon is associated with the transport of mobile impurity ions of alkaline earth metals, primarily sodium (Na^+), from the gate to the silicon (Si) substrate in the electric field of the gate dielectric. Two primary models have been proposed to describe the kinetics of mobile charge accumulation during TFT: Snow's diffusion model (Snow et al. 1965), and Hofstein's interface trapping model (Hofstein 1966). In Show's model, the transfer of mobile charge from the gate to the Si substrate is governed by the diffusion and drift rates of free impurity ions in the dielectric. The accumulated mobile charge is proportional to the square root of the TFT duration:

$$Q \sim \sqrt{t}. \quad (1)$$

In Hofstein's model, the rate of charge accumulation is determined by the release rate of impurity from the interphase boundary (IPB) between the dielectric and the gate. In this case:

$$Q = Q_0(1 - \exp(-t / \tau)), \tag{2}$$

where Q_0 is the initial charge, τ is the time constant, $\tau^{-1} = \nu \exp(-\frac{E}{kT})$, ν is the frequency factor, E is the binding energy, T is the TFT temperature, k is the Boltzmann constant ($k = 8.617 \times 10^{-5}$ eV/K).

When the polarity is reversed, the charge near the Si substrate decreases (or is restored) as the mobile ions return to the gate. According to the diffusion model, this process should occur at the same rate as the accumulation, resulting in symmetric behavior. Conversely, the boundary capture model suggests that restoration occurs much faster than accumulation, reflecting asymmetric behavior due to the high speed of free impurity transport. In practice, both behaviors are observed, and the kinetics of accumulation and restoration deviate from the simple dependencies described by equations (1) and (2) (Hofstein 1966; Snow et al. 1965).

These deviations may be attributed to the capture of impurity by traps in the dielectric, which slows the rate of impurity ion transfer (Aleksandrov, Morozov 2023). Moreover, in the case of amorphous silicon dioxide, these traps are not monoenergetic, but polyenergetic, exhibiting a distribution (or dispersion) in binding energies. The dispersive transport of charge carriers in amorphous materials can be modeled by multiple capture events involving polyenergetic traps (Noolandi 1977). For amorphous silicon dioxide, these traps may include oxygen vacancies or other structural defects.

The aim of this work is to develop a quantitative model for the behavior of MOS structures during TFT, focusing on the capture of mobile impurity ions by polyenergetic traps in the gate oxide. The model also simulates time-dependent shifts in the threshold voltage.

Model equations

The gate dielectric of the MOS structure (amorphous silicon dioxide, SiO_2) contains structural defects, such as oxygen vacancies, which can serve as polyenergetic traps for mobile impurity ions. It is assumed that during their transport, impurity ions can be captured by neutral traps, T_i^0, within the volume of silicon dioxide, leading to the formation of positively charged complexes NT_i^+:

$$N^+ + T_i^0 \underset{k_{2i}}{\overset{k_{1i}}{\rightleftarrows}} NT_i^+, i = 1,2\ldots n, \tag{3}$$

where k_{1i} and k_{2i} are the rate constants for the direct and reverse reactions of the impurity with the i-th trap. The system of diffusion-drift continuity equations and the Poisson equation, describing the transport of impurity ions and their capture by polyenergetic traps in accordance with reaction (3), is as follows:

$$\frac{\partial C_N^+}{\partial t} = D\frac{\partial^2 C_N^+}{\partial x^2} - \mu\frac{\partial}{\partial x}(C_N^+ \cdot E) - C_N^+ \sum_{i=1}^{n} k_{1i} C_{Ti}^0 + \sum_{i=1}^{n} k_{2i} C_{NTi}^+, \tag{4}$$

$$\frac{\partial C_{NTi}^+}{\partial t} = -\frac{\partial C_{Ti}^0}{\partial t} = k_{1i} C_{Ti}^0 C_N^+ + k_{2i} C_{NTi}^+, i = 1,2\ldots n, \tag{5}$$

$$\frac{\partial^2 V}{\partial x^2} = -\frac{\rho}{\varepsilon\varepsilon_0} = -\frac{q}{\varepsilon\varepsilon_0}(C_N^+ + \sum_{i=1}^{n} C_{NTi}^+), \tag{6}$$

where x is the coordinate ($x = 0$ on the Si-SiO_2 IPB and $x = d$ on the SiO_2-metal gate IPB, d is the oxide thickness); t is the TFT time; C_N^+ is the concentration of free impurity ions N^+, C_{Ti}^0 is the concentration of neutral traps T_i^0, C_{NTi}^+ is the concentration of positively charged complexes NT_i^+; V is the potential distribution in the dielectric; E is the electric field strength, $E = -dV/dx$; D is the diffusion coeff 2c icient of free ions; μ is the ion mobility; ($\mu = D/(kT)$ according to the Einstein relation), q is the elementary charge ($q = 1.6 \cdot 10^{-19}$ C); ε is the relative permittivity of the dielectric ($\varepsilon(SiO_2) = 3.9$); ε_0 is the electric constant ($\varepsilon_0 = 8.85 \cdot 10^{-12}$ F/m).

The mobility of impurity ions in amorphous SiO_2 is described by the Arrhenius equation:

$$\mu = \mu_0 \exp(-\frac{E_a}{kT}), \tag{7}$$

where μ_0 is the pre-exponential factor, and E_a is the activation energy. The mobility of Na^+ ions in SiO_2 was determined in (Stagg 1977) using the thermally stimulated ion current method in the fields up to $E = 5 \times 10^5$ V/cm, $\mu_0 = 1.05$ cm^2/V×s, $E_a = 0.66$ eV.

We assume that the capture of an ion by different traps T^0_i is equally probable, and under diffusion limitation, the rate constant of the forward reaction (3) is determined by the diffusion coefficient of free ions: $k_{1i} = k_1 = 4\pi RD$, where R is the effective radius of ion capture by a trap (we assume $R \cong 1$ Å). The reverse reaction occurs at a rate that depends on the binding energy of the ion with the i-th trap E_{bi}: $k_{2i} = \nu \exp(-\frac{E_{bi}}{kT})$, where ν is the vibration frequency of atoms, $\nu = 10^{12}$ s^{-1}. The binding energy is distributed within the range from E_{b1} to E_{bn}: $E_{bi} = E_{b1} + \Delta E_{bi} \cdot (i-1), i = 1,2\ldots n,$ where $\Delta E_{bi} = dE_{bi} = \frac{E_{bn} - E_{b1}}{n}$, is the energy increment.

We assume that the distribution of traps by energy follows an exponential form, characteristic of amorphous materials (Arkhipov, Rudenko 1982):

$$\frac{\partial C_{Ti}(x, E_{bi})}{\partial E_{bi}} = C_T(x)\frac{1}{E_0}\exp(-\frac{E_{bi}}{E_0}), i = 1,2\ldots n, \tag{8}$$

where E_0 is the characteristic energy corresponding to the width of the energy distribution of traps, $C_{Ti}(x, E_{bi})\varnothing E_{bi}$ is the concentration of traps with energies from E_{bi} to $E_{bi} + \Delta E_{bi}$, and $C_T(x)$ is the distribution of traps along the coordinate without taking into account the energy distribution, which we assume to be exponential near both IPBs:

$$C_T(x) = \frac{Q'_{TSi}}{L_{Si}}\exp(-\frac{x}{L_{Si}}) + \frac{Q'_{TMe}}{L_{Me}}\exp(-\frac{d-x}{L_{Me}}), \tag{9}$$

where Q'_{TSi}, Q'_{TMe} are the integral concentrations of traps near the Si-SiO_2 and SiO_2-gate IPBs, respectively, without taking into account the energy distribution, and L_{Si} and L_{Me} are the widths of the corresponding exponential distributions of traps.

By summing equations (8) over energies and replacing the sum with an integral, we obtain an expression for the total concentration of traps in the selected range E_{b1} — E_{bn}:

$$C_{Tsum}(x) = \sum_{i=1}^{n} C_{Ti}(x, E_{bi})\Delta E_{bi} = \int_{E_{b1}}^{E_{bn}} C_{Ti}(x, E_{bi})dE_{bi} = \\ = C_T(x)(\exp(-\frac{E_{b1}}{E_0}) - \exp(-\frac{E_{bn}}{E_0})). \tag{10}$$

The integral concentrations of traps in this range from equations (9) and (10) can be expressed as:

$$Q_{TSi} = Q'_{TSi}(\exp(-\frac{E_{b1}}{E_0}) - \exp(-\frac{E_{bn}}{E_0})), \tag{11}$$

$$Q_{TMe} = Q'_{TMe}(\exp(-\frac{E_{b1}}{E_0}) - \exp(-\frac{E_{bn}}{E_0})). \tag{12}$$

We assume that at the initial moment of time, the charged complexes are in equilibrium with free impurity ions and neutral traps:

$$k_1 C^0_{Ti} C^+_N = k_{2i} C^+_{NTi}, i = 1,2\ldots n, \tag{13}$$

 https://www.doi.org/10.33910/2687-153X-2025-6-1-26-34

Replacing $C^0_{Ti}(x) = C^0_{Ti}(x, E_{bi})\Delta E_{bi} - C^+_{NTi}(x)$, $\sum_{i=1}^{n} C^+_{NTi}(x) = C^+_{Nsum}(x) - C^+_N(x)$ and summing (14) over i, we get:

$$C^+_N(x)(1 + \sum_{i=1}^{n} \frac{C_{Ti}(x, E_{bi})\Delta E_{bi}}{C^+_N(x) + \frac{k_{2i}}{k_1}}) = C^+_{Nsum}(x). \quad (14)$$

Solving equation (14) using the bisection method, we find the distributions of $C^+_N(x)$, $C^0_{Ti}(x)$, and $C^+_{NTi}(x)$ in the equilibrium for a given TFT temperature at the initial time $t = 0$.

The boundary conditions are assumed to be a constant gate bias and dielectric boundaries that reflect the impurity ions:

$$V(d,t) = V_G, \quad (15)$$

$$j(0,t) = j(d,t) = 0, \quad (16)$$

where j is the flux of impurity ions, $j(x,t) = -D\frac{\partial C^+_N}{\partial x} + \mu C^+_N E$.

To assess the influence of mobile ions accumulation on the behavior of the MOS structure, the effective amount of impurity ΔQ_{ot} and the threshold voltage shift ΔV_{th} (equal to the flat-band voltage shift ΔV_{fb}) near the SiO_2-Si MOS IPB are calculated:

$$\Delta Q_{ot}(t) = \int_0^d (C^+_{Nsum}(x,t) - C^+_{Nsum}(x,0))\frac{d-x}{d}dx, \quad (17)$$

$$\Delta V_{th}(t) = \frac{q}{C_{ox}}\Delta Q_{ot}(t), \quad (18)$$

where $C_{ox} = \varepsilon\varepsilon_0/d$ is the specific capacitance of the dielectric.

The system of equations of model (4)–(6) with the initial condition (14) and boundary conditions (15)–(16), taking into account equation (8), was solved numerically using both explicit and implicit difference schemes.

Calculation results and discussion

The calculation results were compared with the experimental data from (Kriegler, Devenyi 1973) and (Snow et al. 1965) on the TFT of MOS structures contaminated with Na^+ ions. In (Kriegler, Devenyi 1973), the MOS structure had an aluminum gate, with the gate oxide formed by thermal oxidation in dry oxygen at a temperature of 1150 °C, resulting in a thickness of 120 nm. Sodium was introduced into the structure during the deposition of aluminum at an approximate concentration of 10^{12} cm^{-2}. TFT measurements were performed at temperatures of 75 °C, 120 °C, and 175 °C, with a gate bias of $V_G = +2$ V in the charge accumulation mode and at $V_G = -1$ V in the subsequent recovery mode.

Figure 1 shows the kinetics of threshold voltage shift as a function of time in the accumulation mode on the silicon substrate. Curves 1–3 represent experimental dependences from (Kriegler, Devenyi 1973), while curves 1'–3' show calculations for monoenergetic traps at $E_b = 1.14$ eV following (Aleksandrov, Morozov 2023), and curves 1"–3" represent calculations for polyenergetic traps at $E_{b1} = 0.9$ eV, $E_{bn} = 1.4$ eV, $E_0 = 0.25$ eV. The comparison in Figure 1 reveals that calculations incorporating polyenergetic traps, in contrast to those based on monoenergetic traps, better represent the experimental data.

The lower limit of the energy range of the traps was initially set to the activation energy of Na^+ ions mobility ($E_{b1} = E_a = 0.66$ eV, as reported by (Stagg 1977)), but was subsequently adjusted to 0.9 eV, since at lower values of E_{b1} the calculation results do not change, due to the rapid depletion of traps with small E_{b1}. The upper limit of the range $E_{bn} = 1.4$ eV was taken to be equal to the highest activation energy experimentally recorded for the diffusion of sodium ions following (Sugano et al. 1968). The number of trap

energy levels within the range was taken to be $n \geq 30$, ensuring that the solution became independent of n.

The obtained range of 0.9-1.4 eV corresponds to the activation energy range for the 'slow' diffusion of sodium ions, as described in (Verwey et al. 1990). The narrow distribution of traps near the gate (L_{Me} = 2 nm) was selected to reflect the fact that, at negative V_G, no significant shift in the threshold voltage was observed during TFT, with the voltage shift measured as ΔV_{th} = 3 mV at T = 120 °C, V_G = –2 V). The appearance of the calculated dependences at temperatures of 75 °C and 120 °C resembles the root function (1) of Snow's model (Snow et al. 1965), while at 175 °C, the behavior aligns more closely with the function (2) of Hofstein's model (Hofstein 1966).

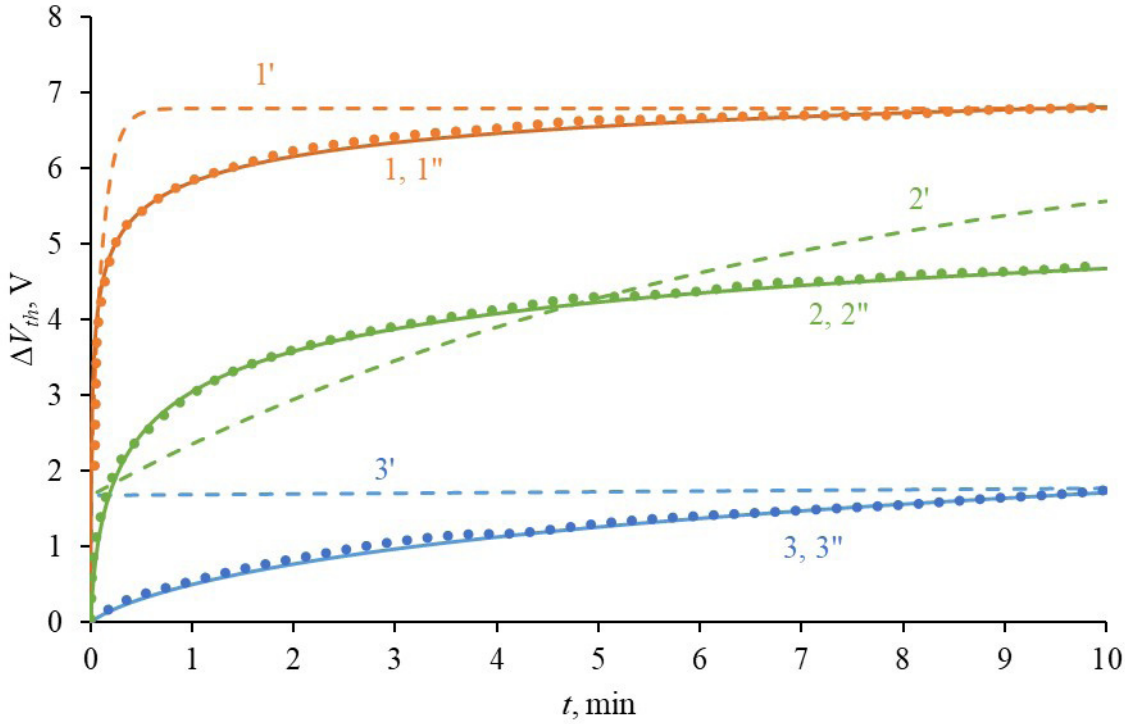

Fig. 1. Dependences of $\Delta V_{th}(t)$ during TFT (accumulation mode V_G = +2 V, d = 120 nm) at temperatures, °C: 1, 1', 1" — 175; 2, 2', 2" — 120; 3, 3', 3" — 75 °C. Curves 1–3 — experimental data from (Kriegler, Devenyi 1973); 1'–3' — calculations for monoenergetic traps (E_b = 1.14 eV, Q_{N^+Me} = 1.25 × 10^{12} cm^{-2}, Q_{TMe} = 9.4 × 10^{11} cm^{-2}); 1"–3" — calculations for polyenergetic traps (E_{b1} = 0.9 eV, E_{bn} = 1.4 eV, E_0 = 0.25 eV, Q_{N^+Me} = 1.4 × 10^{12} cm^{-2}, Q_{TMe} = 2.13 × 10^{12} cm^{-2})

In (Snow et al. 1965), the MOS structure was contaminated with sodium prior to sintering the aluminum gate. The gate oxide thickness was 200 nm. TFT measurements were performed at temperatures of 80 °C, 100 °C, 120 °C, 140 °C, and 160 °C with a gate bias of V_G = +10 V for one hour.

Figure 2 shows the experimental data (symbols 1–4) from (Snow et al. 1965) and the calculated dependences (curves 1'–4') between the effective charge and the $Q_{ot}(t^{1/2})$ during TFT. It is evident from Figure 2 that the experimental dependences from (Snow et al. 1965) deviate from both Snow's model (1) and Hofstein's model (2), but are satisfactorily described by the proposed model based on polyenergetic traps, with the same parameters used in Figure 1 as in (Kriegler, Devenyi 1973), i. e., E_{b1} = 0.9 eV, E_{bn} = 1.4 eV, E_0 = 0.25 eV.

The kinetics of the threshold voltage change during the recovery mode at V_G = –1 V (following the accumulation mode at V_G = +2 V, T = 120 °C, t = 10 min) is shown in Figure 3 (curve 1) based on the data from (Kriegler, Devenyi 1973). Curves 2 and 3 show the calculation using the polyenergetic trap model with the same trap parameters at the gate as those in Figure 1. These calculations are performed both in the absence of traps in silicon (curve 2, Q_{TSi} = 0) and with a small number of traps present (curve 3, Q_{TSi} = 2.36 × 10^{11} cm^{-2}). The trap parameters in silicon are identical to those at the gate (E_{b1} = 0.9 eV, E_{bn} = 1.4 eV, E_0 = 0.25 eV), except for the distribution width, which was taken to be L_{Si} = 5 nm, according to the data from (DiMaria 1977).

 https://www.doi.org/10.33910/2687-153X-2025-6-1-26-34

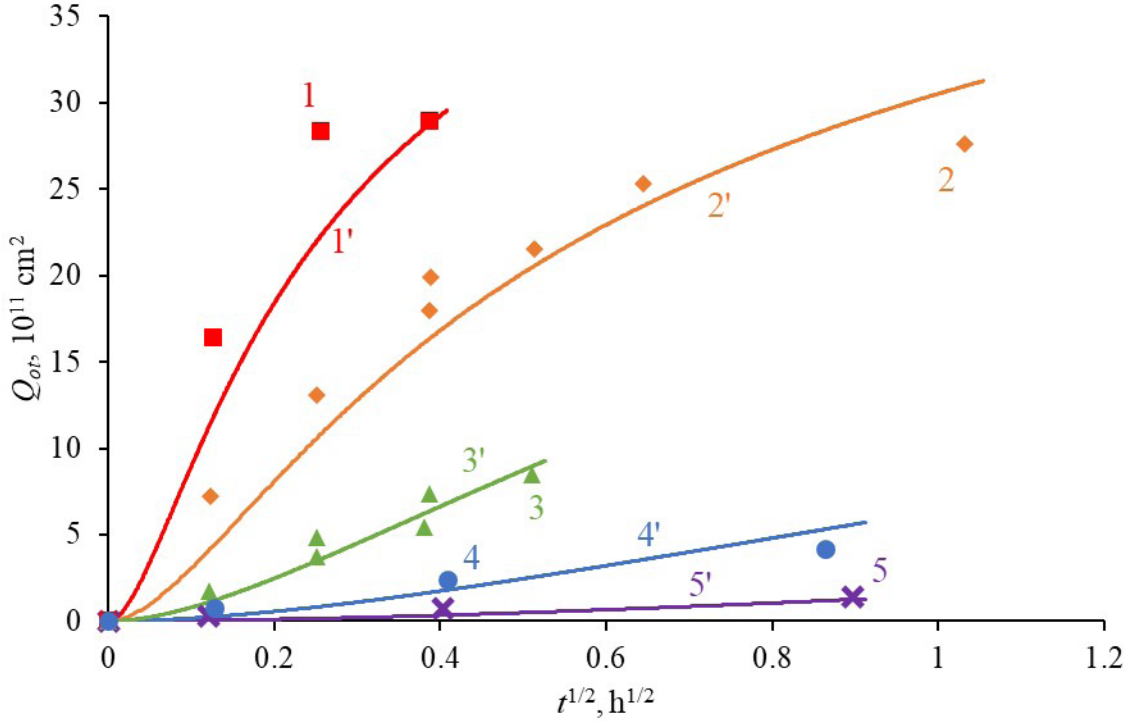

Fig. 2. $Q_{ot}(t^{1/2})$ dependences during TFT (accumulation mode V_G = +10 V, d = 200 nm) for temperatures, °C: 1, 1' — 160; 2, 2' — 140; 3, 3' — 120; 4, 4' — 100; 5, 5' — 80. Curves 1–5 — experimental data (Snow et al. 1965); 1'–5' — calculation for polyenergetic traps (E_{b1} = 0.9 eV, E_{bn} = 1.4 eV, E_0 = 0.25 eV, $Q_{N^+_{Me}}$ = 5.3 × 10^{12} cm^{-2}, Q_{TMe} = 2.24 × 10^{13} cm^{-2})

As shown in Figure 3, recovery occurs much faster than accumulation, indicating asymmetric behavior. The initial rapid voltage drop is caused by the drift of free impurity from the Si-SiO_2 IPB, with the slope of this drop characterized by the mobility of free ions. In the case of no traps near silicon (curve 2), at t > 0.2 s, the threshold voltage is completely restored to V_{th} = 0 ($|\Delta V_{th}| = \Delta V_{th}$ (at $+V_G$)). However, when traps are present near silicon (curve 3), the threshold voltage does not fully recover, as the impurity ions are captured by traps near the boundary with silicon. Among the available literature data on the diffusion coefficient of free sodium ions (Greeuw, Verwey 1984; Hofstein 1967; Kriegler, Devenyi 1976; Stagg 1977; Sugano et al. 1968; Verwey et al. 1990), the data from (Stagg 1977) provide the best correlation with the experimental observations in the region of fast drift.

The asymmetry observed in the charge accumulation and recovery dependencies $\Delta V_{th}(t)$ in Figures 1–3 within the framework of the model can be explained by two factors: first, the initial position of Na^+ ions on traps near the gate, and, second, the relatively low concentration of traps near the Si-SiO_2 IPB (Q_{TSi} = 2.36 × 10^{11} cm^{-2}) for silicon oxide obtained by thermal oxidation in dry oxygen.

In contrast, when 'chlorine' oxides are used, which are obtained by thermal oxidation in the presence of HCl vapor, a more symmetrical accumulation-reduction time dependences are observed during TFT. This symmetry is attributed to an increase in the concentration of traps near silicon, which slows down the drift of sodium ions during the reduction mode under a negative bias. In (Kriegler, Devenyi 1973), along with standard samples with oxide produced by thermal oxidation in dry oxygen (see Figs. 1 and 3), samples with chlorine oxide were also studied. The thermal oxidation of these samples was performed at a temperature of 1150 °C in an atmosphere containing 6% HCl: O_2. The oxide films formed were 115 nm thick. TFT in the recovery mode was carried out at temperatures of 250 °C, 225 °C, 200 °C, and 175 °C with a gate bias of V_G = –2 V (after applying V_G = +2 V at T = 200 °C for t = 5 min). The amount of charge $Q_{ion} = qQ_{ot}A$ that moved from silicon with a negative bias to the gate with an area of A = 0.025 cm^2 was measured. Under a positive bias during the accumulation mode, the experimental dependences $\Delta V_{th}(t)$ for both the standard and chlorine oxides, as reported in (Kriegler, Devenyi 1973), were identical. This indicates that the defects induced by chlorine are concentrated near the SiO_2-Si IPB and do not impact the drift of sodium ions from the gate to silicon.

Figure 4 shows the calculated $Q_{ion}(t)$ dependencies for chlorine oxide in the reduction mode.

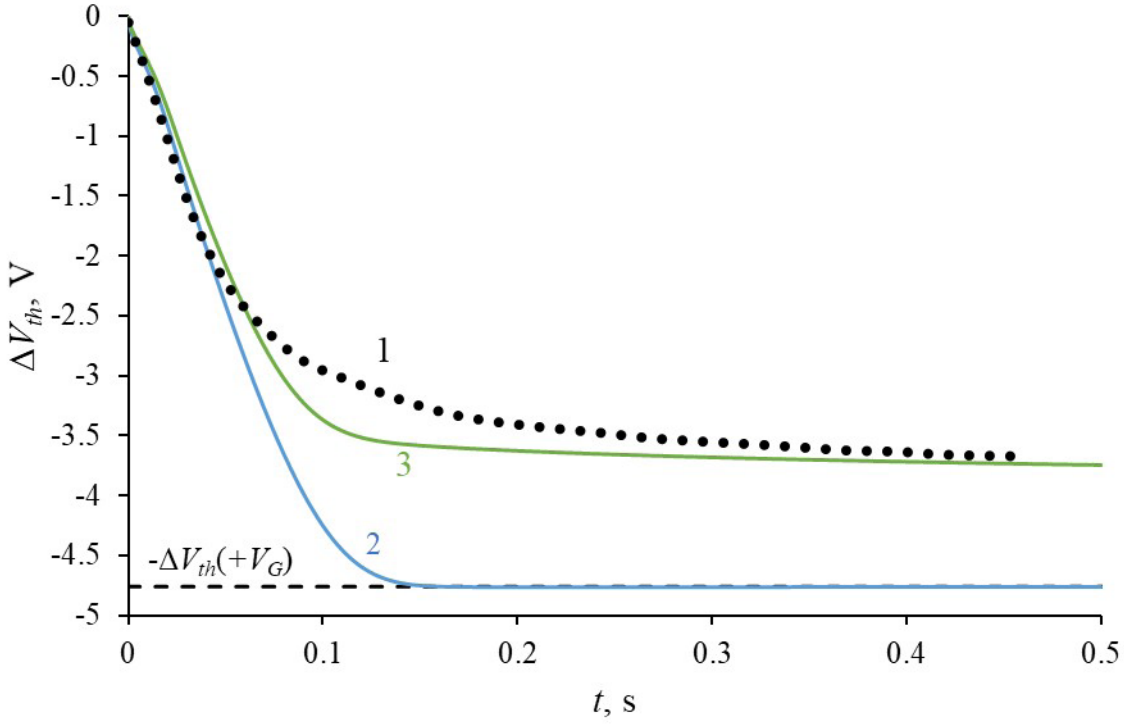

Fig. 3. Dependence of $\Delta V_{th}(t)$ during TFT (recovery mode, V_G = –1 V, T = 120 °C, d = 120 nm). Curve 1 — experimental data (Kriegler, Devenyi 1973); curve 2 — calculation based on the model with no traps near silicon, Q_{TSi} = 0; curve 3 — calculation based on the model with traps near silicon, Q_{TSi} = 2.36·10^{11} cm^{-2}, L_{Si} = 5 nm. The trap parameters near the gate are the same as those in Figure 1

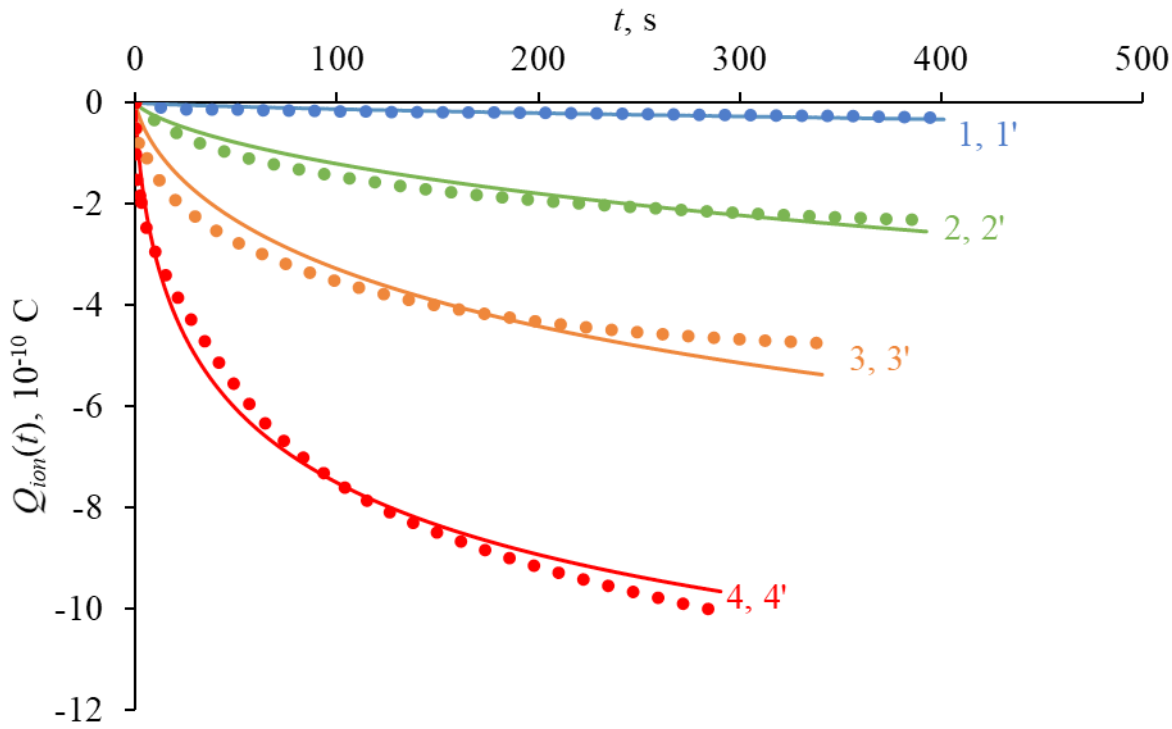

Fig. 4. $Q_{ion}(t)$ dependences during TFT (reduction mode, V_G = –2 V, d = 115 nm, $A \approx 0.025$ cm^2) for temperatures, °C: 1, 1' — 175; 2, 2' — 200; 3, 3' — 225; 4, 4' — 250. Curves 1–4 — experimental data (Kriegler, Devenyi 1973); 1'–4' — calculation for Q_{N^+Si}, cm^{-2}: 1' — 3.7 × 10^{11}; 2' — 4.6 × 10^{11}; 3' — 4.7 × 10^{11} cm^{-2}; 4' — 5.1 × 10^{11} (Q_{TSi} = 3.51 × 10^{12} cm^{-2}, E_{b1} = 0.9 eV, E_{bn} = 2 eV, E_0 = 0.25 eV, L_{Si} = 5 nm)

 https://www.doi.org/10.33910/2687-153X-2025-6-1-26-34

The calculation shows that, for the given parameters of the preliminary positive bias, almost all the impurity migrates from the gate to the substrate (Q_{Nsum} = 1.4 × 10^{12} cm^{-2}). Consequently, the recovery calculation was performed assuming an initial impurity distribution on traps near silicon in the local equilibrium state at the corresponding TFT temperatures. The experimental curves were obtained by varying Q_{N^+Si}, while maintaining a constant number of traps near silicon Q_{TSi} = 3.5 × 10^{12} cm^{-2} (curve 1'–4'), using the same parameters of polyenergetic traps (E_0 = 0.25 eV, E_{b1} = 0.9 eV), but with a higher E_{bn} = 2 eV. The distribution width L_{Si} = 5 nm was taken from the experiment (DiMaria 1977). From the values obtained for curves 1'–4' (Q_{N^+Si} = (5.1 – 3.7) × 10^{11} cm^{-2}), it is evident that the integral amount of impurity Na^+ ions in the chloride oxide, when moving from silicon (with a negative bias), is less than when migrating to silicon (with a positive bias). This suggests neutralization of some Na^+ ions located on traps close to the SiO_2-Si IPB. As established in (Aleksandrov 2015; Dmitriev, Markin 1998), neutralization occurs due to the capture of electrons from the silicon substrate:

$$Na^+ + T^0 + e^- \underset{k_2'}{\overset{k_1'}{\rightleftarrows}} NT^0.$$

We assume that the formation of the inactive part of the impurity $Q_N' = Q_{Nsum} - Q_N$ is limited by the slower reaction of the impurity ions with the traps and is in equilibrium with them:

$$C_{NT}^0 = \frac{k_1'}{k_2'} C_N^+ C_T^0,$$

$$Q_N' = \frac{k_1'}{k_2'} Q_N Q_T / L,$$

$$k_2' = \frac{k_1'}{Q_N'} Q_N Q_T / L.$$

At $k_1' = k_1$, using the temperature dependence $k_2' = \nu' \exp(-\frac{E_b'}{kT})$, we find the binding energy of sodium in such neutral traps: E_b' = 0.82 eV, which is close to the lower limit of binding energies for polyenergetic traps (E_{b1} = 0.9 eV).

Conclusions

A quantitative model of the behavior of MOS structures during thermal field treatment has been developed based on the mechanism of capturing mobile impurity ions by polyenergetic traps in the bulk of the gate dielectric. At a positive gate voltage, the kinetics of charge accumulation in the IPB with silicon is determined by the rate of impurity ion release from polyenergetic traps in the IPB with a gate (Figs. 1 and 2). The parameters of these traps (E_{b1} = 0.9 eV, E_{bn} = 1.4 eV, E_0 = 0.25 eV), their concentrations, and the width of the localization region (L_{Me} = 2 nm) have been determined from experimental temperature dependences (Kriegler, Devenyi 1973; Snow et al. 1965).

Upon a subsequent change in polarity, the kinetics of charge recovery depends on the presence of traps near Si-SiO_2 IPB. In the absence of traps (Fig. 3, curve 2) or their low concentration for dry oxide (Fig. 3, curve 3), the recovery rate is high (showing asymmetric behavior) and is determined by the drift velocity of free impurity ions, as well as the internal field of ions. With a high concentration of traps in the chloride oxide near Si-SiO_2 IPB, the recovery rate becomes significantly slower (Fig. 4) and is comparable to the accumulation rate (indicating symmetric behavior). In this case, the recovery rate is determined by the rate of impurity ion release from polyenergetic traps near Si-SiO_2 IPB (Fig. 4). The parameters of the traps (E_{b1} = 0.9 eV, E_{bn} = 2.0 eV, E_0 = 0.25 eV), their concentrations, and the width of the localization region (L_{Si} = 5 nm) were determined by comparing the calculations with the experimental temperature dependences (Kriegler, Devenyi 1973). It was found that neutralization of a part of the ionized impurity occurs in chlorine oxide, and the binding energy of the Na impurity on such traps is calculated to be E_b' = 0.82 eV.

Conflict of Interest

The authors declare that there is no conflict of interest, either existing or potential.

Author Contributions

O. V. Alexandrov formulated the research problem, while N. N. Morozov carried out the calculations. Both authors analyzed the results and discussed the conclusions.

References

Aleksandrov, O. V. (2015) On the effect of bias on the behavior of MOS structures subjected to ionizing radiation. *Semiconductors*, 49 (6), 774–779. https://doi.org/10.1134/S1063782615060020 (In English)

Aleksandrov, O. V., Morozov, N. N. (2023) Influence of traps on mobile charge accumulation in MOS structures in thermal field treatments. *LETI Transactions on Electrical Engineering & Computer Science*, 16 (6), 20–28. https://doi.org/10.32603/2071-8985-2023-16-6-20-28 (In Russian)

Arkhipov, V. I., Rudenko, A. I. (1982) Drift and diffusion in materials with traps: II. Non-equilibrium transport regime. *Philosophical Magazine B*, 45 (2), 189–207. https://doi.org/10.1080/13642818208246327 (In English)

DiMaria, D. J. (1977) Room-temperature conductivity and location of mobile sodium ions in the thermal silicon dioxide layer of a metal-silicon dioxide-silicon structure. *Journal of Applied Physics*, 48 (12). 5149–5151. https://doi.org/10.1063/1.323594 (In English)

Dmitriev, S. G., Markin, Yu. V. (1998) Manifestations of the deneutralization of mobile charges in SiO_2 in the spectroscopy of the silicon-oxide interface. *Semiconductors*, 32 (12), 1289–1292. https://doi.org/10.1134/1.1187616 (In English)

Grasser, T. (2014) *Bias temperature instability for devices and circuits*. New York: Springer Publ., 810 p. https://doi.org/10.1007/978-1-4614-7909-3 (In English)

Greeuw, G., Verwey, J. F. (1984) The mobility of Na^+, Li^+, and K^+ ions in thermally grown SiO_2 films. *Journal of Applied Physics*, 56 (8), 2218–2224. https://doi.org/10.1063/1.334256 (In English)

Hofstein, S. R. (1966) An investigation of instability and charge motion in metal-silicon oxide-silicon structures. *IEEE Transactions on Electron Devices*, ED-13 (2), 222–237. https://doi.org/10.1109/T-ED.1966.15674 (In English)

Hofstein, S. R. (1967) Space-charge-limited ionic currents in silicon dioxide films. *Applied Physics Letters*, 10 (10), 291–293. https://doi.org/10.1063/1.1754816 (In English)

Kriegler, R. J., Devenyi, T. F. (1973) Temperature-bias aging of (HCl) MOS structures. In: *11th Reliability Physics Symposium*. Las Vegas: IEEE Publ., pp. 153–158. https://doi.org/10.1109/IRPS.1973.362587 (In English)

Kriegler, R. J., Devenyi, T. F. (1976) Direct measurement of Na^+ ion mobility in SiO_2 films. *Thin Solid Films*, 36 (2), 435–439. https://doi.org/10.1016/0040-6090(76)90057-2 (In English)

Noolandi, J. (1977) Equivalence of multiple-trapping model and time-dependent random walk. *Physical Review B*, 16 (10), 4474–4479. https://doi.org/10.1103/PhysRevB.16.4474 (In English)

Snow, E. H., Grove, A. S., Deal, B. E., Sah, C. T. (1965) Ion transport phenomena in insulating films. *Journal of Applied Physics*, 36 (5), 1664–1673. https://doi.org/10.1063/1.1703105 (In English)

Stagg, J. P. (1977) Drift mobilities of Na^+ and K^+ ions in SiO_2. *Applied Physics Letters*, 31 (8), 532–533. https://doi.org/10.1063/1.89766 (In English)

Sugano, T., Hoh, K., Kudo, K., Hishinuma, N. (1968) Ordered structure and ion migration in silicon dioxide films. *Japanese Journal of Applied Physics*, 7 (7), 715–730. https://doi.org/10.1143/JJAP.7.715 (In English)

Verwey, J. F., Amerasekera, E. A., Bisschop, J. (1990) The physics of SiO_2 layers. *Reports on Progress in Physics*, 53 (10), 1297–1331. https://doi.org/10.1088/0034-4885/53/10/002 (In English)

Zhang, J. F., Gao, R., Duan, M, et al. (2022) Bias temperature instability of MOSFETs: Physical processes, models, and prediction. *Electronics*, 11 (9), article 1420. https://doi.org/10.3390/electronics11091420 (In English)

Theoretical physics.
Theory of condensed matter

UDC 538.9

EDN DNZGSD
https://www.doi.org/10.33910/2687-153X-2025-6-1-35-48

Numerical simulations of Gaussian white noise and field-induced phase transition in bulk antiferroelectrics using parameters of ammonium dihydrogen phosphate

S.-Ch. Lim ✉[1]

[1] School of Physics, Universiti Sains Malaysia, 11800 USM, Penang, Malaysia

Author

Siew-Choo Lim, ORCID: 0000-0001-8397-0886, e-mail: sclim@usm.my

For citation: Lim, S.-Ch. (2025) Numerical simulations of Gaussian white noise and field-induced phase transition in bulk antiferroelectrics using parameters of ammonium dihydrogen phosphate. *Physics of Complex Systems*, 6 (1), 35–48. https://www.doi.org/10.33910/2687-153X-2025-6-1-35-48 EDN DNZGSD

Received 24 September 2024; reviewed 27 December 2024; accepted 27 December 2024.

Funding: The study did not receive any external funding.

Abstract. This paper presents phenomenological and numerical studies of Gaussian white noise and field-induced dynamical phase transitions in bulk antiferroelectrics (AFE), focusing on the delayed transition from AFE to ferroelectric (FE) states. The steady states of the AFE are formulated by applying the calculus of variations to the AFE thermodynamic potential, in the absense of external noise. Stochastic relaxation equations for the AFE are then derived using the Landau — Khalatnikov equation, where the AFE thermodynamic potential accounts for both Gaussian white noise and a sinusoidal time-dependent electric field. These equations are solved numerically using the stochastic fourth-order Runge — Kutta (SRK4) method. The results indicate that, for an applied field amplitude of 97% of the transition amplitude, additional Gaussian white noise with amplitudes < 8% of the applied field induces delayed AFE to FE phase transitions, with the time delay inversely proportional to the noise amplitudes.

Keywords: Gaussian white noise, stochastic fourth-order Runge — Kutta (SRK4) method, dynamical phase transition, antiferroelectrics, ferroelectrics

Introduction

Phase transitions in antiferroelectric (AFE) materials are typically characterized by a unique electric polarization that reverses direction at a critical temperature or applied electric field. Below the critical temperature, the AFE to ferroelectric (FE) phase transition occurs when both static and time-dependent electric fields increase beyond their respective critical thresholds. At various static field values, steady states of the AFE systems can be identified. These states exhibit hysteresis patterns in 2D plots of induced polarization versus applied static field. By observing these hysteresis patterns, the system's AFE and FE states can be distinguished. For time-dependent applied electric fields, sinusoidal or other periodic behaviors lead to what is called a dynamic field-induced phase transition, where the dynamic field can drive the system from one phase to another, typically from AFE to FE phases. These phase transitions manifest as abrupt changes in hysteresis patterns, shifting from AFE double hysteresis loops to FE single hysteresis loops (Lines, Glass 1977; Tolédano, Guennou 2016; Zhang et al. 2020; 2023).

In dynamic field-induced phase transitions, the effects of noise are inevitable. Sources of this noise may arise from fluctuating environmental conditions, non-ideal equipment, material degradation (such as aging), electrical interference, thermal fluctuations, imperfect control systems, and other random

disturbances (Garcia-Ojalvo, Sancho 1999; Gardiner 1985; Henkel, Pleimling 2010). Initially, stochastic effects on dynamical phase transitions were used to explain climatic transitions between ice ages and interglacials (Alexandrov et al. 2018; Benzi et al. 1981; Nicolis 1982). The theoretical study of noise-induced phase transitions has gained momentum in other physical systems. For example, in the cubic lattice model (Van den Broeck et al. 1994), spatially extended systems (Cao et al. 2007; Carrillo et al. 2003), and delayed triple-well potential systems (Jin, Xu 2020), among others. Stochastic transitions have also garnered significant interest in quantum systems, such as the system-reservoir model (Ghosh et al. 2005), mesoscopic metal rings (Tong, Vojta 2006), electronic Mach-Zehnder interferometers (Levkivskyi, Sukhorukov 2009), two-dimensional open quantum systems (Dagvadorj et al. 2015), quantum dots (Zhang et al. 2017), and hybrid quantum circuits (Liu et al. 2024), etc.

In this paper, we investigate both phenomenologically and numerically the effects of additional Gaussian white noise on field-induced delayed AFE to FE phase transitions in bulk AFE systems, such as ammonium dihydrogen phosphate (ADP). We first explore how electric fields, both static and time-dependent, influence these phase transitions, with particular attention to hysteresis patterns that help distinguish between AFE and FE states. We further examine the impact of Gaussian white noise on dynamic field-induced AFE to FE phase transitions by evaluating how the frequency and amplitude of the applied electric field, as well as the noise amplitude, affect hysteresis patterns, time series curves, and the delay of phase transition onset.

The study is divided into three parts. In the first part, the steady states of the AFE system are formulated using the bulk AFE thermodynamic potential with an applied static electric field, excluding noise (Lines, Glass 1977; Lim 2022). The resulting equations of state are solved numerically using a root-finding method (Press et al. 1996), and the results are presented graphically in 2D plots. These results serve as a baseline for distinguishing between the AFE and FE phases in the second and third parts of this paper.

In the second part, the adopted AFE thermodynamic potential incorporates Gaussian white noise and a sinusoidal time-dependent electric field. The nonlinear stochastic relaxation equations of the AFE system are formulated by applying the Landau — Khalatnikov equation to this thermodynamic potential. To numerically solve these nonlinear stochastic relaxation equations, we adopt the stochastic fourth-order Runge — Kutta (SRK4) method (Khodabin, Rostami 2015). In the numerical simulations, two sets of frequency and amplitude of the applied field are selected, with the selected amplitudes being smaller than the transition amplitudes without noise. For each set of frequency and amplitude, three sets of numerical data are generated to account for three different noise amplitudes. Specifically, the first two sets correspond to noise amplitudes below the critical value, while the third set corresponds to the critical noise amplitude. The generated data are plotted as time series and hysteresis curves. The abrupt changes in values and the patterns of the curves enable the identification of the transition from AFE to FE phases of the system.

The third part is an extension of the second part, using the same formalism and numerical scheme. The selected frequencies are the same as the frequencies chosen in the second part, but the selected field amplitudes are significantly greater than the transition amplitudes without noise. Two sets of numerical data are generated using the same SRK4 method to account for two moderate noise amplitudes. The generated data are plotted as time series and hysteresis curves, serving as a comparison with the results from the second part.

Part I. AFE and FE steady states in applied static fields

Before applying noise, it is necessary to identify the steady states of the system under a static applied field. The formalism is based on the Landau theory of first-order antiferroelectricity, adopted from previous work (Lim 2022), in which the dimensionless bulk AFE thermodynamic potential is presented in equation (1):

$$g_A = (\psi + t)\, q^2 + t r^2 - (q^4 + 6q^2 r^2 + r^4) + \\ + (q^6 + 15q^4 r^2 + 15q^2 r^4 + r^6) - \bar{e} q\,. \quad (1)$$

g_A, t, $\bar{e}$, q, r, and ψ, are reduced variables, or dimensionless quantities, corresponding to the thermodynamic potential of the AFE system, temperature, applied static electric field, normal electric displacement, staggered electric displacement, and the interaction constant of the AFE sublattices (Lim 2022; Lines,

 https://www.doi.org/10.33910/2687-153X-2025-6-1-35-48

Glass 1977). When the system is in equilibrium, the variation of g_A in equation (1) with respects to q and r is minimized, which gives the equations of state for the AFE system, as shown in equations (2):

$$2(\psi + t)q - (4q^3 + 12qr^2) + (6q^5 + 60q^3r^2 + 30qr^4) - \bar{e} = 0, \tag{2a}$$

$$2tr - (12q^2r + 4r^3) + (30q^4r + 60q^2r^3 + 6r^5) = 0. \tag{2b}$$

From equation (2b), the possible values of r are:

$$r_{FE} = 0, \tag{3a}$$

which corresponds to the field-induced FE phase, and

$$r_{\pm}^2 = \frac{-(15q^2 - 1) \pm \sqrt{180q^4 - 12q^2 + 1 - 3t}}{3}, \tag{3b}$$

which corresponds to the remnant AFE phase under the influence of the applied static field. The existence of the AFE phase is confirmed when the value of $r = r_{\pm}$ is non-zero and real. Substituting equations (3) into equation (2a) gives the equations of state of the AFE system in terms of q versus $\bar{e}$.

To reveal some features of the equations of state, equations (2) and (3) are solved numerically (Press et al. 1996), and the generated data are presented graphically. In the numerical calculations, the material parameters for ammonium dihydrogen phosphate (ADP) are adopted from previous work (Lim 2022). For ADP, the Curie temperature is T_C = 148 K. The fitting of ADP material constants yields $\psi \approx 0.01233$, $t \approx -3.346 \times 10^{-3}$, $e_C \approx 0.41658$, and $f_0 \approx 0.021336524$ at T = 80 K (Lim 2022), where f_0 is the natural frequency of the AFE system. The calculated points for ADP's equations of state are shown in Figure 1.

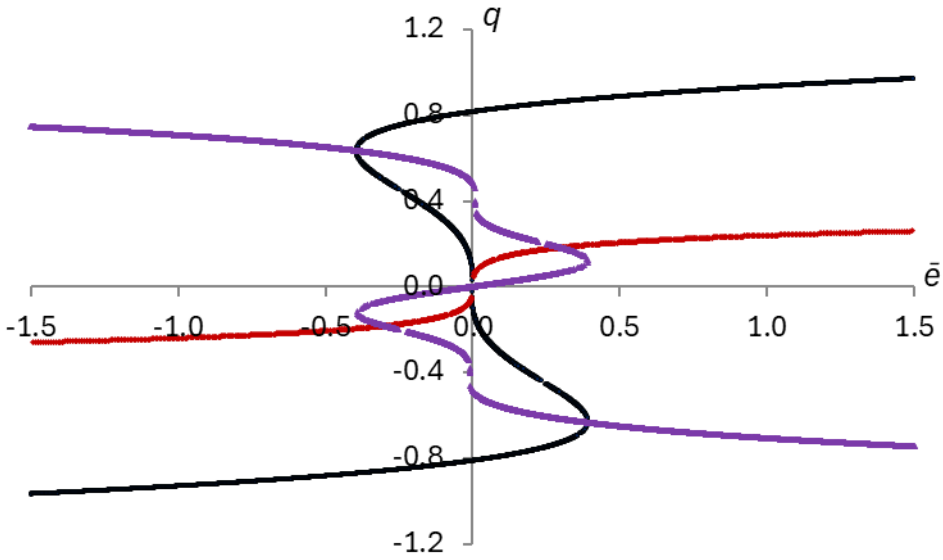

Fig. 1. Steady states for ADP at T = 80 K ($t \approx -3.346 \times 10^{-3}$), where FE states are represented by black dots (r = 0), AFE states by purple dots ($r = r_+$), and red dots ($r = r_-$)

In Figure 1, the black dots, calculated from equations (2a) and (3a), correspond to the field-induced FE states of the system, whereas the red ($r = r_-$) and purple ($r = r_+$) dots, obtained from equations (2a) and (3b), correspond to the remnant AFE states of the system. In Figure 1, the numerical points indicate the existence of AFE states for both $|\bar{e}| < e_C$ and $|\bar{e}| \geq e_C$. However, the bulk AFE system considered here does not account for stress, strain, size, or surface effects that may pin the AFE states for $|\bar{e}| \geq e_C$. Therefore, the condition for the existence of the AFE phase is that the magnitude of the applied static field must be smaller than the coercive field, i. e., $|\bar{e}| < e_C$. To satisfy this condition, the purple and red dots with $|\bar{e}| \geq e_C$

are removed. Additionally, in Figure 1, the AFE and FE states corresponding to the dots with negative slope trends are unstable and are unlikely to exist under an applied static electric field. To retain only the stable and metastable states, points exhibiting negative slopes are also removed (Line, Glass 1977). The results of discarding the unstable states and the AFE states with $|\bar{e}| \geq e_C$ are shown in Figure 2.

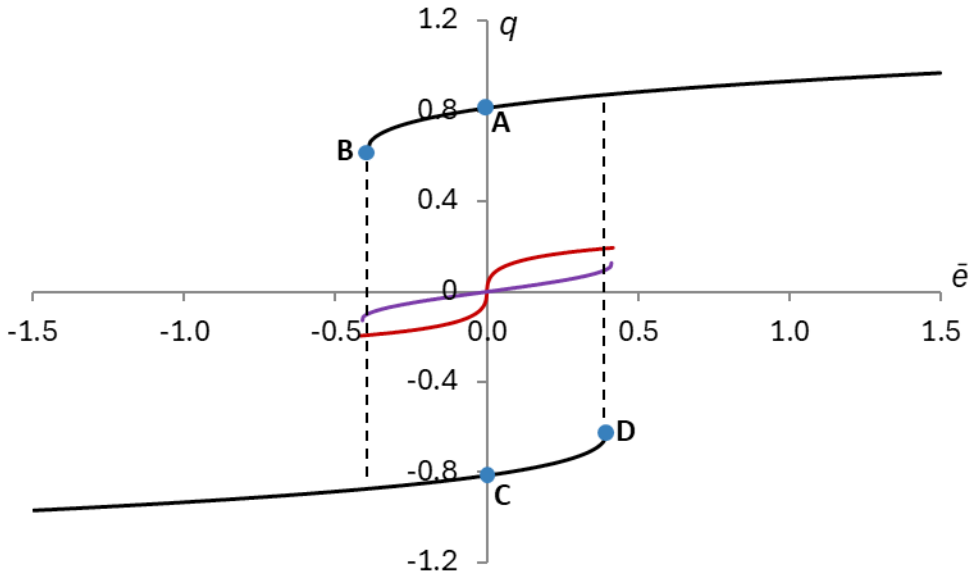

Fig. 2. Metastable states (AB and CD) and stable states of ADP at $T = 80\ K$ ($t \approx -3.346 \times 10^{-3}$), where FE states are represented by black curves ($r = 0$), AFE states by purple curves ($r = r_+$), and red curves ($r = r_-$)

The curves in Figure 2 show obvious hysteresis patterns with discontinuities around $\pm e_C$ for both FE and AFE states. Key differences between FE and AFE states include: (i) the FE states show a single hysteresis pattern, whereas the AFE states show a double hysteresis pattern; (ii) the magnitudes of the normal electric displacement in AFE states (i. e., $|q| < 0.2$) are significantly smaller than those in FE states (i. e., $|q| > 0.6$); (iii) the magnitude of the applied field required to induce discontinuous switching in FE states (i. e., $|\bar{e}| \approx 0.39325 \approx 0.944 e_C$) is smaller than that required in AFE states (i. e., $|\bar{e}| \approx e_C$); and (iv) the FE curves exhibit metastable state curves AB and CD (Line, Glass 1977).

Part II. AFE to FE phase transitions under the influence of applied sinusoidal fields and Gaussian white noise

In the formulation, the applied dynamic fields consist of two components: one is a deterministic sinusoidal field, and the other resembles Gaussian white noise with zero mean, adjustable amplitude, and variance. With these dynamic fields, the dimensionless bulk AFE thermodynamic potential is given in equation (4) (Lim 2022; Van den Broeck et al. 1994):

$$g_A = (\psi + t)q^2 + tr^2 - \left(q^4 + 6q^2r^2 + r^4\right) + \left(q^6 + 15q^4r^2 + 15q^2r^4 + r^6\right) - \\ -eq - D\xi(s)q, \tag{4}$$

where s is the dimensionless time variable, $e = e_0 \sin(2\pi fs)$ is the ***time-dependent applied electric field*** (in what follows referred to as '***field***' or '***applied field***'), and e_0 is the field amplitude. $\xi(s)$ represents Gaussian white noise, and $\mathcal{D} = \sigma e_0$ is the adjustable amplitude of the noise, where σ is a constant. In the presence of the field and noise, the dimensionless Landau — Khalatnikov equation of motion is given by equation (5) (Lim 2022):

$$\frac{d^2x_i}{ds^2} + \gamma \frac{dx_i}{d\tau} = -\frac{\delta g_A}{\delta x_i}, \tag{5}$$

 https://www.doi.org/10.33910/2687-153X-2025-6-1-35-48

where γ is dimensionless damping constant, and x_i represents the dimensionless normal or staggered electric displacements, q and r. The first and second terms in equation (5) represent the acceleration and damping of x_i. $\frac{\delta g_A}{\delta x_i}$ is the variation of g_A in equation (4) with respect to x_i. For small damping, the dynamics of q and r are oscillatory, which has been used to simulate chaotic dynamics without noise in previous works (Lim 2022; 2023). For large damping, such as γ = 1, the first-order time derivative terms dominate, and equation (5) can be approximated as nonlinear first-order stochastic relaxation equations for the AFE system, as shown in equations (6) (Khodabin, Rostami 2015; Van den Broeck et al. 1994):

$$dq = C_q ds + D dw, \tag{6a}$$

$$dr = C_r ds, \tag{6b}$$

where

$$C_q = -2(\psi + t)q + 4\left(q^3 + 3qr^2\right) - 6\left(q^5 + 10q^3r^2 + 5qr^4\right) + e, \tag{7a}$$

$$C_r = -2tr + 4\left(3q^2r + r^3\right) - 6\left(5q^4r + 10q^2r^3 + r^5\right), \tag{7b}$$

$$dw = \xi(s)ds. \tag{7c}$$

Equations (6) are used to simulate the dynamic phase transitions and hysteresis effects of AFE systems. The stochastic fourth-order Runge — Kutta (SRK4) method, an extension of the classic fourth-order Runge — Kutta method (Khodabin, Rostami 2015), is adopted to simulate equations (6). In the numerical scheme, equations (6) are rewritten in vector form, as shown in equation (8):

$$dX_s = C\left(X_s, s\right)ds + D\left(X_s, s\right)dW_s. \tag{8}$$

To solve equation (8), the SRK4 method involves discretizing the time interval into steps and updating the solution iteratively. Let X_n denote the approximation of X_{S_n} at time s_n, and let $\Delta s = s_{n+1} - s_n$. The SRK4 method updates X_{n+1} using the computed intermediate values as shown in equation (9):

$$K_1 = C\left(X_n, s_n\right)\Delta s + D\left(X_n, s_n\right)\Delta W_{n,1}, \tag{9a}$$

$$K_2 = C\left(X_n + \frac{1}{2}K_1, s_n + \frac{1}{2}\Delta s\right)\Delta s + D\left(X_n + \frac{1}{2}K_1, s_n + \frac{1}{2}\Delta s\right)\Delta W_{n,2}, \tag{9b}$$

$$K_3 = C\left(X_n + \frac{1}{2}K_2, s_n + \frac{1}{2}\Delta s\right)\Delta s + D\left(X_n + \frac{1}{2}K_2, s_n + \frac{1}{2}\Delta s\right)\Delta W_{n,3}, \tag{9c}$$

$$K_4 = C\left(X_n + K_3, s_n + \Delta s\right)\Delta s + D\left(X_n + K_3, s_n + \Delta s\right)\Delta W_{n,4}, \tag{9d}$$

where all the terms $\mathcal{D}$ (…, …) in equations (9) are adjustable constants. $\Delta W_{n,1}$, $\Delta W_{n,2}$, $\Delta W_{n,3}$, and $\Delta W_{n,4}$ are independent amplitude increments of the stochastic process with zero mean and variance Δs, i. e., $\Delta W_n \sim \mathcal{N}(0, \Delta s) = \sqrt{\Delta s}\,\mathcal{N}(0,1)$, where $\mathcal{N}(0,1)$ is the Gaussian random variable with zero mean and variance one. The updated solution is given by equation (10):

$$X_{n+1} = X_n + \frac{1}{6}\left(K_1 + 2K_2 + 2K_3 + K_4\right). \tag{10}$$

The material parameters adopted in the simulations are based on the parameters of ADP at $T = 80K$, which are the same as those used to generate Figures 1 and 2.

Before applying Gaussian white noise, two frequencies of the field are selected: $f_1 = 0.5f_0$ and $f_2 = 1.5f_0$. The corresponding transition amplitudes of the field needed to switch the system from AFE hysteresis to FE hysteresis are approximately $e_{0T1} = 1.0162e_C$ and $e_{0T2} = 1.0775e_C$, respectively. To reveal the effects of Gaussian white noise and maintain the periodicity of the induced normal electric displacement as the

applied field, the selected field amplitudes for the two frequencies are $e_{01} = 0.9857e_C$ and $e_{02} = 1.0443e_C$, which are approximately 97% of the corresponding transition amplitudes. The numerical results for the first set of frequency and amplitude, namely $f = f_1 = 0.5f_0$ and $|e_1| = e_{01} = 0.9857e_C$, with a standard deviation of $\sqrt{\Delta s_1} \approx 7.654083178069687 \times 10^{-2}$, are shown in Figures 3 and 4.

In Figure 3, the time series curves are presented as e_1 versus s (i. e., (s, e_1)), along with three q versus s curves (i. e., (s, q_1), (s, q_2), (s, q_3)), and three r versus s curves (i. e., (s, r_1), (s, r_2), (s, r_3)). These curves correspond to three amplitudes of noise: $\mathcal{D}_1 = 0.0630e_{01} = 0.06203610e_C$, $\mathcal{D}_2 = 0.0792e_{01} = 0.07798824e_C$, and $\mathcal{D}_3 = 0.0793e_{01} = 0.07808671e_C$. For all these curves, e_1 is switched on from the 1st to 45th cycles and switched off after the 45th cycle, whereas noise is switched on from the 1st to the 35th cycles, and switched off after the 35th cycle.

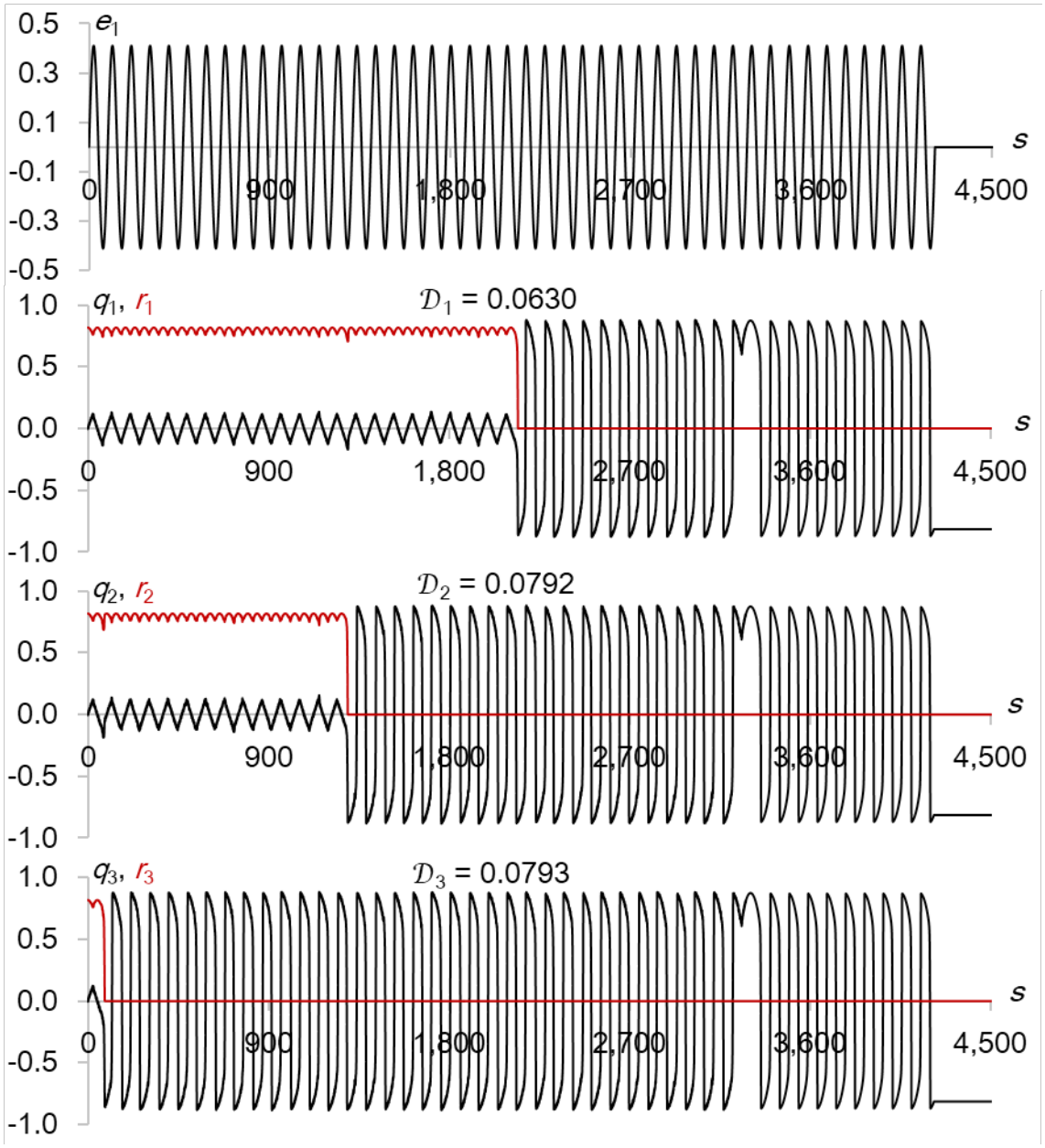

Fig. 3. Time series curves for (s, e_1), (s, q_1), (s, r_1), (s, q_2), (s, r_2), (s, q_3), and (s, r_3) for the 1st to 45th cycles. The three black (s, q) curves and three red (s, r) curves correspond to three amplitudes of noise: $\mathcal{D}_1 = 0.0630e_{01}$, $\mathcal{D}_2 = 0.0792e_{01}$, and $\mathcal{D}_3 = 0.0793e_{01}$. Here, $|e_1| = e_{01} = 0.9857e_C$, $f = f_1 = 0.5f_0$, and $\sqrt{\Delta s_1} \approx 7.654083178069687 \times 10^{-2}$; all noise is switched off after the 35th cycle

https://www.doi.org/10.33910/2687-153X-2025-6-1-35-48

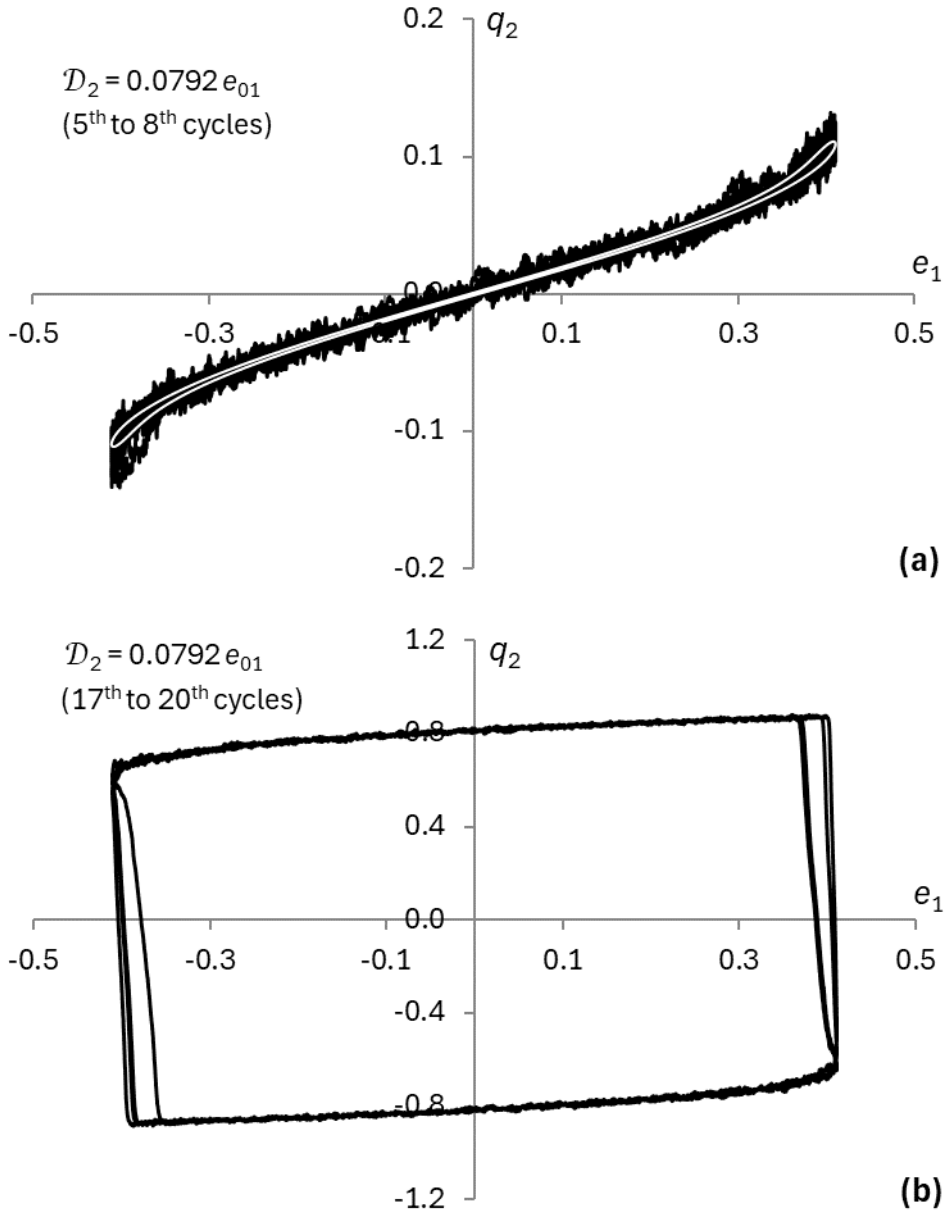

Fig. 4. (a) AFE hysteresis loops without noise (white loop, $\mathcal{D} = 0$) and AFE hysteresis loops with Gaussian white noise (black curves, $\mathcal{D}_2 = 0.0792e_{01}$) for the 5th to 8th cycles. (b) FE hysteresis loops induced by Gaussian white noise ($\mathcal{D}_2 = 0.0792e_{01}$) for the 17th to 20th cycles. Here, $f = f_1 = 0.5f_0$ and $|e_1| = e_{01} = 0.9857e_C$

When Gaussian white noise is activated, the transition from AFE hysteresis to FE hysteresis does not occur immediately but is delayed, as shown in the curves (s, q_1), (s, q_2) and (s, r_1), (s, r_2) in Figure 3. This is displayed as an abrupt change in the amplitudes of (s, q_1), (s, q_2) from less than 0.2 to greater than 0.6, and in (s, r_1), (s, r_2) from greater than 0.6 to approximately 0.0. For the noise amplitudes $\mathcal{D}_1 = 0.0630e_{01}$ and $\mathcal{D}_2 = 0.0792e_{01}$, the transitions from AFE hysteresis to FE hysteresis are delayed until the 23rd and 14th cycles, respectively. This indicates that a larger amplitude of Gaussian white noise results in a shorter delay time for the AFE to FE phase transition. The noise amplitude required to induce the transition is identified as $\mathcal{D}_3 = 0.0793e_{01}$, which is the smallest amplitude necessary to observe the transition occurring in the first cycle.

The numerical results indicate that when the amplitude of the field is smaller than the transition amplitude (i. e., $e_{01} < e_{0T1}$), and in the absence of noise ($\mathcal{D} = 0$), the system displays only the AFE hysteresis curve, depicted as a white loop in Figure 4(a). The black curves in Figures 4(a) and 4(b) show the hysteresis loops with Gaussian white noise, derived from a selected curve in Figure 3, specifically the (e_1, q_2) curve for $\mathcal{D}_2 = 0.0792e_0$, focusing on the 5th to 8th cycles (before the transition) and

the 17th to 20th cycles (after the transition), respectively. Due to the applied noise, the four successive AFE and FE hysteresis loops in Figures 4(a) and 4(b) show fluctuations and do not overlap. In particular, the black AFE hysteresis loops in Figure 4(a) exhibit fluctuations around the white loop. The FE hysteresis loops in Figure 4(b) exhibit both stable and unstable states, corresponding to the parts with positive and negative slopes.

The numerical results for the second set of frequency and amplitude, namely $f = f_2 = 1.5f_0$ and $|e_2| = e_{02} = 1.0443e_C$, with a standard deviation of $\sqrt{\Delta s_2} \approx 4.419086983258320 \times 10^{-2}$, are shown in Figures 5 and 6. In Figure 5, the time series curves display e_2 versus s (i. e., (s, e_2)), along with three q versus s curves (i. e., (s, q_4), (s, q_5), (s, q_6)), and three r versus s curves (i. e., (s, r_4), (s, r_5), (s, r_6)). These curves correspond to three amplitudes of noise: $\mathcal{D}_4 = 0.0561e_{02} = 0.05858523e_C$, $\mathcal{D}_5 = 0.0813e_{02} = 0.08490159e_C$, and $\mathcal{D}_6 = 0.0866e_{02} = 0.09043638e_C$. For all these curves, e_2 is switched on from the 1st to the 45th cycles and switched off after the 45th cycle, whereas noise is switched on from the 1st to the 35th cycles, and switched off after the 35th cycle.

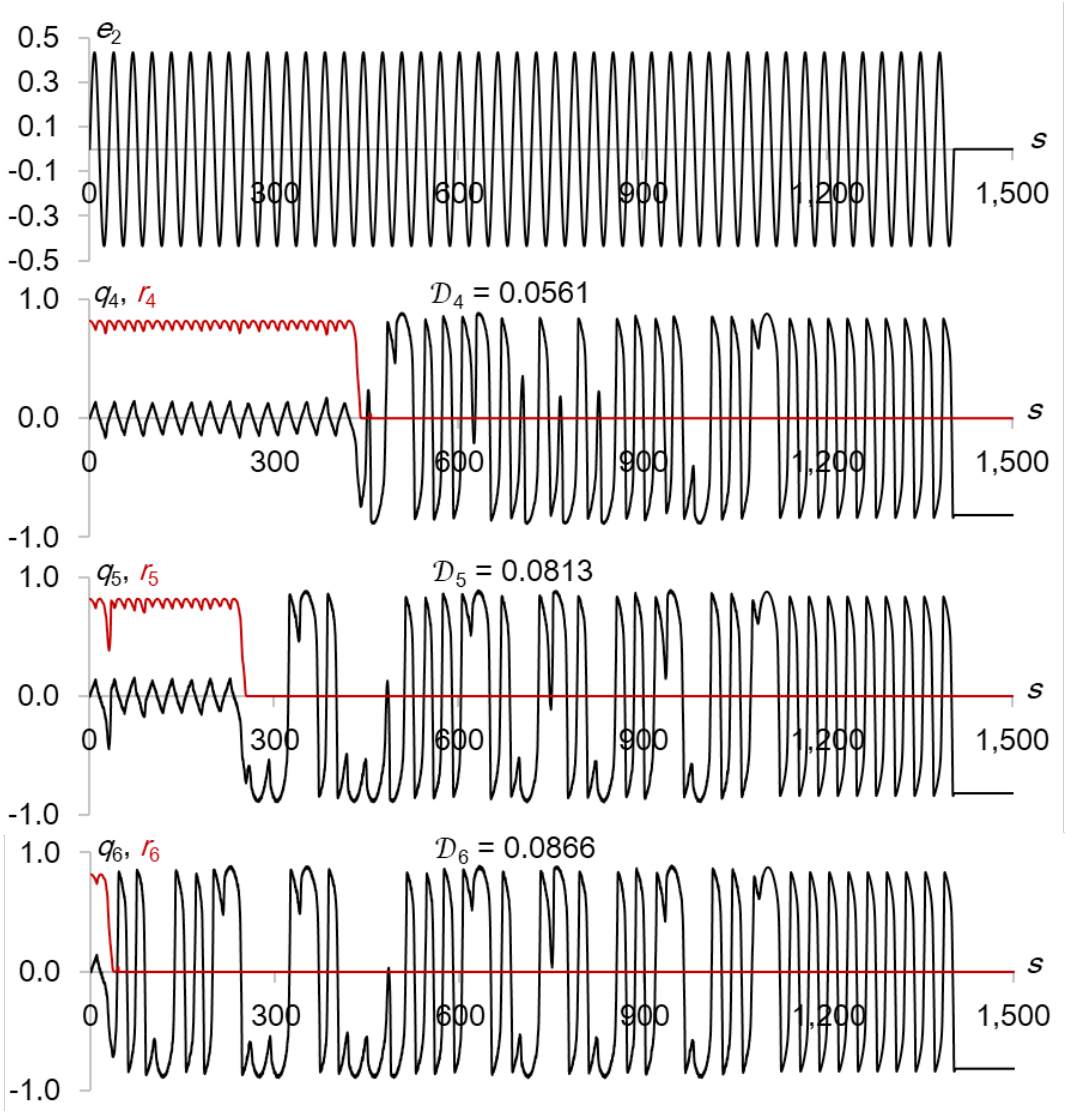

Fig. 5. Time series curves for (s, e_2), (s, q_4), (s, r_4), (s, q_5), (s, r_5), (s, q_6), and (s, r_6) for the 1st to 45th cycles. The three black (s, q) curves and three red (s, r) curves correspond to three amplitudes of noise: $\mathcal{D}_4 = 0.0561e_{02}$, $\mathcal{D}_5 = 0.0813e_{02}$, and $\mathcal{D}_6 = 0.0866e_{02}$. Here, $|e_2| = e_{02} = 1.0443e_C$, $f = f_2 = 1.5f_0$, and $\sqrt{\Delta s_2} \approx 4.419086983258320 \times 10^{-2}$; all noise is switched off after the 35th cycle

https://www.doi.org/10.33910/2687-153X-2025-6-1-35-48

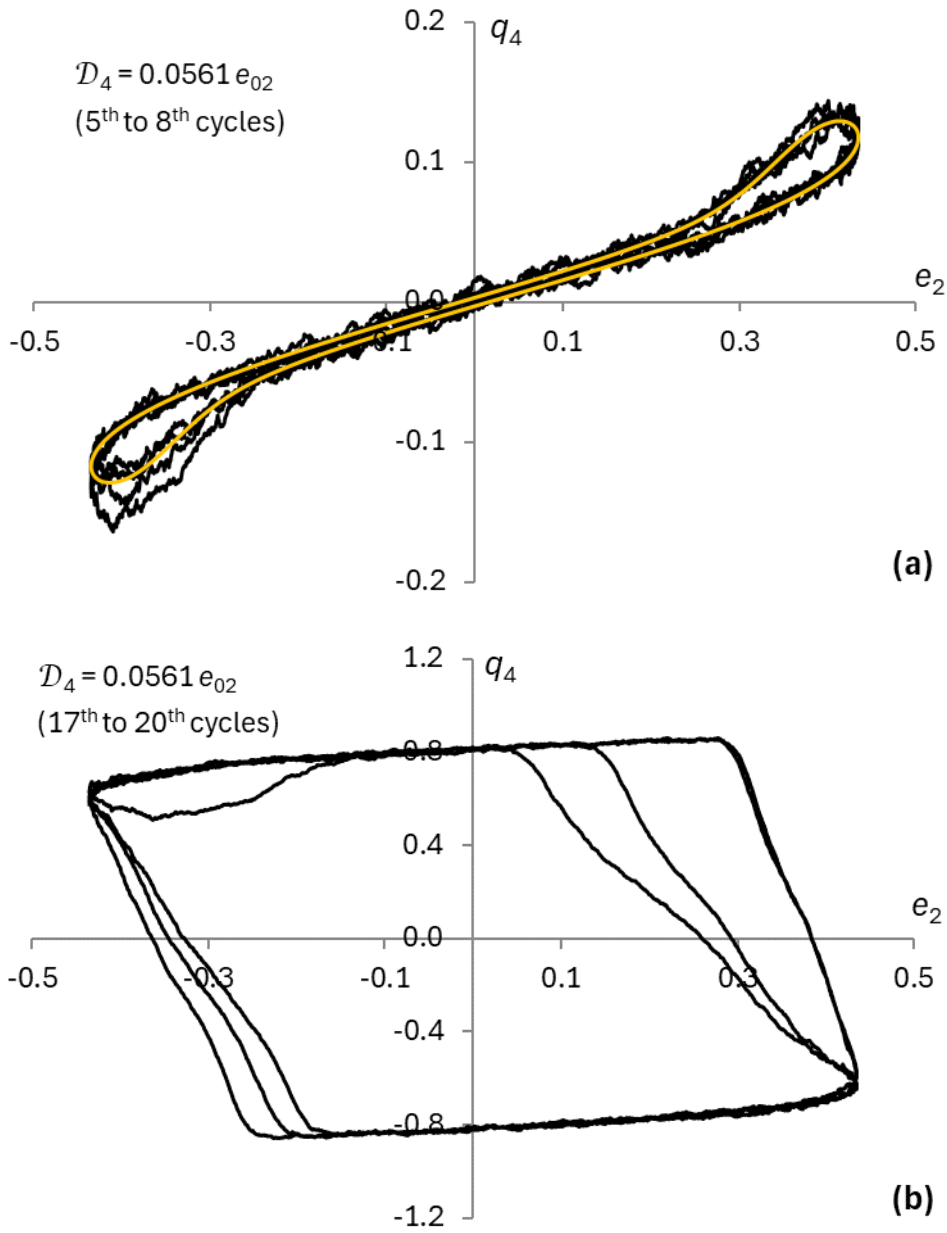

Fig. 6. (a) AFE hysteresis loops without noise (yellow loop, $\mathcal{D} = 0$) and AFE hysteresis loops with Gaussian white noise (black curves, $\mathcal{D}_4 = 0.0561e_{02}$) for the 5th to 8th cycles. (b) FE hysteresis loops induced by Gaussian white noise ($\mathcal{D}_4 = 0.0561e_{02}$) for the 17th to 20th cycles. Here, $f = f_2 = 1.5f_0$ and $e_0 = e_{02} = 0.9857e_C$

As with the first set of results, when Gaussian white noise is introduced, the transition from AFE to FE hysteresis does not occur immediately after noise is switched on; instead, it is delayed, as shown in the curves (s, q_4), (s, q_5) and (s, r_4), (s, r_5) in Figure 5. For the noise amplitudes $\mathcal{D}_4 = 0.0561e_{02}$ and $\mathcal{D}_5 = 0.0813e_{02}$, the transitions from AFE to FE hysteresis are delayed until the 14th and 8th cycles, respectively. This reflects the inversely proportional relationship between noise amplitude and time delay for the AFE to FE phase transition. The transition noise amplitude is identified as $\mathcal{D}_6 = 0.0866e_{02}$. In addition to the AFE to FE phase transitions, the three (s, q) curves in Figure 5 exhibit desynchronization, or phase slips, and a loss of periodicity while Gaussian white noise is switched on. The appearance of these features is the result of the crossing of unstable and fluctuating orbits (Berglund 2016).

When the amplitude of the field is smaller than the transition amplitude (i. e., $e_{02} < e_{0T2}$), and in the absence of noise ($\mathcal{D} = 0$), the system displays only the AFE hysteresis curve, depicted as a yellow loop in Figure 6(a). In contrast, the black curves in Figures 6(a) and 6(b) represent the hysteresis loops with Gaussian white noise, derived from the (e_2, q_4) curve in Figure 5, for $\mathcal{D}_4 = 0.0561e_{02}$, during the 5th to 8th cycles and the 17th to 20th cycles, corresponding to the periods before and after the AFE to FE phase

transition. As a result of the applied noise, the four successive AFE and FE hysteresis loops in Figures 6(a) and 6(b) do not overlap and show fluctuations. In particular, the black AFE curves in Figure 6(a) exhibit fluctuations around the yellow loop, while the FE hysteresis loops in Figure 6(b) display both stable and unstable states, corresponding to the parts with positive and negative slopes. The large and distorted deviations observed among the four successive FE hysteresis loops in Figure 6(b) are manifestations of desynchronization, or phase slips, as seen in the time series curve $(s, q)_4$ in Figure 5.

Part III: Hysteresis effects in the FE phase under strong field and moderate Gaussian white noise

In this section, the formalism, material parameters, and numerical schemes are the same as those in the second part. To enable comparison with the results from the second part, the same two frequencies and standard deviations are selected, i. e., $f_1 = 0.5f_0$ and $f_2 = 1.5f_0$. The selected strong field amplitudes for the two frequencies are $|e_3| = e_{03} = 1.5e_C$ and $|e_4| = e_{04} = 3.0e_C$, respectively, which are approximately 147.6% and 278.4% of the transition amplitudes e_{0T1} and e_{0T2}, respectively. To assess the effects of Gaussian white noise, moderate noise amplitudes of $\mathcal{D}_7 = 0.1e_{03} = 0.15e_C$ and $\mathcal{D}_8 = 0.1e_{04} = 0.30e_C$ are selected for the two frequencies, respectively. The numerical results for both frequencies, covering the 1st to 10th cycles, are presented in Figures 7 and 8.

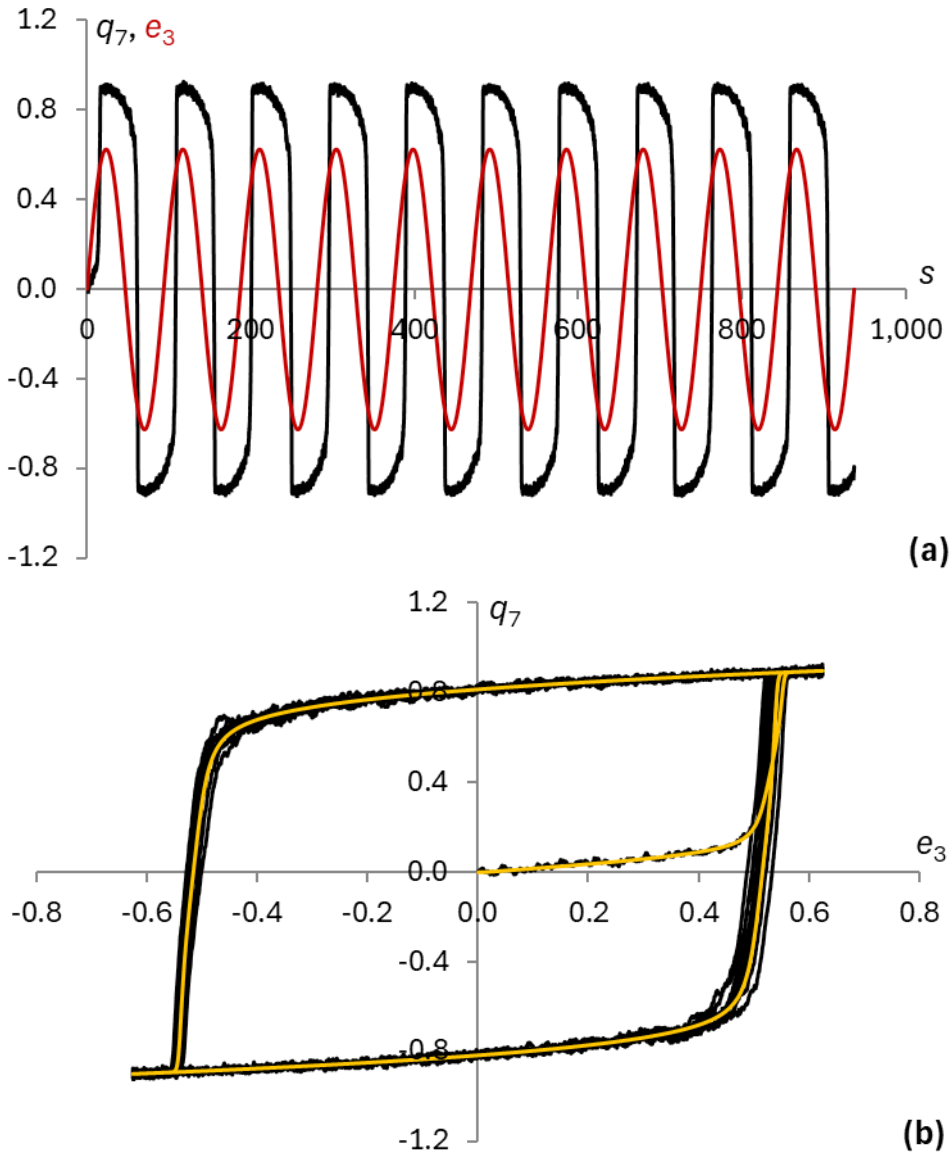

Fig. 7. (a) (s, e_3) and (s, q_7) time series curves. The (s, q_7) time series curve corresponds to Gaussian white noise with amplitude $\mathcal{D}_7 = 0.1e_{03}$. (b) FE hysteresis loops without noise (yellow loop, $\mathcal{D} = 0$), and FE hysteresis loops with Gaussian white noise, (e_3, q_7) (black curves, $\mathcal{D}_7 = 0.1e_{03}$), Here, $f = f_1 = 0.5f_0$, $|e_3| = e_{03} = 1.5e_C$, $\sqrt{\Delta s_1} \approx 7.654083178069687 \times 10^{-2}$, and the time range is 1st to 10th cycles

 https://www.doi.org/10.33910/2687-153X-2025-6-1-35-48

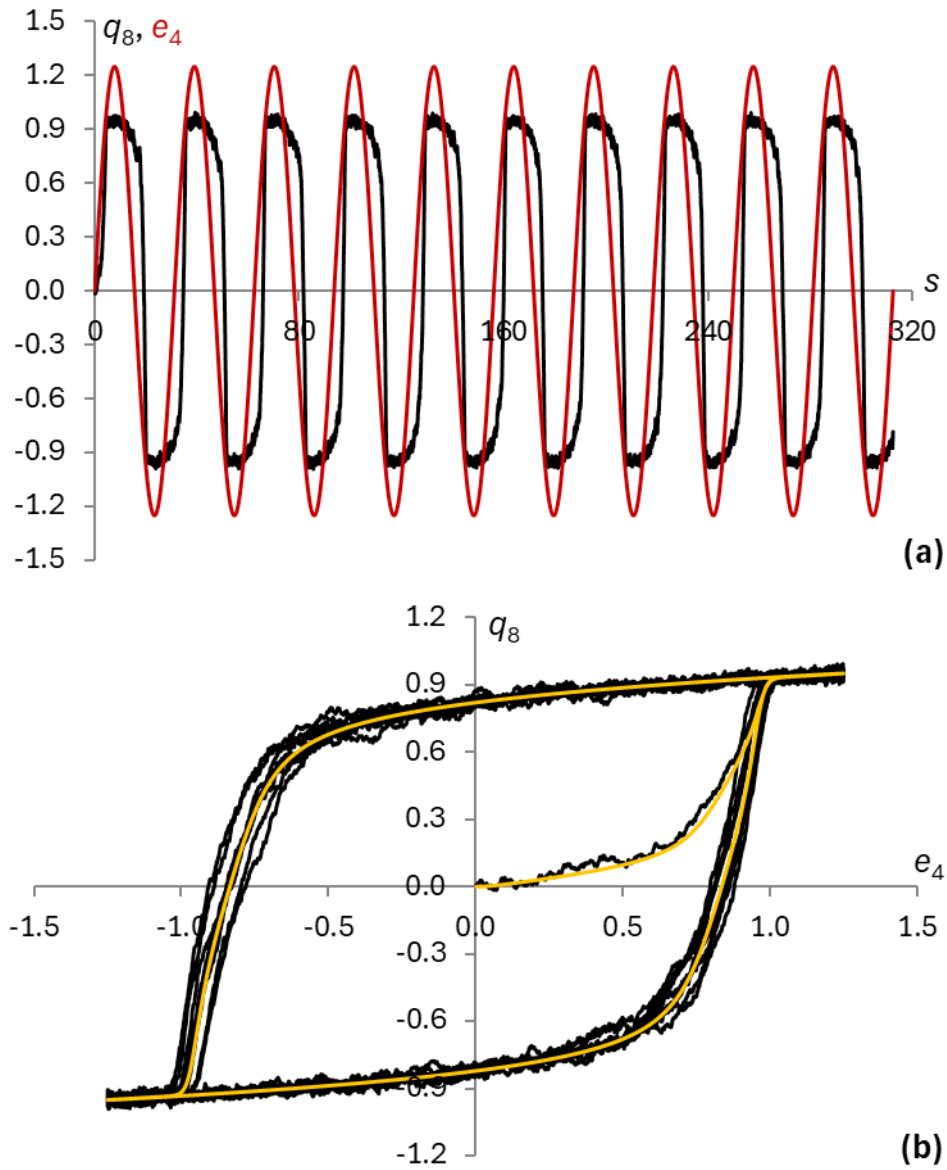

Fig. 8. (a) (s, e_4) and (s, q_8) time series curves. The (s, q_8) time series curve corresponds to Gaussian white noise with amplitude $\mathcal{D}_8 = 0.1e_{03}$. (b) FE hysteresis loops without noise (yellow loop, $\mathcal{D} = 0$), and FE hysteresis loops with Gaussian white noise (black curves, $\mathcal{D}_8 = 0.1e_{03}$), Here, $f = f_2 = 1.5f_0$, $|e_4| = e_{04} = 3.0e_C$, $\sqrt{\Delta s_2} \approx 4.419086983258320 \times 10^{-2}$, and the time range is 1st to 10th cycles

For f_1, the time series curves (s, e_3) and (s, q_7) are represented by the red and black curves in Figure 7(a). Similarly, for f_2, the time series curves (s, e_4) and (s, q_8) are represented by the red and black curves in Figure 8(a). The corresponding hysteresis curves (e_3, q_7) and (e_4, q_8) are shown in Figures 7(b) and 8(b). The numerical results indicate that in the absence of noise ($\mathcal{D} = 0$), the system shows only a single FE hysteresis loop, represented by the yellow hysteresis loop in Figures 7(b) and 8(b). Upon the introduction of Gaussian white noise, the FE hysteresis loops fluctuate around the yellow hysteresis loop and do not overlap. Given that the field amplitudes are significantly larger than the corresponding transition amplitudes e_{0T1} and e_{0T2}, the time series curves (s, q_7) and (s, q_8) in Figures 7(a) and 8(a) do not exhibit the pronounced desynchronization or phase slips, as seen in Figure 5.

Conclusions

The results in the first part of the reported study show the steady states of the selected AFE system, specifically ADP, under the applied static electric field. The numerical results demonstrate possible states of the system, including stable, unstable, and metastable states, as shown in Figure 1. By eliminating

unstable states and AFE states with $\bar{e} \geq e_C$, clear AFE and FE hysteresis patterns emerge, with the corresponding magnitudes of the induced normal electric displacement at $|q| < 0.2$ and $|q| > 0.6$, respectively. These steady states provide a baseline for identifying the AFE and FE phases in the second and third parts of the study.

In the second part, it is observed that for ADP, without the application of noise, a higher frequency requires a greater field amplitude for the dynamic phase transition from AFE to FE phases. For both selected frequencies, $f_1 = 0.5f_0 < f_0$ and $f_2 = 1.5f_0 > f_0$, and with the selected field amplitudes slightly below the critical field amplitudes (around 97%), additional Gaussian white noise with amplitudes less than 8% of the field amplitude induces a dynamic phase transition from AFE to FE phases. These phase transitions, however, are delayed for noise amplitudes below the corresponding critical values. The higher the level of noise, the shorter the delay time. This is due to the nonlinear nature of the system, where the system's states are affected by their history or past states over time. Consequently, the influence of noise accumulates until it reaches the threshold for the phase transition from AFE to FE phases. The stronger the noise, the faster the system gains the energy to cross the energy barrier and thus escape from AFE to FE states (Kramers 1940; Schüller et al. 2020; Tsimring, Pikovsky 2001). Notably, the transition delay means that when plotting the 2D hysteresis curves, both AFE and FE hysteresis loops may coexist if the AFE phase duration is not excluded from the analysis.

The hysteresis loops in the FE phase exhibit both stable and unstable states, identified by the positive and negative slopes of different parts of the hysteresis loop, as shown in Figures 4(b) and 6(b). More unstable features in the FE phase include desynchronization, phase slips, and loss of periodicity, which are clearly observed in the q versus s curves in Figure 5. It is also observed that, at higher frequency of the field, these instabilities become more pronounced. This is evident from comparing (i) the deviations of the four consecutive hysteresis loops in Figure 6(b), which are larger than those in Figure 4(b), and (ii) the more obvious desynchronization, phase slips, and loss of periodicity in the q versus s curves in Figure 5 compared to Figure 3. These instabilities arise because the selected field amplitudes are close to the transition amplitudes for the two selected frequencies.

When the field amplitude is well above the transition amplitude, it is evident that only the FE phase exists, and the effects of moderate Gaussian white noise diminish considerably. This is clearly observed in Figures 7(b) and 8(b) as the loss of negative slopes in the hysteresis loops, along with the recovery of synchronization, as evidenced by the time series curves in Figures 7(a) and 8(a). The residual effects of noise manifest as fluctuated and non-overlapping hysteresis loops.

In summary, when the field amplitude is just below the transition amplitude, the addition of Gaussian white noise will provide energy to the AFE system to overcome the energy barrier from AFE to FE phases, thereby inducing a transition. The transition does not occur immediately but is delayed for noise amplitudes slightly below than the critical value. Once the AFE system transitions to the FE phase, it remains in this phase, even when the noise and/or field are switched off. This indicates that the noise and field-induced phase transition from AFE to FE phases is irreversible, which is significantly different from the modeled non-stop transitions between ice ages and interglacials (Alexandrov et al. 2018; Benzi et al. 1981; Nicolis 1982). The bulk AFE model used in this study (Equation 4) does not include stress, strain, size effects, surface effects, or restoring forces that could pin the AFE states, which contributes to the irreversibility of the transition. In contrast, the phase transition from AFE to FE phases induced solely by a deterministic sinusoidal electric field, does not exhibit any delayed behavior.

To conclude, for the antiferroelectric system in its first-order phase, manipulating the frequency, the amplitudes of the applied field, and the levels of Gaussian white noise can control the timing of the AFE to FE phase transition. This feature may have applications in systems which require controllable switching time from small to large values of a physical quantity, corresponding to the AFE ($|q| < 0.2$) to FE ($|q| > 0.6$)phase transition. Moreover, this feature will provide direct observations of the system's order parameter behavior in its time series, similar to climate transitions over time. In future research, the analytical and numerical techniques developed here may be modified to enable the restoration of the AFE phase, and the study of noise-plus-field-induced phase transitions may be applied to other physical systems, such as antiferromagnets.

Conflict of Interest

The author declares that there is no conflict of interest, either existing or potential.

 https://www.doi.org/10.33910/2687-153X-2025-6-1-35-48

References

Alexandrov, D. V., Bashkirtseva, I. A., Ryashko, L. B. (2018) Noise-induced transitions and shifts in a climate–vegetation feedback model. *Royal Society Open Science*, 5 (4), article 171531. http://dx.doi.org/10.1098/rsos.171531 (In English)

Benzi, R., Sutera, A., Vulpiani, A. (1981) The mechanism of stochastic resonance. *Journal of Physics A: Mathematical and General*, 14 (11), L453–L457. https://doi.org/10.1088/0305-4470/14/11/006 (In English)

Berglund, N. (2016) Noise-induced phase slips, log-periodic oscillations, and the Gumbel distribution. *Markov Processes and Related Fields*, 22 (3), 467–505. https://hal.science/hal-00967427v2 (In English)

Cao, F. J., Wood, K., Lindenberg, K. (2007) Noise-induced phase transitions in field-dependent relaxational dynamics: The Gaussian ansatz. *Physical Review E*, 76 (5), article 051111. https://doi.org/10.1103/PhysRevE.76.051111 (In English)

Carrillo, O., Ibañes, M., García-Ojalvo, J. et al. (2003) Intrinsic noise-induced phase transitions: Beyond the noise interpretation. *Physical Review E*, 67 (4), article 046110. https://doi.org/10.1103/PhysRevE.67.046110 (In English)

Dagvadorj, G., Fellows, J. M., Matyjaśkiewicz, S. et al. (2015) Nonequilibrium phase transition in a two-dimensional driven open quantum system. *Physical Review X*, 5 (4), article 041028. https://doi.org/10.1103/PhysRevX.5.041028 (In English)

Garcia-Ojalvo, J., Sancho, J. M. (1999) *Noise in Spatially Extended Systems*. New York: Springer Publ., 307 p. (In English)

Gardiner, C. W. (1985) *Handbook of stochastic methods: For physics, chemistry and the natural sciences*. 2nd ed. Berlin: Springer Publ., 442 p. (In English)

Ghosh, P. K., Barik, D., Ray, D. S. (2005) Noise-induced transition in a quantum system. *Physics Letters A*, 342 (1–2), 12–21. https://doi.org/10.1016/j.physleta.2005.04.097 (In English)

Henkel, M., Pleimling, M. (2010) *Non-equilibrium phase transitions. Vol. 2: Ageing and dynamical scaling far from equilibrium*. Dordrecht: Springer Publ., 544 p. (In English)

Jin, Y., Xu, P. (2020) Noise-induced transitions and resonances in a delayed triple-well potential system. In: W. Lacarbonara, B. Balachandran, J. Ma et al. (eds.). *Nonlinear Dynamics of Structures, Systems and Devices: Proceedings of the First International Nonlinear Dynamics Conference (NODYCON 2019)*. Cham: Springer Publ., pp. 523–531. https://doi.org/10.1007/978-3-030-34713-0_52 (In English)

Khodabin, M., Rostami, M. (2015) Mean square numerical solution of stochastic differential equations by fourth order Runge-Kutta method and its application in the electric circuits with noise. *Advances in Difference Equations 2015*, 2015, article 62. https://doi.org/10.1186/s13662-015-0398-6 (In English)

Kramers, H. A. (1940) Brownian motion in a field of force and the diffusion model of chemical reactions. *Physica*, 7, 4, 284–304. https://doi.org/10.1016/S0031-8914(40)90098-2 (In English)

Levkivskyi, I. P., Sukhorukov, E. V. (2009) Noise-induced phase transition in the electronic Mach-Zehnder interferometer. *Physical Review Letters*, 103, article 036801. https://doi.org/10.1103/PhysRevLett.103.036801 (In English)

Lim, S.-Ch. (2022) Numerical simulations of nonlinear and chaotic order parameter responses in bulk antiferroelectrics using ammonium dihydrogen phosphate parameter. *Physics of Complex Systems*, 3 (3), 122–136. https://www.doi.org/10.33910/2687-153X-2022-3-3-122-136 (In English)

Lim, S.-Ch. (2023) Calculations of Lyapunov exponents and characterizations of nonlinear dynamics in bulk antiferroelectrics. *Physics of Complex Systems*, 4 (4), 176–194. https://www.doi.org/10.33910/2687-153X-2023-4-4-176-194 (In English)

Lines, M. E., Glass, A. M. (1977) *Principles and applications of ferroelectrics and related materials*. Oxford: Oxford University Press, 664 p. (In English)

Liu, S., Li, M.-R., Zhang, S.-Z. et al. (2024) Noise-induced phase transitions in hybrid quantum circuits. *Physical Review B*, 110 (6), article 064323. https://doi.org/10.1103/PhysRevB.110.064323 (In English)

Nicolis, C. (1982) Stochastic aspects of climatic transitions-response to a periodic forcing. *Tellus*, 34 (1), 1–9. https://doi.org/10.3402/tellusa.v34i1.10781 (In English)

Press, W. H., Teukolsky, S. A., Vetterling, W. T., Flannery, B. P. (1996) *Numerical Recipes in C: The Art of Scientific Computing*. 2nd ed. Cambridge: Cambridge University Press, 537 p. (In English)

Schüller, B., Meistrenko, A., van Hees, H. et al. (2020) Kramers' escape rate problem within a non-Markovian description. *Annals of Physics*, 412, article 168045. https://doi.org/10.1016/j.aop.2019.168045 (In English)

Tolédano, P., Guennou, M. (2016) Theory of antiferroelectric phase transitions. *Physical Review B*, 94 (1), article 014107. https://doi.org/10.1103/PhysRevB.94.014107 (In English)

Tong, N. H., Vojta, M. (2006) Signatures of a noise-induced quantum phase transition in a mesoscopic metal ring. *Physical Review Letters*, 97 (1), article 016802. https://doi.org/10.1103/PhysRevLett.97.016802 (In English)

Tsimring, L. S., A. Pikovsky, A. (2001) Noise-induced dynamics in bistable systems with delay. *Physical Review Letters*, 87 (25), article 250602. https://doi.org/10.1103/PhysRevLett.87.250602 (In English)

Van den Broeck, C., Parrondo, J. M. R., Toral, R. (1994) Noise-induced nonequilibrium phase transition. *Physical Review Letters*. 73 (25), 3395–3398. https://doi.org/10.1103/PhysRevLett.73.3395 (In English)

Zhang, G., Novais, E., Baranger, H. U. (2017) Rescuing a quantum phase transition with quantum noise. *Physical Review Letters*, 118 (5), article 050402. https://doi.org/10.1103/PhysRevLett.118.050402 (In English)

Zhang, M.-H., Fulanović, L., Egert, S. et al. (2020) Electric-field-induced antiferroelectric to ferroelectric phase transition in polycrystalline NaNbO3. *Acta Materialia*, 200, 127–135. https://doi.org/10.1016/j.actamat.2020.09.002 (In English)

Zhang, M.-H., Fulanović, L., Zhao, C. H., Koruza, J. (2023) Review on field-induced phase transitions in lead-free NaNbO3-based antiferroelectric perovskite oxides for energy storage. *Journal of Materiomics*, 9 (1), 1–18. https://doi.org/10.1016/j.jmat.2022.09.008 (In English)

Theoretical physics.
Electronic structure of solids

UDC 538.915 + 538.955 + 530.145.3

EDN MDSAWK
https://www.doi.org/10.33910/2687-153X-2025-6-1-49-53

On the electronic quantum structures of conductors

V. D. Pavlov ✉[1]

[1] Vladimir Electromechanical Plant, 127 Noyabrskaya Str., Vladimir 600901, Russia

Author

Valentin D. Pavlov, ORCID: 0000-0003-2125-4897, e-mail: pavlov.val.75@mail.ru

For citation: Pavlov, V. D. (2025) On the electronic quantum structures of conductors. *Physics of Complex Systems*, 6 (1), 49–53. https://www.doi.org/10.33910/2687-153X-2025-6-1-49-53 EDN MDSAWK

Received 9 December 2024; reviewed 15 January 2025; accepted 15 January 2025.

Funding: The study did not receive any external funding.

Abstract. This paper investigates the quantum of kinetic momentum in a two-particle system of correlated electrons. Under these conditions, the minimum possible magnetic flux quantum becomes half of the flux calculated for a single electron, presenting an apparent contradiction. Since magnetic flux is an additive quantity, one might naturally expect an increase, not a decrease, in the flux. This study aims to resolve this contradiction. While pair correlation leads to a halving of the magnetic flux quantum relative to F. London's value, *n*-fold correlations would theoretically reduce the quantum by a factor of *n*. This, however, defies conventional explanation. It is unacceptable to attribute the quantum of kinetic momentum to a Cooper pair; rather, a quantum of kinetic momentum must be assigned to an individual particle, not a system of particles. F. London's quantum should, therefore, be regarded solely as a quantum of magnetic flux.

Keywords: quantum structure, correlated electrons, conductor, mean free path, kinetic moment, magnetic flux

Introduction

Two-particle quantum systems of electrons, referred to as Cooper pairs (Daido, Yanase 2024; Sivukhin 2002), emerge in conductors as a result of electron-phonon interactions (Ishida, Matsueda 2021; Wu, Liu 2023).

In these systems, a quantum of kinetic momentum ħ is ascribed to the correlated electron pair, resulting in a magnetic flux quantum that is half the value calculated for a single electron (Pavlov 2020). This presents a contradiction, as magnetic flux is inherently additive, and one would typically expect an increase in flux rather than a decrease. The objective of this study is to address and resolve this contradiction.

The research adopts a theoretical approach, employing both quantum mechanical and semiclassical considerations (Nesterov et al. 2024; Timchenko et al. 2022).

The exclusivity of two-particle systems in the creation of magnetic flux

Pair correlations occur in conductors with short electron mean free paths, and are absent in those with long mean free paths (Sivukhin 2002). The quantum of magnetic flux from a two-particle system was first measured in 1961 for conductors with short electron mean free paths. However, this does not preclude the possibility of measuring the magnetic flux quantum from a single electron in a conductor with a long mean free path, where pair correlations are absent. Notably, the quantum measured by F. London is twice as large as the value measured in 1961, and advancements in measurement equipment have increased sensitivity.

Consequently, the creation and measurement of magnetic flux by a two-particle system of electrons is not exclusive; a single electron can also generate a magnetic flux.

Magnetic quantization from a conductor with a long electron mean free path

The magnetic flux energy expression is derived as follows:

$$E = \frac{I\Phi}{2}.$$

Current from a single electron:

$$I = \frac{e}{T},$$

where T is the time it takes for an electron to complete one revolution in a circular path.

$$T = \frac{2\pi R}{v}.$$

Here R is the size of the circular contour, v is the linear velocity of the charge.
At the same time,

$$E = \frac{m_e v^2}{2}.$$

Comparison of the given expressions derives

$$\Phi = \frac{2\pi R m_e v}{e} = \frac{2\pi R p}{e},$$

where p is the amount of motion.

Since the electron is not correlated (unique), no dual interpretation of the quantum of its kinetic moment is possible. This leads us to the following:

$$m_e vR = pR = \hbar, \tag{1}$$

and results in:

$$\Phi_L = \frac{2\pi\hbar}{e} = \frac{h}{e}. \tag{2}$$

This represents the well-known F. London's quantum of magnetic flux.

Magnetic quantization from current created by two electrons

The current generated by two moving charges is double that of a single charge, irrespective of whether the charges are correlated.

Consequently, the magnetic flux created by the doubled current is also twice as large. Applying this to the equations above (2), we derive:

$$\Phi_2 = 2\Phi_L = \frac{2h}{e}.$$

The textbook value of the magnetic flux quantum created by a Cooper pair is four times smaller.

 https://www.doi.org/10.33910/2687-153X-2025-6-1-49-53

$$\Phi_0 = \frac{h}{2e}. \tag{3}$$

Obtaining value (3) is possible only by adding the values that are inverse to (2)

$$\frac{1}{\Phi} = \frac{1}{\Phi_L} + \frac{1}{\Phi_L} = \frac{2}{\Phi_L} = \frac{2e}{h}. \tag{4}$$

There is no reasonable explanation for this.

Pairwise correlations are not the limit

The textbook calculation of the magnetic flux quantum accounts only for Cooper pairs of electrons, thus assuming pairwise correlations. At the same time, correlations of more than two electrons are possible, and, in some cases, multi-particle correlations could even be less pronounced.

Just as pair correlations result in a halving of the magnetic flux quantum compared to F. London's value, *n*-particle correlations would theoretically reduce the quantum by a factor of *n*:

$$\Phi_0 = \frac{h}{ne}. \tag{5}$$

There is no rational explanation for this, just like (3) and (4).

Magnetic quantization from a conductor with a short electron mean free path

If we accept the expression for the Cooper pair (Equation 3), it follows that one electron generates half the magnetic flux of the Cooper pair:

$$\Phi_0 = \frac{1}{2}\frac{h}{2e} = \frac{h}{4e}.$$

In the case of n-particle correlations, the magnetic flux quantum would further decrease:

$$\Phi_0 = \frac{1}{n}\frac{h}{ne} = \frac{h}{n^2 e}.$$

This phenomenon is conceptually unacceptable (Popov 2024b).

On double standards

In a poor conductor, two correlated electrons are assigned a quantum of kinetic momentum ħ on the basis of their being part of a quantum system. This would have to be agreed with if this approach were extended to other similar quantum systems, such as two electrons in helium, where the role of phonons (in conductors) is analogous to the attractive force of the atomic nucleus in helium (Popov 2024a). Let this be so. In other words:

$$2m_e v r_{\mathrm{He}} = \hbar. \tag{6}$$

There are three forces applied to an electron: attraction to the nucleus, repulsion from another electron, and centrifugal force.

$$\frac{2e^2}{4\pi\varepsilon_0 r_{\mathrm{He}}^2} - \frac{e^2}{4\pi\varepsilon_0 (2r_{\mathrm{He}})^2} = \frac{m_e v^2}{r_{\mathrm{He}}},$$

$$1.75\frac{e^2}{4\pi\varepsilon_0 r_{\mathrm{He}}^2} = \frac{m_e v^2}{r_{\mathrm{He}}}. \tag{7}$$

Expression (6) squared

$$4m_e^2v^2r_{\text{He}}^2 = \hbar^2,$$

$$r_{\text{He}}^3 = \frac{\hbar^2}{4m_e^2v^2}.$$

Ther relation (7) takes the form:

$$1.75\frac{e^2}{4\pi\varepsilon_0}\frac{4m_e^2v^2}{\hbar^2} = \frac{m_ev^2}{r_{\text{He}}},$$

$$r_{\text{He}} = \frac{m_ev^2 4\pi\varepsilon_0\hbar^2}{1.75e^2 4m_e^2v^2} = \frac{4\pi\varepsilon_0\hbar^2}{1.75e^2 4m_e} = \frac{a_0}{7}.$$

In quantitative terms it results in:

$$r_{\text{He}} = \frac{a_0}{7} = \frac{5.2917721092\cdot10^{-11}}{7} \approx 7.56\cdot10^{-12}(m).$$

The result differs from the table value by almost four times.

At the same time, if not the pair, but each electron is attributed a quantum of kinetic momentum $\hbar$, the resulting calculations will be correct.

There are two possible ways out of this situation.

First. The pair of helium electrons should not be assigned a quantum of kinetic momentum $\hbar$. Therefore, in order to avoid double standards, other multi-particle systems, including the Cooper pair of electrons, should not be assigned it either.

Second. Multi-particle quantum systems should be assigned a quantum of kinetic momentum $\hbar$, including the pair of helium electrons. But then we will have to admit that the radius of the helium atom is four times smaller than is commonly believed.

The first option seems more preferable.

Conclusion

Kinetic momentum is an additive quantity. The contributions of each element of a multi-particle system must be summed. If the kinetic momentum of a multi-particle system is equal to the quantum ħ, it implies that each particle (electron) has a kinetic moment equal to a fractional part of the quantum. This, however, undermines the very concept of a quantum.

Therefore, attributing the quantum $\hbar$ of kinetic moment to the Cooper pair is fundamentally incorrect.

On the other hand, if the value of the magnetic flux quantum for the Cooper pair measured in 1961 is reliable, then the radius of the helium atom must be four times smaller than currently assumed.

Alternatively, the quantum of kinetic momentum ħ should be attributed to individual particles, not systems of correlated particles. F. London's quantum should, therefore, be regarded solely as a quantum of magnetic flux.

Conflict of Interest

The author declares that there is no conflict of interest, either existing or potential.

References

Daido, A., Yanase, Y. (2024) Rectification and nonlinear hall effect by fluctuating finite-momentum cooper pairs. *Physical Review Research*, 6 (2), article L022009. https://doi.org/10.1103/physrevresearch.6.l022009 (In English)

Ishida, K., Matsueda, H. (2021) Two-step dynamics of photoinduced phonon entanglement generation between remote electron-phonon systems. *Journal of the Physical Society of Japan*, 90, article 104714. https://doi.org/10.7566/JPSJ.90.104714 (In English)

Nesterov, V. Yu., Presnov, N. D., Zabotnov, S. V. et al. (2024) Three-photon absorption and photoluminescence in films of liquid-crystal polymers with embedded CDSE/ZNS quantum dots. *Physics of Complex Systems*, 5 (1), 3–9. https://doi.org/10.33910/2687-153X-2024-5-1-3-9 (In English)

Pavlov, V. D. (2020) Magnitnyo potok i ego kvantovanie [Magnetic flow and its quantization]. *Izvestiya Ufimskogo nauchnogo tsentra RAN — Proceedings of the RAS Ufa Scientific Centre*, 4, 25–28. https://doi.org/10.31040/2222-8349-2020-0-4-25-28 (In Russian)

Popov, I. P. (2024a) Dvojnye standarty pri opisanii atomov geliya i pozitroniya [Double standards when describing helium and positronium atoms]. *Vestnik Tomskogo gosudarstvennogo universiteta. Khimiya — Tomsk State University Journal of Chemistry*, 35, 143–151. (In Russian)

Popov, I. P. (2024b) Seven singular points in quantum mechanics. *Technical Physics*. [Online]. Available at: https://doi.org/10.1134/S1063784224700427 (accessed 01.04.2024). (In English)

Sivukhin, D. V. (2002) *Obshchij kurs fiziki. T. 5. Atomnaya i yadernaya fizika [General course of physics. Vol. 5. Atomic and nuclear physics]*. Moscow: Fizmatlit Publ., 784 p. (In Russian)

Timchenko, B. A., Faleeva, M. P., Gilev, P. A. et al. (2022) Atmospheric implementation of superdense coding quantum algorithm. *Physics of Complex Systems*, 3 (4), 186–201. https://doi.org/10.33910/2687-153X-2022-3-4-186-201 (In English)

Wu, C., Liu, C. (2023) Effects of phonon bandgap on phonon–phonon scattering in ultrahigh thermal conductivity θ-phase TAN. *Chinese Physics B*, 32, article 046502. https://doi.org/10.1088/1674-1056/acb201 (In English)

Summaries in Russian / Информация о статьях на русском языке

Физика конденсированного состояния

ПОЛИСУЛЬФОНАМИДНЫЕ МЕМБРАНЫ-ЭЛЕКТРЕТЫ ДЛЯ РАЗДЕЛЕНИЯ ЭМУЛЬСИИ УГЛЕВОДОРОДОВ

Мансур Флоридович Галиханов, Ильдар Гильманович Шайхиев, Владислав Олегович Дряхлов, Земфира Талгатовна Санатуллова

Аннотация. Сточные воды, содержащие эмульгированные нефтепродукты, представляют серьезную угрозу для окружающей среды. Углеводороды изменяют физико-химические свойства среды обитания, отравляют организм живых организмов, обволакивают поверхность тела, что приводит к угнетению биоценоза и деградации экосистем. В этой связи в работе исследованы полисульфонамидные мембраны для очистки воды от эмульгированного масла. Для повышения устойчивости к замасливанию и улучшения эксплуатационных характеристик фильтры обрабатывались коронным разрядом при напряжении U = 5-35 кВ в течение 1–5 мин. В результате коронной обработки эффективность увеличилась с 74,9 до 84,5%, при этом производительность повысилась до ≈ 11 раз. Данное обстоятельство объясняется изменением контактных свойств поверхности модифицированных мембран, как показано результатами настоящего исследования.

Ключевые слова: сточные воды, нефтепродукты, полисульфонамидные мембраны, индустриальное масло, коронная обработка, эмульсия

Для цитирования: Galikhanov, M. F., Shaikhiev, I. G., Dryakhlov, V. O., Sanatullova, Z. T. (2025) Polysulfonamide electret membranes for hydrocarbon emulsion separation. *Physics of Complex Systems*, 6 (1), 3–8. https://www.doi.org/10.33910/2687-153X-2025-6-1-3-8 EDN XCXNQF

МЕХАНИЗМ ТРАНСПОРТА ЗАРЯДА В ОРГАНИЧЕСКОЙ ПЛЕНКЕ НА ОСНОВЕ ФТОРИРОВАННОГО ПОЛИАРИЛОВОГО ЭФИРА, СОДЕРЖАЩЕГО БЛОКИ В ЦЕПИ 1,4-ДИОКСО-ТИОКСАНТЕН-9-ОНА

Андрей Андреевич Гисматулин, Владимир Алексеевич Пустоваров, Данила Сергеевич Одинцов, Ирина Александровна Оськина, Инна Казимировна Шундрина, Иван Алексеевич Азаров, Леонид Анатольевич Шундрин, Владимир Алексеевич Гриценко

Аннотация. На основе перфторбифенила и 1,4-дигидрокси-9Н-тиоксантен-9-она был синтезирован новый термостабильный полиарилэфир (FPAE-ThS) с электроноакцепторным тиоксантеноновым фрагментом в составе полимерной цепи. Механизм транспорта заряда в FPAE-ThS пленке описывается фонон-облегченным туннелированием между ловушками. Определены термическая (1.0 eV) и оптическая (2.0 eV) энергии ионизации ловушек и концентрация ловушек ($N=1.0\times10^{20}$ cm^{-3}). Половина значения Стоксового сдвига (1,1 эВ), полученного из спектров фотолюминесценции и спектров возбуждения фотолюминесценции, соответствует результатам моделирования транспорта заряда. Показано, что модельное запоминающее устройство на основе пленки FPAE-ThS обладает резистивными переключениями с разницей в сопротивлении на 4 порядка между состояниями мемристора с низким и высоким сопротивлением.

Ключевые слова: фторированные полимеры, транспорт заряда, мемристор, ловушка, фотолюминесценция, спектры возбуждения фотолюминесценции

Для цитирования: Gismatulin, A. A., Pustovarov, V. A., Odintsov, D. S., Os'kina, I. A., Shundrina, I. K., Azarov, I. A., Shundrin, L. A., Gritsenko, V. A. (2025) Charge transport mechanism and memristive effect in a thin film based on fluorinated polyaryl ether containing 1,4-dioxo-thioxanthene-9-one in-chain blocks. *Physics of Complex Systems*, 6 (1), 9–16. https://www.doi.org/10.33910/2687-153X-2025-6-1-9-16 EDN ZZHQFC

ЭЛЕКТРЕТНЫЕ СВОЙСТВА И ЭЛЕКТРОПРОВОДНОСТЬ КОМПОЗИТОВ ПОЛИПРОПИЛЕН-ПОЛИФЕНИЛЕНСУЛЬФИД

Андрей Александрович Павлов, Михаил Анатольевич Коваленко, Виктор Антонович Гольдаде, Маргарита Эдуардовна Борисова, Сергей Валентинович Зотов

Аннотация. Исследованы электретные свойства и электропроводность полимерных композитов полипропилен-полифениленсульфид (ПП-ПФС). Показано, что эффективная поверхностная плотность заряда значительно выше у волокнисто-пористых материалов (ВПМ) по сравнению с пленочными. Установлено, что на графиках зависимостей удельной электропроводности композитов от обратной температуры наблюдается излом при температуре примерно 110 °C. Высокотемпературный участок кривой характеризует собственную проводимость диэлектрика, низкотемпературный — «структурно чувствительную» или примесную. В спектрах токов термостимулированной деполяризации (ТСД) наблюдается два релаксационных максимума. Низкотемпературный максимум тока определяет процесс релаксации заряда, накопленного на границе раздела матрицы (ПП) и наполнителя (ПФС), что обусловлено поляризацией Максвелла — Вагнера. Высокотемпературный максимум тока предположительно связан с релаксационным процессом, обусловленным собственной проводимостью ПП в аморфной фазе.

Ключевые слова: полипропилен, полифенилен сульфид, электрет, электропроводность, композиционный материал

Для цитирования: Pavlov, A. A., Kovalenko, M. A., Goldade, V. A., Borisova, M. E., Zotov, S. V. (2025) Electret properties and electrical conductivity of polypropylene-polyphenylene sulfide composites. *Physics of Complex Systems*, 6 (1), 17–25. https://www.doi.org/10.33910/2687-153X-2025-6-1-17-25 EDN OEOMHP

Физика полупроводников

МОДЕЛЬ ПОВЕДЕНИЯ МОП-СТРУКТУР ПРИ ТЕРМОПОЛЕВЫХ ОБРАБОТКАХ

Олег Викторович Александров, Никита Николаевич Морозов

Аннотация. Разработана количественная модель поведения МОП-структур при термополевых обработках в режимах накопления и восстановления подвижного заряда в подзатворном диэлектрике. Транспорт подвижного заряда рассматривается на основе модели захвата ионов на полиэнергетические ловушки с диапазоном энергий связи. Проведено моделирование временных зависимостей смещения порогового напряжения МОП-структур при положительном и последующем отрицательном смещении затвора. Предложенная модель позволяет описать экспериментальное симметричное и асимметричное поведение МОП-структур, содержащих ионы Na+. Определены диапазон энергий связи, концентрации и области локализации ловушек.

Ключевые слова: МОП-структура, подзатворный диэлектрик, подвижный заряд, термополевая обработка, дисперсионный транспорт, полиэнергетические ловушки, аморфный диоксид кремния, моделирование

Для цитирования: Aleksandrov, O. V., Morozov, N. N. (2025) Modelling the behavior of metal-oxide-semiconductor structures under thermal field treatment. *Physics of Complex Systems*, 6 (1), 26–34. https://www.doi.org/10.33910/2687-153X-2025-6-1-26-34 EDN TUEBOO

Теоретическая физика

ЧИСЛЕННОЕ МОДЕЛИРОВАНИЕ ГАУССОВСКОГО БЕЛОГО ШУМА И ИНДУЦИРОВАННОГО ПОЛЕМ ФАЗОВОГО ПЕРЕХОДА В ОБЪЕМНЫХ АНТИФЕРРОЭЛЕКТРИКАХ НА ОСНОВЕ ДИГИДРОФОСФАТА АММОНИЯ

Сью-Чу Лим

Аннотация. В настоящей работе представлены феноменологические и численные исследования гауссовского белого шума и индуцированного полем динамического фазового перехода в объемных антиферроэлектриках (АФЭ). Особое внимание уделено задержке перехода от антиферроэлектрического к ферроэлектрическому (ФЭ) состоянию. Стационарные состояния АФЭ приводятся на основе вариационного анализа термодинамического потенциала АФЭ при отсутствии шума. Стохастические уравнения релаксации для АФЭ выводятся с применением уравнения Ландау — Халатникова, где расчет термодинамического потенциала АФЭ учитывает гауссовский белый шум и изменяемое во времени синусоидальное электрическое поле. Эти уравнения решаются численно с использованием стохастического метода Рунге — Кутты четвертого порядка (SRK4). Результаты показывают, что при амплитуде приложенного поля, составляющей 97% от амплитуды

перехода, дополнительный гауссовский белый шум с амплитудами менее 8% от приложенного поля вызывает задержку фазового перехода от АФЭ к ФЭ, при этом время задержки обратно пропорционально амплитуде шума.

Ключевые слова: гауссовский белый шум, стохастический метод Рунге — Кутты четвертого порядка (SRK4), динамический фазовый переход, антиферроэлектрики, ферроэлектрики

Для цитирования: Lim, S.-Ch. (2025) Numerical simulations of Gaussian white noise and field-induced phase transition in bulk antiferroelectrics using parameters of ammonium dihydrogen phosphate. *Physics of Complex Systems*, 6 (1), 35–48. https://www.doi.org/10.33910/2687-153X-2025-6-1-35-48 EDN DNZGSD

ОБ ЭЛЕКТРОННЫХ КВАНТОВЫХ СТРУКТУРАХ ПРОВОДНИКОВ

Валентин Дмитриевич Павлов

Аннотация. Двухчастичной системе коррелированных электронов приписывается квант кинетического момента. Вследствие этого минимально возможный магнитный поток (квант) стал меньше (в два раза), чем поток, рассчитанный для одного электрона. Налицо противоречие, поскольку магнитный поток — величина аддитивная, и поэтому естественнее было бы ожидать его увеличения, а не уменьшения. Цель исследования заключается в разрешении указанного противоречия. Подобно тому как при парной корреляции квант магнитного потока вдвое уменьшился по сравнению с квантом Ф. Лондона, при n-кратной корреляции квант уменьшится в n раз. Этому нет разумного объяснения. Приписывание куперовской паре кванта кинетического момента неприемлемо. Квантом кинетического момента следует наделять единственную частицу, а не систему частиц. Квант Ф. Лондона единственно может рассматриваться в качестве кванта магнитного потока.

Ключевые слова: квантовая структура, коррелированные электроны, проводник, длина свободного пробега, кинетический момент, магнитный поток

Для цитирования: Pavlov, V. D. (2025) On the electronic quantum structures of conductors. *Physics of Complex Systems*, 6 (1), 49–53. https://www.doi.org/10.33910/2687-153X-2025-6-1-49-53 EDN MDSAWK